Nano Research

Open Access

Review Article

Advances in two-dimensional transition metal dichalcogenide nanocomposites for electromagnetic interference shielding: A review

Lianglong Xie[1], Fangxue Hang[1], Debao Niu[1], Kai Li[1]✉, Yougen Hu[2]✉, and Fukang Deng[1]✉

[1] School of Light Industry and Food Engineering, Guangxi University, Nanning 531004, China
[2] Shenzhen Institute of Advanced Electronic Materials, Shenzhen Institutes of Advanced Technology, Chinese Academy of Sciences, Shenzhen 518055, China

Cite this article: *Nano Research*, **2026**, *19*, 94908348. https://doi.org/10.26599/NR.2026.94908348

ABSTRACT: With the rapid advancement of the electronics industry, the demand for new electromagnetic interference (EMI) shielding materials has grown substantially in recent decades. In response, a wide range of novel materials are being investigated as alternatives to conventional metals. Consequently, lightweight EMI shielding materials designed for miniaturized and highly integrated electronic devices have attracted increasing attention. Two-dimensional (2D) transition metal dichalcogenides (TMDs) offer several advantages—such as excellent thermal and chemical stability, tunable electrical conductivity, unique layered structures, and ultrathin thickness—making them promising candidates for EMI shielding. This review summarizes recent advances in TMDs and their nanocomposites for EMI shielding, highlighting synthesis strategies and offering in-depth analysis of shielding effectiveness, thickness, flexibility, and underlying mechanisms. In addition, the current challenges and future prospects of TMD-based EMI shielding materials are discussed.

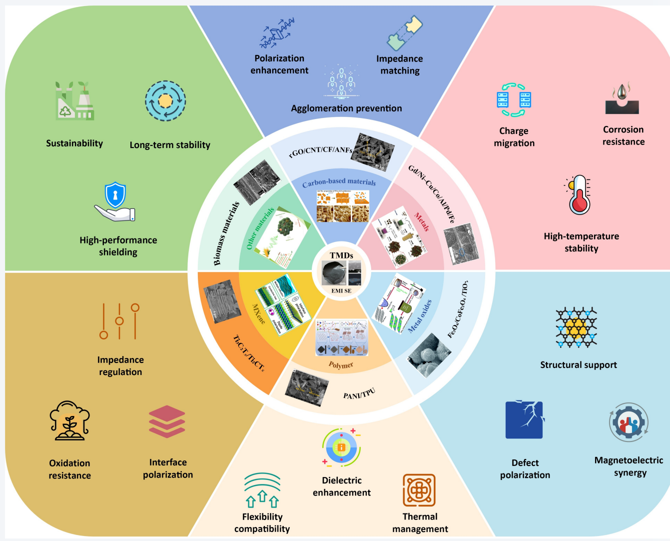

KEYWORDS: transition metal dichalcogenides, electromagnetic interference (EMI) shielding, carbon-based material, metallic network, polymer, MXene

1 Introduction

In the current technological era, the advent of fifth-generation (5G) communication has accelerated the expansion of the electronics industry, making wireless communication and electronic devices ubiquitous in daily life [1–4]. Prolonged exposure to electromagnetic waves (EMWs) emitted by these devices may pose risks to human health [5–8] and interfere with the performance of other systems, a phenomenon known as electromagnetic interference (EMI) [9–11]. EMI shielding is widely regarded as an effective strategy to mitigate these effects [12–15]. Controlling electromagnetic radiation pollution has therefore become increasingly urgent [16–18]. To achieve sustainable development, safeguard human health, and ensure information security, researchers are actively developing high-performance EMI shielding materials [19–21].

Shielding materials are defined as those capable of reducing microwave reflection by eliminating or attenuating incident waves [22, 23]. Core requirements include high shielding effectiveness (SE), low weight, flexibility, corrosion resistance, and cost efficiency [24–26]. Research in this [26] field dates back to the 1950s, initially for microwave protection and stealth applications, and today it spans both military and civilian domains that demand highly efficient shielding materials [27–29]. Effective EMI shielding depends on two critical factors: the development of high-performance materials and the influence of environmental fluctuations on their properties [30]. For shielding among multiple

Received: October 10, 2025; **Revised:** December 10, 2025
Accepted: December 15, 2025

✉Address correspondence to Fukang Deng, fk.deng@gxu.edu.cn; Yougen Hu, yg.hu@siat.ac.cn; Kai Li, gxlikai@gxu.edu.cn

devices, materials must exhibit high conductivity, low magnetic permeability, and strong attenuation capability [31, 32]. Metals have traditionally served as the dominant choice because of their excellent conductivity [33–35]. Their free electrons move easily within the lattice, forming an effective barrier against EMWs. Common examples include copper (Cu), aluminum (Al), and silver (Ag), while ferrites and μ-metals are used to block magnetic fields due to their low magnetic permeability. Cu is the most widely used owing to its high conductivity (5.9×10^7 S/m), Al is valued for its low weight and cost, and steel for its strength and durability. However, the heavy weight and processing limitations of metals restrict broader application [36, 37].

To overcome these drawbacks, researchers have increasingly explored nanomaterials for EMI shielding [38]. Prominent examples include conductive polymers [39, 40], magnetic materials [41–43], carbon-based structures [44–48], ceramics such as silicon carbide and barium titanate [49–52], transition metal dichalcogenides (TMDs) [53–58], and MXenes such as $Ti_3C_2T_x$ and Ti_2CT_x [59–65]. Heterogeneous composites combining one-dimensional (1D), two-dimensional (2D), magnetic, or dielectric fillers have also been developed to improve performance, yielding lighter, more stable, and corrosion-resistant materials [66, 67].

Among the numerous candidate materials, TMDs and their composites offer a unique pathway for addressing the next generation of “green” electromagnetic shielding challenges, distinguishing themselves from MXenes and graphene [68]. While MXenes and graphene demonstrate exceptional intrinsic electrical conductivity, resulting in excellent shielding effectiveness, their shielding mechanism primarily relies on electromagnetic wave reflection, which can lead to secondary electromagnetic interference issues [69, 70]. In contrast, TMDs possess moderate electrical conductivity and tunable semiconductor properties, making them more suitable for impedance matching with free space, thereby allowing greater penetration of electromagnetic waves into the material [71]. Once inside, the electromagnetic energy can be efficiently dissipated as heat through mechanisms such as the unique dielectric polarization of TMDs, abundant interface defects, and multiple scattering at heterojunctions [72]. This paradigm shift from “reflective shielding” to “absorptive shielding” represents a core competitive advantage of TMDs in addressing electromagnetic compatibility issues within devices [73]. Furthermore, the precise control over electromagnetic properties through factors like phase (e.g., 1T vs. 2H phase) and elemental composition (e.g., S vs. Se) further enhances the appeal of TMDs, a level of tunability that is difficult to match by other two-dimensional materials [74, 75].

Among these, TMDs—such as molybdenum disulfide (MoS_2), tungsten disulfide (WS_2), niobium diselenide ($NbSe_2$), and tantalum disulfide (TaS_2)—stand out as typical 2D materials. They feature weak interlayer van der Waals forces, high electron mobility, and tunable surface defects. Their electrical properties can be adjusted through phase regulation, such as the metallic 1T phase or semiconducting 2H phase, providing new opportunities to optimize shielding performance [76–78]. With high surface area, adjustable conductivity, and interlayer reflection pathways, TMDs synergistically enhance SE through combined reflection and absorption, offering distinct advantages for EMI shielding [79, 80]. In fact, carbon materials and MoS_2 were studied and exfoliated prior to graphene. Structurally, TMDs resemble graphene, clay, and oxides, with layered precursors that can be exfoliated into nanosheets with diverse functionalities.

In the optimization of electromagnetic shielding in TMDs, with MoS_2 as a typical example, phase engineering and the tunability of conductivity are core methods. Both parameters precisely adjust reflection loss (electromagnetic wave surface reflection) and absorption loss (internal energy dissipation of electromagnetic waves), which together determine the SE [81]. This relationship can be quantitatively characterized by the differences in conductivity across phases and SE parameters [82, 83]. Phase engineering can create 1T, 2H, and 1T/2H mixed-phase systems: The 1T phase is metallic, with a conductivity of approximately 10^2 S/m (10^7 times greater than the semiconductor 2H phase, which has a conductivity of $\approx 10^{-5}$ S/m) [75, 82]. It exhibits very strong reflection loss (due to a significant impedance mismatch between the material’s wave impedance, $\approx 0.1\ \Omega$, and that of air, $377\ \Omega$), causing substantial reflection of electromagnetic waves. However, severe impedance mismatch results in poor SE—for example, pure 1T-phase MoS_2 (T-P, 1T content 76%) has reflection loss (RL) rarely dropping below −10 dB (the effective absorption threshold), making it impractical. The 2H phase, being a semiconductor, has a wave impedance of approximately $100\ \Omega$, which is closer to that of air, leading to weak reflection loss. Its low conductivity also results in negligible absorption loss (only weak polarization loss). Pure 2H-phase samples (T-220, 1T content 0%) exhibit no effective absorption bandwidth (EAB), and electromagnetic waves almost entirely penetrate the material [82–84].

The 1T/2H mixed-phase system can overcome the limitations of single-phase materials. When the 1T content is controlled to approximately 23%–25% (e.g., t-60 ≈ 23%, T-185 ≈ 25%), the 1T phase provides sufficient reflection loss, while the 2H phase optimizes impedance matching. The 1T/2H phase interface also generates Maxwell–Wagner–Sillars polarization loss due to charge accumulation, further enhancing energy dissipation. The resulting materials exhibit excellent SE: For example, the minimum reflection loss (RL_{min}) of t-60 reaches −59.8 dB at 11.5 GHz (2.68 mm), with an EAB of 6.8 GHz (10.5–17.3 GHz, covering the X-band and part of the Ku-band), while maintaining cycling stability. It is important to note that when the 1T content is too high (e.g., 76%) or too low (0%), the SE sharply declines due to exacerbated impedance mismatch or insufficient absorption, which confirms the quantitative role of phase ratio in controlling SE, and provides clear guidance for the optimization of TMD-based shielding materials [82].

Nevertheless, the SE of individual TMDs remains limited, relying primarily on absorption in semiconducting phases and conductive reflection in metallic phases. By integrating TMDs with other materials—such as carbon, metals, metal oxides, and polymers—the shielding performance can be significantly enhanced through synergistic effects [85, 86]. This review therefore summarizes recent advances in TMDs and their nanocomposites for EMI shielding (Fig. 1). It first outlines shielding mechanisms, key performance parameters, and measurement methods. It then discusses synthesis strategies, shielding effectiveness, and underlying mechanisms of various nanocomposites. Finally, current challenges and future prospects of TMD-based EMI shielding materials are explored. not needed. Make sure that all pages have page numbers. Ensure that all parts of the manuscript are presented clearly.

2 Mechanism of EMI shielding

2.1 Shielding mechanism and calculation mechanisms

As shown in Fig. 2, incident electromagnetic radiation interacts with both the surface and interior of a shielding material through

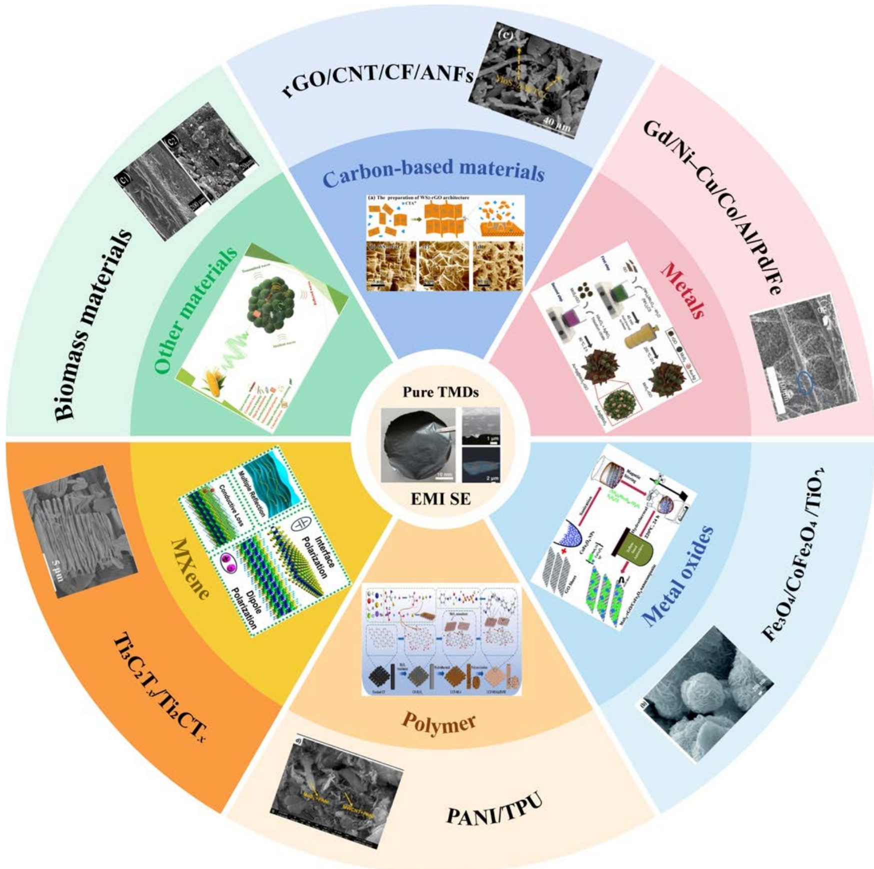

Figure 1 Schematic of various TMDs nanocomposite materials for EMI shielding field. Reproduced with permission from Ref. [54], © The Royal Society of Chemistry 2024; Ref. [55], © Deng, F. K. et al. 2023; Ref. [87], © American Chemical Society 2019; Ref. [88], © Elsevier Ltd. 2022; Ref. [191], © Elsevier B.V. 2024; Ref. [196], © Liu, Z. et al. 2023, under exclusive licence to Korean Carbon Society; Ref. [194], © The Royal Society of Chemistry 2019; Ref. [213], © Elsevier Ltd. 2025; Ref. [167], © American Chemical Society 2024; Ref. [231], © Elsevier B.V. 2024; Ref. [116], © Wang, J. E. et al. 2024, published by Nano-Micro Letters.

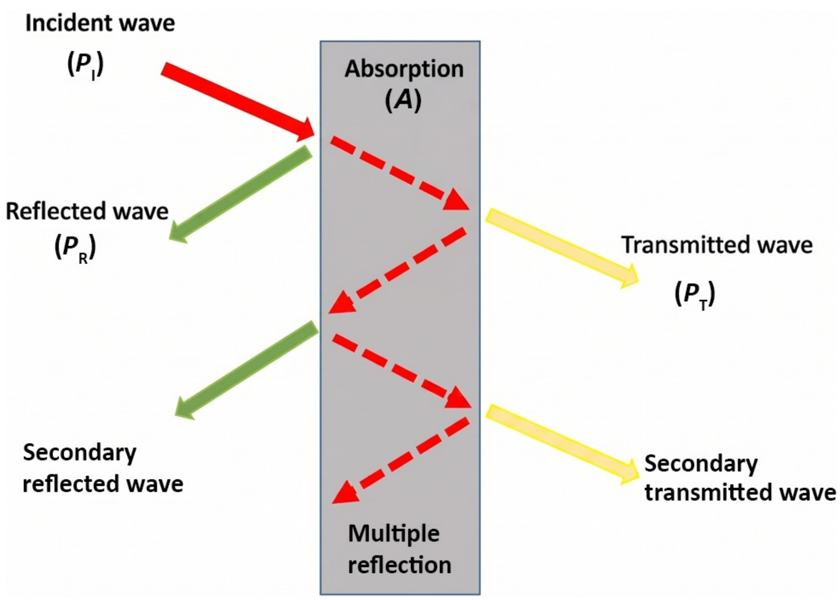

Figure 2 Mechanism of EMI shielding. Reproduced with permission from Ref. [98], © Wiley-VCH GmbH 2022.

several mechanisms, which can be described in terms of impedance mismatch, reflection, absorption, and transmission. When an incident electromagnetic wave reaches the shielding body, mismatch between the impedance of the material and the surrounding air causes part of the incident power (P_I) to be reflected from the surface (P_R) The remaining energy is either absorbed (A) within the material due to attenuation or transmitted (P_T), where it is further dissipated as heat [89].

The SE of a material is typically expressed on a logarithmic scale as shown in Eq. (1), which relates the ratio of transmitted to incident power, or equivalently, the transmitted to incident electric field strength (Eq. (1))

$$\mathrm{SE_T\ (dB)} = 10\ \lg\frac{P_\mathrm{T}}{P_\mathrm{I}} = 20\lg\frac{E_\mathrm{T}}{E_\mathrm{I}} \tag{1}$$

Here, E and P denote the electric field strength and power, respectively, with subscripts T and I indicating transmitted and incident EMWs. Attenuation of EMWs occurs via reflection, absorption, and multiple reflections [90, 91]. The total shielding effectiveness ($\mathrm{SE_T}$) can therefore be expressed as the sum of reflection ($\mathrm{SE_R}$), absorption ($\mathrm{SE_A}$), and multiple reflection ($\mathrm{SE_M}$) contributions, as shown in Eq. (2) [92, 93]

$$\mathrm{SE_T} = \mathrm{SE_R} + \mathrm{SE_A} + \mathrm{SE_M} \tag{2}$$

An alternative evaluation method employs a two-port network model, where scattering parameters (S-parameters) are used to determine transmission (T) and reflection (R) coefficients. In this framework, subscripts 1 and 2 correspond to the input and output ports, respectively, and the coefficients are expressed as Eqs. (3) and (4)

$$R = \left|\frac{E_\mathrm{R}}{E_\mathrm{T}}\right|^2 = |S_{11}|^2 = |S_{22}|^2 \tag{3}$$

$$T = \left|\frac{E_\mathrm{T}}{E_\mathrm{I}}\right|^2 = |S_{12}|^2 = |S_{21}|^2 \tag{4}$$

S-parameter measurements must be conducted under matched input–output conditions to avoid internal reflections. Based on these coefficients, absorption can be calculated as Eq. (5)

$$A = 1 - R - T \tag{5}$$

If absorption attenuation $\mathrm{SE_A}$ is less than 10 dB, the contribution of multiple reflections ($\mathrm{SE_M}$) can be neglected. In this case, the effective absorption A_eff is defined as Eq. (6)

$$A_\mathrm{eff}\ \mathrm{(dB)} = \frac{1-(T+R)}{1-R} \tag{6}$$

The individual contributions of reflection and absorption can then be calculated using Eqs. (7) and (8)

$$\mathrm{SE_R\ (dB)} = 10\lg\left(\frac{1}{1-R}\right) \tag{7}$$

$$\mathrm{SE_A\ (dB)} = 10\lg\left(\frac{1}{1-A_\mathrm{eff}}\right) = 10\lg\left(\frac{1-R}{T}\right) \tag{8}$$

Accordingly, the total shielding effectiveness simplifies to Eq. (9)

$$\mathrm{SE_T\ (dB)} = \mathrm{SE_R} + \mathrm{SE_A} \tag{9}$$

In addition, the absolute shielding effectiveness normalized by thickness and density (SSE/t) is often used as a comparative metric of material performance. This parameter is defined as Eq. (10)

$$\mathrm{SSE}/t\ (\mathrm{dB \cdot cm^2/g}) = (\mathrm{EMI\ SE/density})/t \tag{10}$$

This comprehensive framework highlights how reflection, absorption, and transmission collectively determine the shielding effectiveness of materials, while the SSE/t metric provides a useful benchmark for evaluating and comparing the efficiency of different shielding systems [94–96].

2.2 Key parameters and theoretical models

SE, measured in decibels (dB), provides a direct measure of a material's ability to block electromagnetic radiation. As defined in Eq. (2), The total shielding effectiveness ($\mathrm{SE_T}$) includes contributions from reflection ($\mathrm{SE_R}$), absorption ($\mathrm{SE_A}$), and multiple reflections ($\mathrm{SE_M}$).

The dielectric constant and conductivity strongly influence SE. According to classical electromagnetic theory, for a thick shield of thickness t, conductivity σ_s, and permeability μ_r, the shielding effectiveness is given by Eq. (11) [97]

$$\mathrm{SE\ (dB)} = 20\frac{t}{\delta}\lg e + 10\lg\left(\frac{\sigma_\mathrm{s}}{16\omega\varepsilon_0\mu_\mathrm{r}}\right) \tag{11}$$

Here, δ is the skin depth, ω is the angular frequency, ε_0 is the permittivity of free space, and μ_r is the relative permeability of the material. The first term corresponds to absorption loss, while the second term represents reflection loss. Equation (11) indicates that absorption-related SE scales with the square root of conductivity, whereas reflection-related SE scales logarithmically. Consequently, higher conductivity leads to enhanced shielding performance.

During reflection, the incident wave energy is not dissipated but becomes a secondary source of electromagnetic pollution, potentially interfering with surrounding systems. Therefore, effective EMI shielding requires dispersing EMWs primarily through absorption, which demands materials with appropriate electrical or magnetic properties [97]. The absorption-related component is given by Eq. (12)

$$\mathrm{SE_A\ (dB)} = 20\frac{t}{\delta}\lg e = 20t\sqrt{\frac{\mu_\mathrm{r}\omega\sigma_\mathrm{s}}{2}}\lg e \tag{12}$$

where $\sigma_\mathrm{s} = \omega\varepsilon_0\varepsilon''$, with ε'' being the imaginary part of the complex permittivity, and the skin depthis defined as Eq. (13)

$$\delta = \frac{1}{\sqrt{\pi\mu\sigma\nu}} \tag{13}$$

Skin depth directly governs EMW absorption and is inversely proportional to conductivity, frequency, and permeability. Hence, optimizing these parameters is critical for designing effective EMI shielding materials.

3 EMI shielding measurement methods

Selecting an appropriate measurement technique is critical for obtaining accurate electromagnetic shielding data. Common approaches include the open-field method, shielding box method, shielding chamber method, and coaxial transmission line method.

The open-field (free-space) method directly measures SE under typical operating conditions and is considered a reliable approach for evaluating electronic devices. As shown in Fig. 3(a), the sample is placed between two horn antennas connected to a vector network analyzer (VNA) via coaxial cables. Antenna 1 transmits while antenna 2 receives. Because this method does not account for diffracted or reflected fields, the data often require post-processing with time-domain gating algorithms to ensure accuracy [98–100].

The shielding box method is widely used for comparative testing

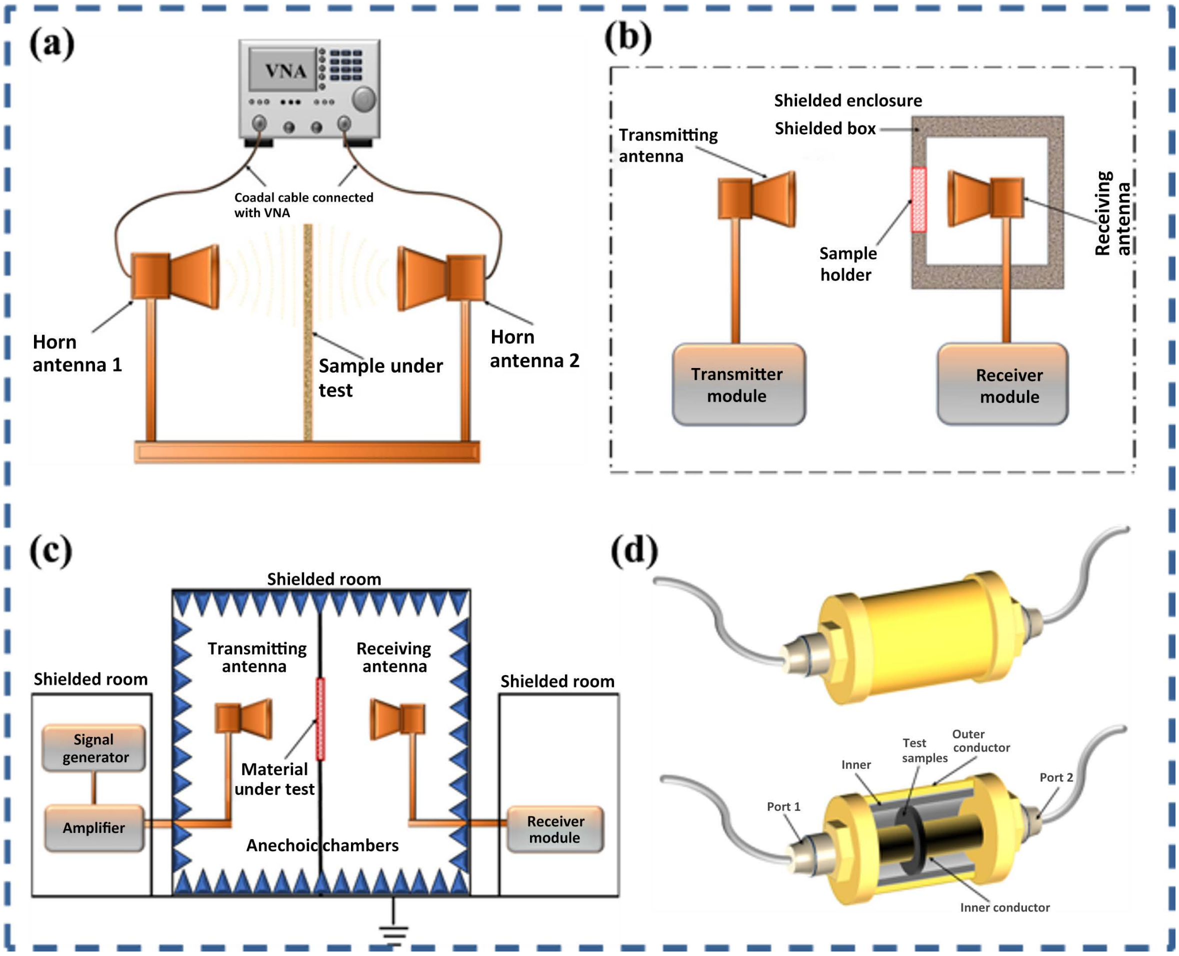

Figure 3 (a) Open field SE measurement. (b) SE measurement setup using a shielded box. (c) Shielded room SE measurement. (d) Coaxial transmission line fixture. Reproduced with permission from Ref. [98], © Wiley-VCH GmbH 2022.

of materials. It employs a metal enclosure with a small port on one wall, as illustrated in Fig. 3(b). An antenna inside the box acts as the receiver, while another outside serves as the transmitter. During testing, the port is first left open to measure received power without a sample. The sample is then placed over the port, and the received power is recorded with the VNA. This method is suitable for frequencies up to 500 MHz, but it suffers from poor electrical contact between the sample and container, as well as limited reproducibility between laboratories [101, 102].

To address these drawbacks, the shielding chamber method was developed, operating similarly to the shielding box approach but under stricter isolation conditions. In this method, the sample and antennas are placed in an anechoic chamber, while multiple shielding enclosures isolate EMWs from the receiver, signal generator, and power supply (Fig. 3(c)). This method currently supports frequencies up to 1 GHz, with ongoing efforts to extend the range beyond 10 GHz. It is considered the most complex approach, allowing sample sizes up to 2.5 m^2 to ensure data repeatability [103].

The coaxial transmission line method is the most widely applied technique for measuring EMI SE. It covers the frequency range of 30 MHz to 1.5 GHz, with extensions up to 18 GHz. The setup consists of transmitting and receiving coaxial cables, a VNA, and a metal sample holder. As shown in Fig. 3(d), the annular sample is mounted at the center of a 50 Ω coaxial unit tapered at both ends. The inner and outer conductors measure 4.35 and 9.9 cm, matching the sample dimensions. Shielding ability is determined by comparing input and output power using the VNA. Advantages of this method include compatibility with different conductor geometries (e.g., waveguides or coaxial lines) and small sample requirements, making it particularly suitable for TMDs and other nanomaterials [104–106].

Compared with antennas, coaxial cables exhibit significantly lower EMW loss, which enhances measurement accuracy. Moreover, the coaxial transmission line method enables separation of transmission, reflection, and absorption components, ensuring reliable SE data and consistent inter-laboratory results for the same sample.

4 TMDs for electromagnetic shielding

In recent years, 2D materials have become a major focus in materials science owing to their unique physical and chemical properties [107]. Among them, TMDs represent a distinct class of 2D materials that offer new opportunities in catalysis, energy storage, sensing, and electronics because of their rich chemistry and diverse electronic structures. TMDs follow the general formula MX_2, where M is a group IV–X transition metal (e.g., Mo, W, and Ta) and X is a chalcogen (S, Se, and Te). They possess a layered structure similar to graphene but exhibit greater electronic

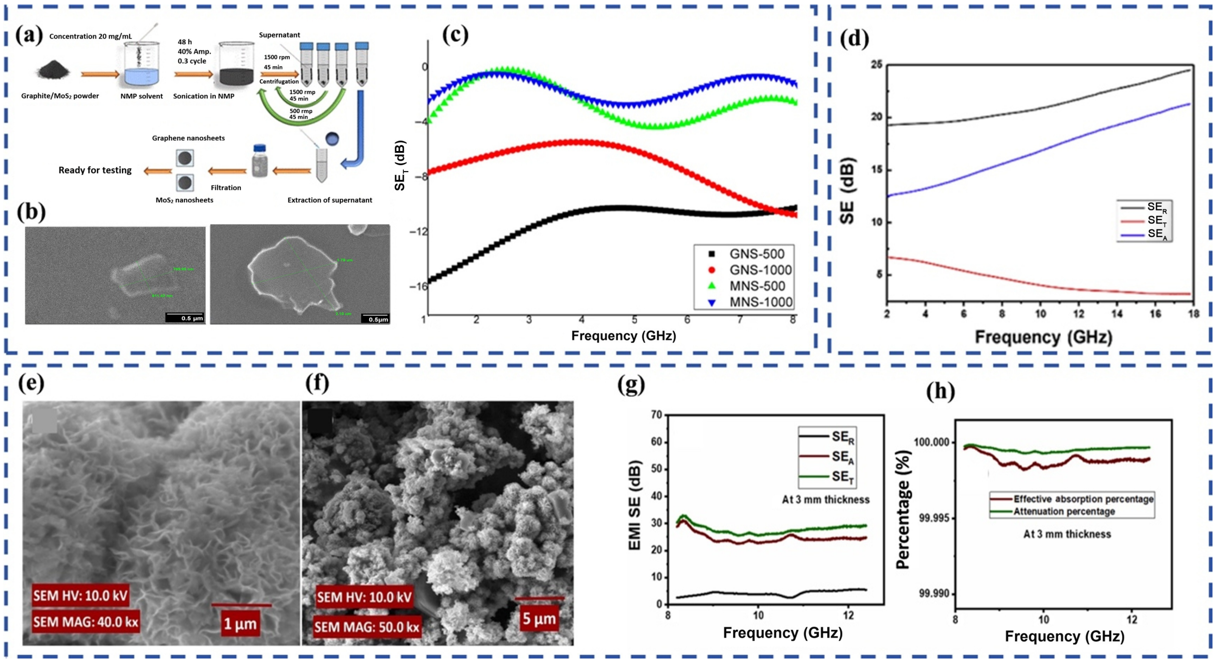

Figure 4 (a) Schematic representation of liquid phase exfoliation (LPE) method showing exfoliation of graphene and MoS_2 powder at 500 and 1000 rpm. (b) SEM representative images of exfoliated MoS_2. (c) EMI shielding effectiveness analysis (experimental) of GNS and MNS both for 1000 and 500 rpm as a function of frequency (1–8 GHz). Reproduced with permission from Ref. [128], © Khan, R. et al. 2020. (d) Attenuation performance of MoS_2 nanosheets prepared for 10 h. Reproduced with permission from Ref. [129], © Elsevier Ltd. 2019. Signifies FE-SEM images of MoS_2 nanoparticle at (e) low and (f) high magnification. (g) Shielding effectiveness due to absorption, reflection and total shielding, and effective absorption percentage. (h) Attenuation percentage for MoS_2 nanoparticles at 3 mm thickness. Reproduced with permission from Ref. [130], © Elsevier Ltd. 2025.

versatility and chemical activity [108].

A TMD monolayer comprises three atomic planes: one transition metal atom sandwiched between two chalcogen atoms, forming MX_2. Strong covalent bonds hold atoms within each layer, while weak van der Waals forces connect adjacent layers, allowing exfoliation into single layers [109]. These materials exhibit tunable band structures: Monolayers possess direct bandgaps, multilayers indirect bandgaps, and bandgap width can be adjusted by varying layer number. Such properties make TMDs highly attractive for applications in transistors, optoelectronics, photodetectors, photovoltaics, and energy storage [110, 111]. For example, monolayer MoS_2 devices achieve carrier mobilities up to 200 $cm^2/(V{\cdot}s)$ and on/off ratios above 10^8, making them promising candidates for flexible electronics.

Because the metal atom is sandwiched between chalcogens, a TMD monolayer is not truly monoatomic [112]. Bulk TMDs display diverse properties, ranging from insulating (e.g., HfS_2) to semiconducting (e.g., MoS_2, WS_2), semimetallic (e.g., $TiSe_2$, WTe_2), and metallic (e.g., VSe_2, NbS_2). Some compounds, such as TaS_2 and $NbSe_2$, also exhibit low-temperature phenomena including superconductivity, charge-density waves, and Mott transitions [113]. When exfoliated into single- or few-layer structures, many bulk properties are preserved, while quantum confinement introduces new features. Since the early 21st century, TMDs have also attracted interest for EMI shielding [108, 114].

MoS_2 occurs naturally as molybdenite and is an anisotropic semiconductor with distinct phases (1T, 2H, 3R) corresponding to tetragonal, hexagonal, and rhombohedral symmetries. Chemically exfoliated 1T MoS_2 exhibits higher conductivity than the 2H phase, although stabilizing the metallic 1T phase is challenging [115]. Hydrothermal methods enable preparation of heterostructures such as 1T-WS_2 and 1T/2H MoS_2. MoS_2 improves impedance matching with free space and exhibits excellent electromagnetic attenuation properties. Compared with graphene, MoS_2 has lower conductivity and dielectric constant but benefits from exceptional semiconductor properties and high dielectric loss, making it widely studied for EMI shielding [116].

WSe_2 offers unique electronic and optical properties that provide advantages over MXenes and graphene in electromagnetic applications. Its properties can be tuned through interlayer modification and chemical functionalization, while its flexibility is particularly beneficial in weight-sensitive applications such as aerospace. WSe_2 also demonstrates superior environmental and human health compatibility, supporting sustainable EMI shielding solutions [117].

$NbSe_2$, a metallic TMD, exhibits high conductivity and a large surface area due to its 2D structure, enhancing electromagnetic interactions. Combined with carbon nanotubes (CNTs), $NbSe_2$ shows synergistic improvements in shielding. Its superconductivity at low temperatures offers potential for specialized applications. However, its synthesis is complex, requiring precise control of parameters, which limits large-scale production. Moreover, its shielding effectiveness remains lower than that of more established materials, and its stability under environmental stress requires improvement.

TaS_2 is another emerging TMD that has gained attention. The 2H-TaS_2 phase exhibits metallic behavior, charge-density wave transitions, and superconductivity [118, 119]. Its electrical properties make it ideal for studying the influence of conductivity on EMI shielding. Exfoliation methods include electrochemical techniques, n-butyllithium intercalation, mechanical milling, and solvent-assisted ultrasonication [120–123]. However, these approaches suffer from low efficiency, poor reproducibility, and sensitivity to environmental conditions. Deng et al. [55] reported a practical intercalation method using concentrated LiOH under mild conditions to produce micron-scale 2H-TaS_2 nanosheets. Restacking these nanosheets via van der Waals interactions yielded flexible, self-supporting films (3.1 μm thick) with ultrahigh conductivity (2666 S/cm), EMI SE of 41.8 dB, SSE/*t* of 27,859 dB·cm²/g, tensile strength exceeding 23.3 MPa, and excellent flexibility.

Overall, only a limited number of TMDs, primarily MoS_2 and WSe_2, are widely used in EMI shielding. This limitation arises mainly from synthesis challenges, including precise parameter control and high production costs [124–127]. Other materials, such as $NbSe_2$ and TaS_2, suffer from stability issues and environmental sensitivity, which hinder long-term performance. Furthermore, their scarcity and high cost restrict practical applications, whereas MoS_2 and WSe_2 are easier to synthesize and more accessible, making them the preferred candidates for EMI shielding.

4.1 Pure TMDs

Khan et al. [128] investigated liquid-phase exfoliated molybdenum disulfide nanosheets (MNS) for electromagnetic shielding applications (Fig. 4(a)). By controlling centrifugation speed, nanosheets with lateral dimensions of ~ 2 (500 rpm) and ~1 μm (1000 rpm) were obtained (Fig. 4(b)). In the 1–8 GHz frequency range, the re-stacked MNS-500 sample achieved a SE of up to 6 dB (Fig. 4(c)). In contrast, Zhang et al. [129] synthesized MoS_2 nanosheets via a one-step hydrothermal method. Their SE was dominated by absorption attenuation with negligible reflection loss. Nanosheets prepared with a 10 h reaction time exhibited > 20 dB attenuation across 2–18 GHz (Fig. 3(d)). These MoS_2nanosheets not only combined facile synthesis with excellent shielding performance but also offered lightweight properties, corrosion resistance, and flexibility.

Building on these advances, Anwar et al. [130] synthesized MoS_2 nanoparticles with a petal-like morphology using a hydrothermal method. This hierarchical nanoflower structure, formed by ultrathin nanosheets (Figs. 4(e) and 4(f)), exhibited outstanding shielding performance and provided insights into the structure–property relationship. The ordered layered morphology enhanced charge transport and electromagnetic attenuation. As a result, the nanoparticles absorbed 99.9% of EMWs in the X-band (8.2–12.4 GHz), achieving SE_A of 29 dB and SE_T of 32 dB (Figs. 4(g) and 4(h)). The high attenuation efficiency was attributed to scattering effects, interfacial polarization, and dielectric losses induced by the nanoflower structure.

Beyond MoS_2 optimization, researchers have also investigated other promising TMDs, such as $NbSe_2$ and TaS_2. Luxa et al. [131] synthesized layered $NbSe_2$ and evaluated its shielding performance. After exfoliation with a high-shear homogenizer, micron-sized nanosheets (~ 10–90 nm thick) were obtained, displaying preferential orientation during vacuum filtration (Fig. 5(a)). The resulting $NbSe_2$ film, ~ 203 μm thick (Fig. 5(b)), exhibited excellent X-band SE_T, reaching 31.4 dB (Fig. 5(c)). Deng et al. [55] employed a green lithium-ion intercalation method to mass-produce 2H-TaS_2 nanosheets, which were restacked into flexible self-supporting films via van der Waals interactions (Fig. 5(d)). A 3.1 μm TaS_2 film achieved an EMI SE of 41.8 dB in the X-band (Fig. 5e) and an exceptional SSE/*t* of 27,859 dB·cm²/g (Fig. 5(f)).

To address scalability challenges in metallic TMDs such as $NbSe_2$, Kang et al. [56] proposed an optimized lithium-ion intercalation-assisted exfoliation strategy (Fig. 5(g)). By controlling energy input (mechanical stirring, ultrasonication), temperature, and ultrasonic power, they achieved high-yield production of monolayer $NbSe_2$ nanosheets. Compared with mechanical mixing, this process, aided by temperature–ultrasound synergy, significantly expanded the interlayer spacing of $NbSe_2$, improving monolayer yield. Morphology and Raman analyses confirm high-quality monolayer structures (Fig. 5(h)). Leveraging its metallic conductivity, a conductive film was prepared by vacuum-filtering a dispersion of $NbSe_2$ onto a polyethersulfone (PES) membrane. With only ~ 1.65 mg loading, the film achieved a SE_T of 20 dB in the X-band (Fig. 5(i)), meeting the threshold for commercial shielding (≥ 20 dB). Furthermore, Li et al. [78] demonstrated scalable, high-quality production of monolayer $NbSe_2$ via electrochemical exfoliation (Fig. 5(j)). The monolayers exhibited conductivity of 1.16 × 10^6 S/m (Fig. 5(k)), approaching metallic levels and surpassing MXenes and reduced graphene oxide (rGO). The optimized $NbSe_2$ film achieved a remarkable SE of 65 dB at only 5 μm thickness (Fig. 5(l)).

In the field of electromagnetic shielding, graphene has attracted significant attention due to its exceptional electrical properties. Pradip Kumar et al. [132] successfully developed high-performance reduced large-area graphene oxide (rLGO) films, which exhibited a conductivity of 243 ± 12 S/cm at a thickness of 7.5 μm and an EMI SE of 20 dB at 1 GHz. Qinwei Wei et al. [133] prepared pure graphene (PG) films that achieved high electromagnetic shielding effectiveness, with a conductivity of 1340 S/cm at a thickness of 4 μm, resulting in a shielding effectiveness of up to 38.1 dB. Zhu et al. [134] developed ultra-stable graphene aerogels (HGAs), which, while maintaining a thin thickness (1 mm), achieved an EMI SE of up to 64.1 dB, with a conductivity of 490.2 S/m. In terms of electromagnetic shielding performance, graphene excels even with minimal usage. However, challenges remain, such as the tendency for graphene sheets to agglomerate, weak interfacial interactions, and the presence of defects, all of which lead to less-than-ideal composite material performance.

In contrast to graphene, TMD materials offer moderate conductivity, tunable semiconductor properties, and superior overall performance and cost-effectiveness [135]. For example, MoS_2 nanoparticles synthesized by Anwar et al. [130] exhibited an absorption-dominated shielding mechanism in the X-band, with an effective absorption percentage of up to 99.9% and an SE_A of 29 dB, outperforming graphene's reflection-dependent shielding. Furthermore, the nanopetalous structure of MoS_2 not only provides a large specific surface area but also enhances mechanical stability and flexibility, whereas graphene requires composite materials to enhance its performance during processing [136]. Therefore, MoS_2 has better performance and broader application prospects in high-frequency electromagnetic shielding [137]. As shown in the table, both TaS_2 nanosheet flexible self-supporting films and monolayer $NbSe_2$ exhibit higher conductivity than most graphene materials. Under quantitative analysis, the electromagnetic SE of TaS_2 and $NbSe_2$, with the same thickness, exceeds that of rLGO films, PG films, and HGAs [132–134].

Compared to MXenes, which possess an extremely high intrinsic conductivity (≈ 5000 S/cm), TMD materials avoid the severe impedance mismatch with air that MXenes face [138]. When electromagnetic waves impinge upon the surface of MXenes, most of the energy is reflected back rather than absorbed [94]. This strong reflection causes secondary electromagnetic pollution, interfering with the normal operation of other precision

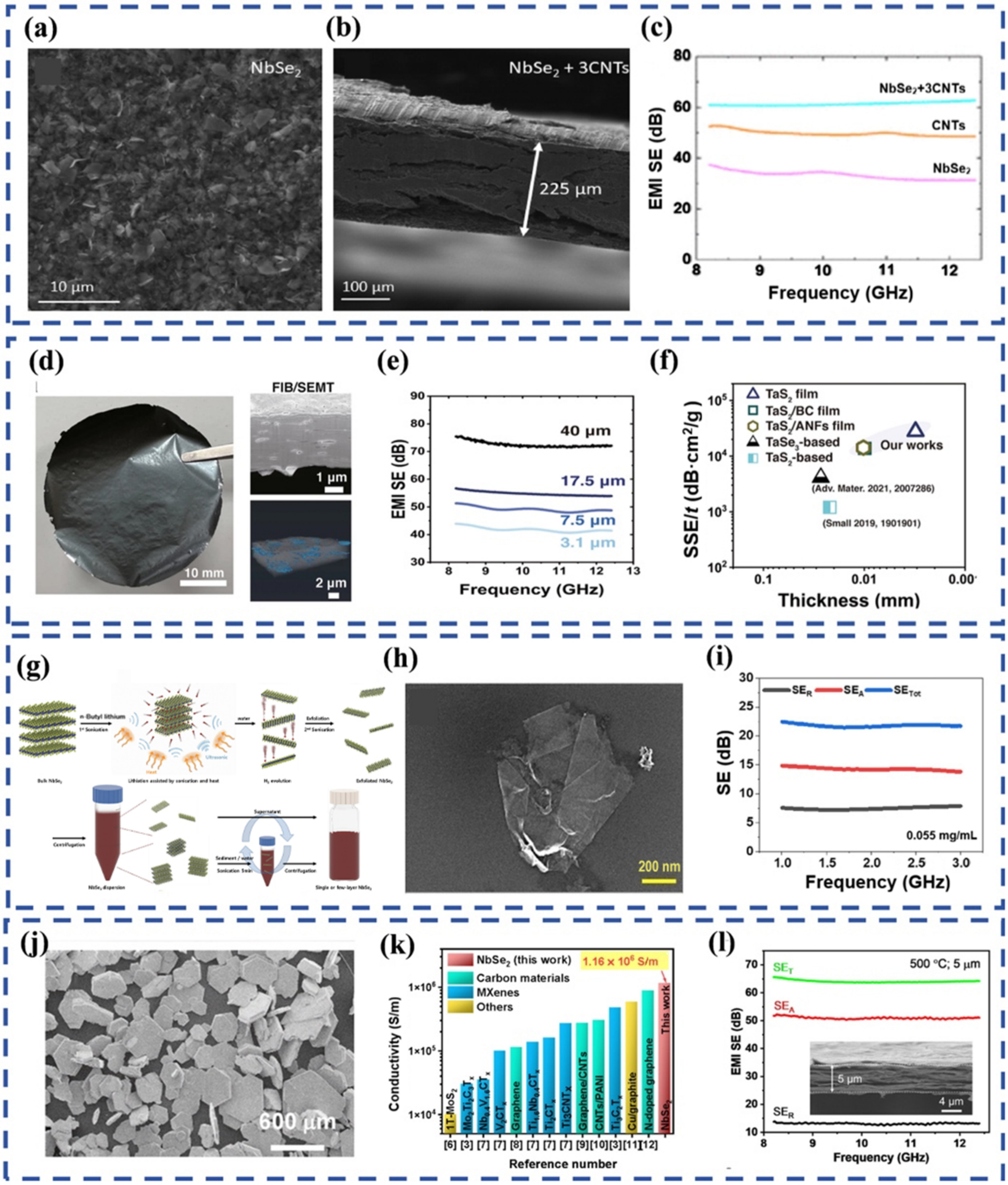

Figure 5 (a) SEM image of $NbSe_2$ from the top view. (b) SEM image of $NbSe_2$+3CNTs cross-sectional view with thickness. (c) EMI shielding performance in X-band: comparison of EMI SE for the as-prepared $NbSe_2$. Reproduced with permission from Ref. [131], © American Chemical Society 2023. (d) Structure characterizations of TaS_2 films. Photos, cross-sectional SEM images and 3D reconstruction microstructure based on FIB/SEMT of a TaS_2 freestanding film. (e) EMI SE of TaS_2 freestanding films at different thicknesses. (f) Comparison of EMI SSE/*t* of TaS_2 films with the reported TMDs-based EMI shielding materials. Reproduced with permission from Ref. [55], © Deng, F. K. et al. 2023. (g) Schematic image of Li-ion intercalation-assisted exfoliation using sonication. (h) SEM image of exfoliated $NbSe_2$ nanosheet. (i) SE_R and SE_A of 0.055 mg/ml, the best EMI SE performance. Reproduced with permission from Ref. [56], © Elsevier B.V. 2023. (j) SEM image of the flake $NbSe_2$ powder. (k) Comparison of the room-temperature electrical conductivity of the annealed $NbSe_2$ film with literature-reported values from different film materials. (l) SE_T, SE_A, and SE_R of the 5.0 μm thick $NbSe_2$ film annealed at 500 °C; the inset displays the SEM cross-section morphology of the film. Reproduced with permission from Ref. [78], © American Chemical Society 2024.

components within the same device, thus conflicting with the "green shielding" requirements of modern high-frequency, highly integrated electronic devices [89, 139]. The moderate conductivity and tunable bandgap of TMDs are their key advantages. Unlike metals, they are not as "rigid", allowing electromagnetic waves to penetrate the material more easily [140]. Through mechanisms such as dielectric relaxation, dipole polarization, and interface polarization, the electromagnetic energy is converted into thermal energy and dissipated [141]. This ultimately leads to high absorption and low reflection, achieving "green shielding" and fundamentally addressing internal electromagnetic interference [142]. Compared to MXenes, TMDs have undeniable advantages in terms of preparation processes, which constitute their core competitive edge for transitioning from the laboratory to industrial applications [143]. Specifically, the hydrogen fluoride etching step used in MXene synthesis is its unavoidable "Achilles' heel", bringing severe safety and environmental risks, as well as increasing process complexity and cost [144]. In contrast, TMDs (especially those synthesized via hydrothermal methods) follow green chemistry principles, requiring no harsh protective measures or waste treatment, significantly lowering the barriers to technology transfer [145]. Additionally, TMD nanosheets are more easily processed using mature solution-based methods and polymer composites, offering unparalleled flexibility for manufacturing next-generation flexible electronic devices [146]. Therefore, TMDs open up an ideal pathway that combines high performance, safety, and large-scale production feasibility, which is the key competitive advantage over MXenes [93]. As summarized in Table 1 and Fig. 6, TMDs and their composites demonstrate unique competitive advantages and innovative contributions in the field of EMI shielding compared to other alternative materials.

Despite these advances, pure TMDs face inherent limitations that restrict their practical use in electromagnetic shielding. Their mechanical properties are often inadequate; for instance, pure TaS_2 self-supporting films have a tensile strength of only 23.3 MPa and fracture easily under repeated bending, limiting their suitability for

Table 1 Comparison of representative shielding effectiveness data for TMD, MXene, and graphene shielding system

Category	Materials	Thickness	Frequency range (GHz)	EMI SE (dB)	Conductivity (S/cm)	Ref.
TMDs	TaS_2	3.1 μm	8.2–12.4	41.8	2666	[55]
	$NbSe_2$	5 μm	8.2–12.4	65	11,600	[78]
	MoS_2	7.5 μm	0.1–1.6	20	—	[190]
Graphene	rLGO	7.5 μm	1	15	243 ± 12	[132]
	PG	4 μm	8.2–12.4	38.1	1340	[133]
	GA	1 mm	8.2–12.4	32	49,020	[134]
MXene	MXene	—	8.2–12.4	50	22	[147]
	MXene	5 μm	8.2–12.4	21	8500	[138]
	Ti_3CNT_x	40 μm	8.2–12.4	61	1125	[148]
	$Ti_3C_2T_x$	40 μm	8.2–12.4	84	4500	[148]

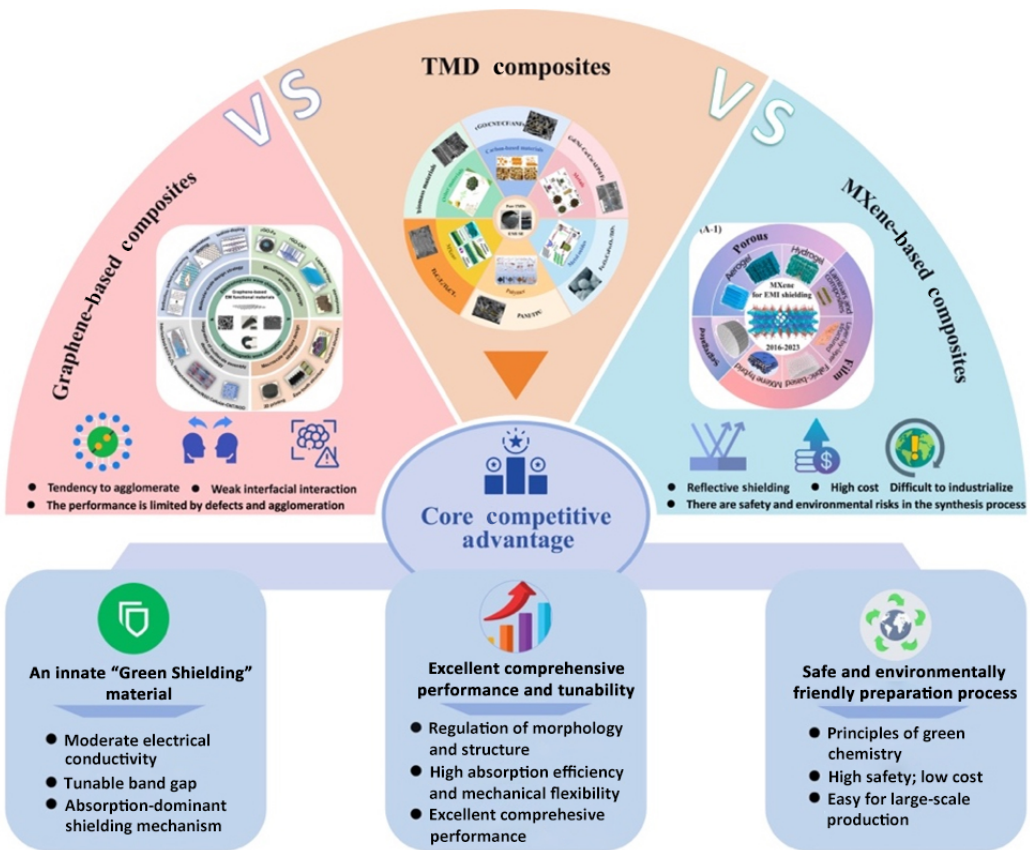

Figure 6 The unique advantages and innovative contributions of TMDs compared with other alternative materials. Reproduced with permission from Ref. [69], © Wiley-VCH GmbH 2022 and Ref. [70], © Elsevier Ltd. 2024, all rights are reserved, including those for text and data mining, AI training, and similar technologies.

flexible electronics [55]. In addition, the single-layer structure constrains electromagnetic loss mechanisms, while film compactness and interface stability affect long-term reliability. To overcome these issues, researchers have turned to TMD-based composites. By integrating TMD nanosheets with carbon, metals, metal oxides, polymers, or other nanomaterials, synergistic improvements can be achieved through electrostatic interactions, hydrogen bonding, or mechanical entanglement [62, 149–151]. This strategy not only enhances mechanical properties but also boosts electromagnetic losses by introducing multiple interfacial polarizations and optimizing conductive networks. For example, A free-standing TaS_2 film, which exhibits ultrahigh electrical conductivity, excellent mechanical flexibility, and outstanding EMI shielding performance, demonstrates a tensile strength of 23.3 MPa. By incorporating BC or aramid nanofibers to form composite films, the tensile strength can be further enhanced to 134.13 MPa while maintaining superior shielding performance (e.g., the TaS_2/BC composite film still achieves 46.8 dB). These characteristics enable such films to be directly applied in advanced electronic systems—such as flexible circuits and wearable devices—where stringent requirements for lightness, thinness, flexibility, and strength are essential [55].

The burgeoning field of flexible electronics, encompassing wearable health monitors, foldable smartphones, and conformal sensors for the Internet of Things (IoT), imposes stringent requirements on integrated functional materials, including those for EMI shielding [32, 152]. In these applications, shielding materials must not only provide effective protection against electromagnetic waves but also exhibit mechanical compliance, durability under repeated deformation, and low weight to ensure device comfort, portability, and long-term reliability [32, 120]. Conventional metal shields, such as thin copper or aluminum foils, are often inadequate due to their high density, susceptibility to fatigue cracking upon repeated bending, and potential for corrosion, which can compromise shielding integrity and device lifespan [36, 37]. Consequently, there is a pressing need for shielding materials that concurrently fulfill a combination of key performance metrics: high EMI SE, excellent flexibility (often quantified by a high number of bending cycles without failure), sufficient tensile strength, low density, and robust environmental stability (e.g., resistance to oxidation and moisture) [55, 152]. While TMDs offer intrinsic advantages such as tunable conductivity and a propensity for absorption-dominated shielding—aligning well with the demand for "green" shielding by minimizing secondary reflections [70, 72]—their standalone mechanical properties often fall short of the requirements for durable flexible electronics. This performance gap naturally leads to the exploration of composite strategies, which will be discussed subsequently in this section.

4.2 TMDs/carbon-based material

TMDs, with their layered structure, tunable bandgap, and abundant surface active sites, provide multiple pathways for electromagnetic wave (EMW) reflection and absorption [153]. Carbon-based materials such as graphene, carbon nanotubes (CNTs), bacterial cellulose (BC), and aramid nanofibers (ANFs) exhibit excellent conductivity, mechanical strength, and structural versatility, making them ideal scaffolds for efficient shielding networks [151–158]. When combined with TMDs via van der Waals forces, electrostatic interactions, or covalent bonds, these composites simultaneously enhance conductive pathways to improve reflection losses and exploit heterojunction polarization to strengthen absorption losses [159, 160]. Such interfacial coupling also preserves flexibility and mechanical stability [161–163]. This "1 + 1 > 2" synergistic effect enables TMD/carbon composites to meet the stringent EMI shielding requirements of modern electronics while overcoming the trade-offs of single-material systems.

Guo et al. [164] fabricated reduced graphene oxide@ molybdenum disulfide/polyvinylidene fluoride (rGO@MoS_2/PVDF) composites (Fig. 7(a)). At 25 wt.% rGO@MoS_2, the composite achieved a SE_T of 27.9 dB across 2–18 GHz (Fig. 7(b)), dominated by absorption (SE_A) (Fig. 7(c)). The heterojunction between rGO and MoS_2 enhanced interfacial and defect dipole polarization, while the rGO network improved conduction loss. Building on this, Singh et al. [165] synthesized CNT/MoS_2-rGO core–shell nanohybrids via a solvothermal method. MoS_2 encapsulated CNTs to form a core–shell structure anchored on rGO, generating a 3D conductive network (Fig. 7(d)). A 1 mm-thick CNT/MoS_2-rGO composite reached 40 dB SE_T (Fig. 7(e)), outperforming MoS_2 (7 dB) and MoS_2-rGO (28 dB). This improvement was attributed to interfacial and defect dipole polarization, high dielectric loss, electron migration in CNTs, and electron hopping between rGO layers, yielding absorption-dominated shielding (SEA ≈ 33 dB) (Fig. 7(f)).

Sajid et al. [166] prepared MoS_2/graphene nanoplatelet (GNP) nanocomposites by vacuum filtration. Layered structures were formed by varying concentration or arranging MoS_2 and GNPs in single, bilayer, and trilayer assemblies (Fig. 7(g)). At 0.5 wt.% GNPs, the layered MoS_2/GNP structure achieved 24 dB SE—14% higher than the 21 dB SE of physically mixed composites (Fig. 7(h))—with absorption ($SE_A \approx 16$ dB) as the dominant mechanism (Fig. 7(i)). The improvement stemmed from multiple interfacial polarization effects. Similarly, Uddin et al. [88] developed a MoS_2@waste tissue cellulose carbon (WTCC) hybrid by soaking and carbonizing MoS_2 nanosheets with WTCC. Acting as a low-conductivity filler, MoS_2 bridged cellulose fibers to form a conductive network and enhanced dielectric loss and scattering via its large surface area and multi-interface structure. At 10 wt.% MoS_2, the composite achieved a SE_T of 28 dB (Fig. 8(a)), dominated by absorption ($SE_A \approx 23$ dB, $SE_R \approx 5$ dB). A green shielding index ($g_s \approx 1$) indicated efficient absorption with minimal secondary reflection (Fig. 8(b)). This biowaste-derived composite highlights a sustainable route for EMI shielding, though broadband shielding remains essential for stable operation of multiple devices.

Zu et al. [77] fabricated flexible, hydrophobic CC/MoS_2 composites by anchoring MoS_2 nanosheets onto carbonized cotton fabric (CC) via a one-step hydrothermal method. The composites achieved > 20 dB SE across the J-band (5.85–8.2 GHz), X-band, and P-band (12.4–18 GHz), with CM-180 reaching 25.1 dB at 8.2 GHz and averaging 23.3 dB in the X-band (Fig. 8(c)). The cross-fiber structure of CC provided continuous conductive pathways, while MoS_2 nanosheets introduced additional interfaces, defects, and polarization sites. The periodic CC/MoS_2 structure induced negative dielectric behavior, enhancing impedance mismatch, whereas MoS_2's flower-like morphology and CC's hollow fibers extended EMW reflection paths, strengthening attenuation through scattering and interfacial polarization.

Dhanasekaran et al. [167] prepared ternary PANI/MWCNT/MoS_2 composites via in situ polymerization (Fig. 8(d)). At a fixed 5 wt.% MWCNT, composites with 5, 10, and 20 wt.% MoS_2 were tested. The 10 wt.% MoS_2 composite achieved 48.98 dB SE at

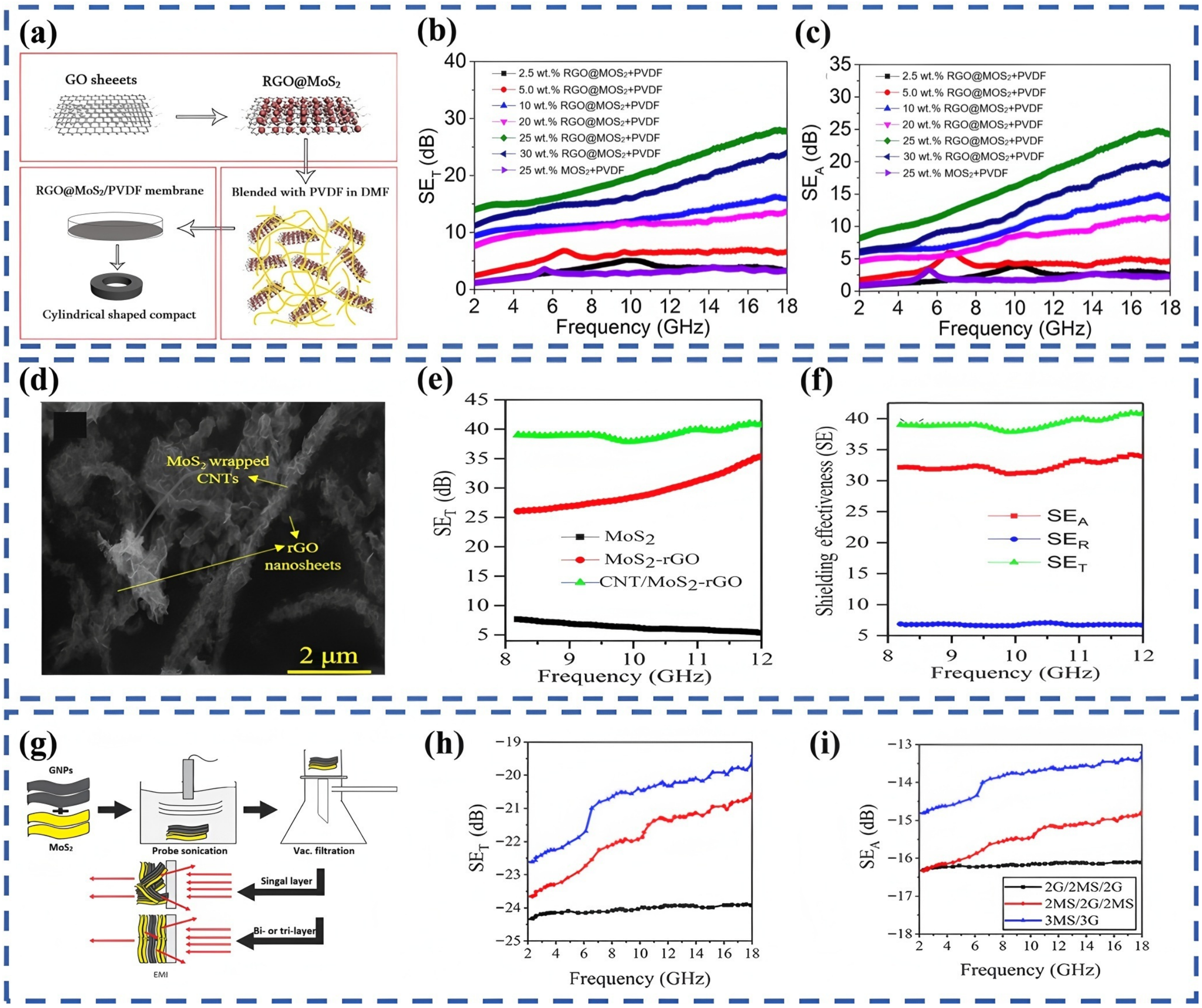

Figure 7 (a) Composites of reduced graphene oxide (rGO)@MoS_2/poly(vinylidene fluoride) (PVDF) have been prepared and investigated. (b) Frequency dependence of SE_T of the samples. (c) Frequency dependence of SE_A of the samples. Reproduced with permission from Ref. [164], © Wiley-VCH Verlag GmbH & Co. KGaA, Weinheim 2016. (d) SEM micrographs of CNT/MoS_2-rGO nanohybrids at low resolution; (e) SE_T of the as-synthesized samples in the X-band frequency range; (f) shielding effectiveness over the entire range of frequency of CNT/MoS_2-rGO nanohybrid in the X-band. Reproduced with permission from Ref. [165], © American Chemical Society 2020. (g) Schematic of single and multilayer structure fabrication processes as well as EMI mechanisms. EMI shielding effectiveness of bi- and trilayer structures: (h) total EMI shielding effectiveness and (i) absorption. Reproduced with permission from Ref. [166], © Zhou, J. Q. et al. 2022, published by American Chemical Society.

2.8 mm thickness (Fig. 8(e)). This enhancement was attributed to synergy between MoS_2 and MWCNTs, which improved impedance matching, conductivity, and EMW dissipation. Collectively, these studies validate the strategy of “TMD/carbon synergistic enhancement”, leveraging heterointerface polarization and 3D conductive networks to achieve absorption-dominated shielding while addressing requirements for green, low-reflection, and broadband adaptability.

To broaden the performance and application boundaries of TMD materials, researchers have gone beyond the limitations of MoS_2 and explored systems with unique properties, such as WS_2 (1T/2H phase coexistence), $NbSe_2$ (metallic conductivity), and TaS_2 (interlayer van der Waals modulation). These materials show significant advantages when combined with carbon materials: WS_2/rGO composites form mountain-wall structures to enhance wedge effects, $NbSe_2$/CNTs achieve near-metallic conductivity, and TaS_2/polymer fibers optimize the balance between mechanical and electrical properties. This extends the synergistic strategy beyond MoS_2, significantly improving SE, flexibility, and frequency adaptability.

Based on these characteristics, TMDs demonstrate clear application expansion value across multiple fields: In harsh environments such as high temperatures and high humidity, TMDs can be combined with ceramics like SiC and Si_3N_4 to create aerogels, foams, and other structural absorptive materials, offering high thermal stability, wide effective absorption bandwidth, and thermal insulation [168, 169]. These materials address the issues of traditional coatings such as poor adhesion and weatherability, making them suitable for aerospace, offshore wind power, and other fields [170]. In the flexible and wearable sectors, their two-dimensional flexible structure can be combined with polymers like polyimide and gels to form lightweight, stretchable thin films or fabrics for radiation shielding, meeting the needs of flexible electronics and wearable devices while offering excellent mechanical flexibility and biocompatibility [171, 172]. In multifunctional integration scenarios, the dielectric properties of TMDs can also be combined with thermoelectric and photonic functionalities, such as in composites with Sn@C, where microwave heat is used to build temperature gradients for “absorption-to-electricity conversion”, or by leveraging dielectric response changes for “absorption-to-sensing”

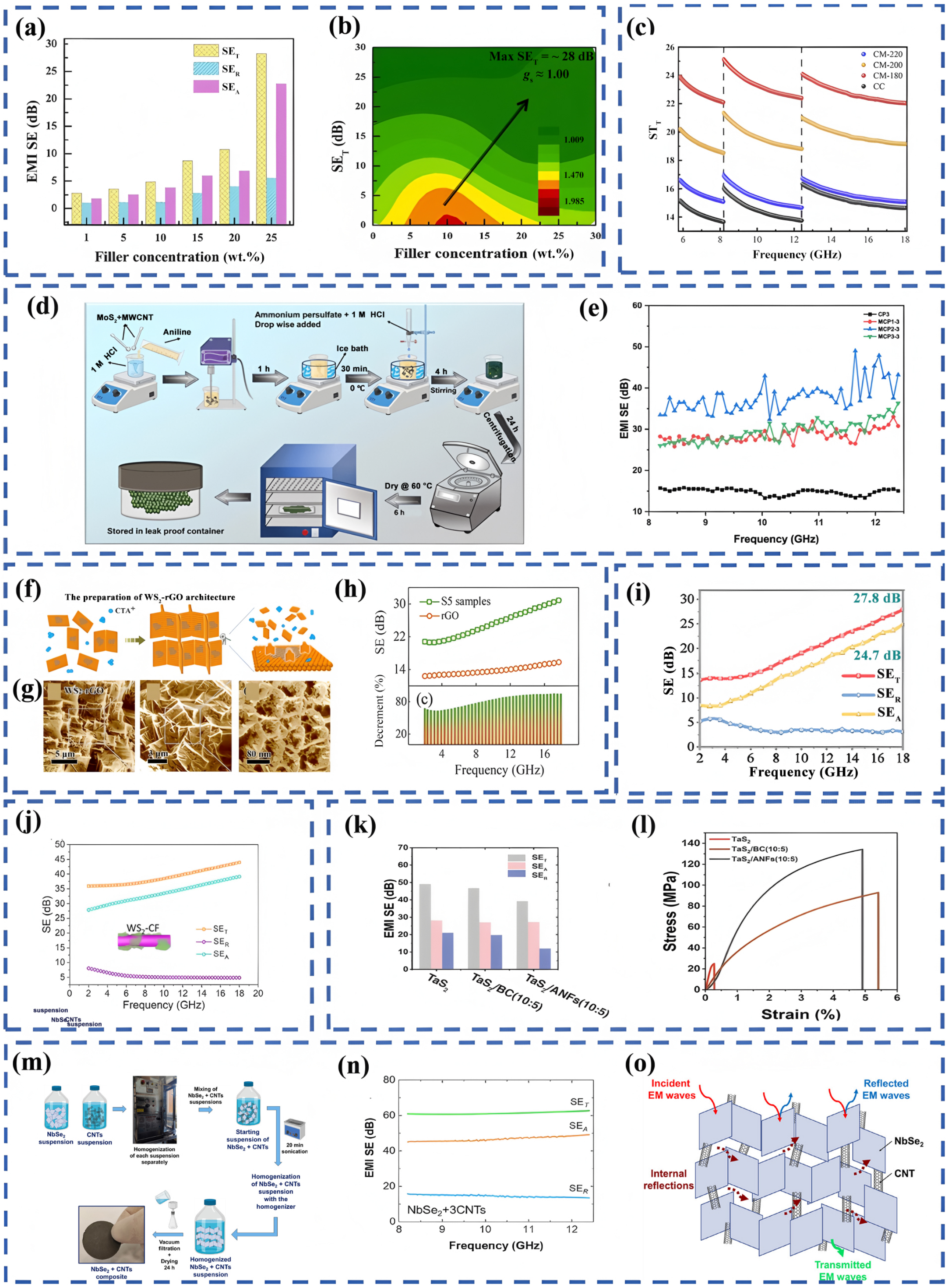

Figure 8 (a) Comparison of EMI SE performance at $f = 8$ GHz of MoS_2@WTCC/silicone resin composites with different filler loading. (b) Green shielding index (g_s) vs. filler concentration and SE_T of MoS_2@WTCC/silicone resin composites. Reproduced with permission from Ref. [88], © Elsevier Ltd. 2022. (c) Total electromagnetic shielding performance. Reproduced with permission from Ref. [77], © Elsevier Ltd. 2025. All rights are reserved, including those for text and data mining, AI training, and similar technologies. (d) Synthesis procedure of PANI/MoS_2/MWCNT. (e) SE_T of the 2.8 mm thick PANI/MWCNT and PANI/MoS_2/MWCNT composites. Reproduced with permission from Ref. [167], © American Chemical Society 2024. (f) Schematic illustration of fabricating 3D WS_2–rGO architecture. (g) SEM images of WS_2–rGO architecture in different resolutions. (h) SE of WS_2–rGO. Reproduced with permission from Ref. [87], © American Chemical Society 2019. (i) The SE of 5WS_2/CNTs-25. Reproduced with permission from Ref. [173], © IOP Publishing 2021. (j) The EMI shielding performance of WS_2-CF at a typical thickness of 3.00 mm. Reproduced with permission from Ref. [57], © The Chinese Ceramic Society 2021. Production and hosting by Elsevier B.V. (k) Average EMI SE_T, SE_A, and SE_R in 7.5-μm-thick TaS_2 freestanding film, TaS_2/BC (10:5), and TaS_2/ANFs (10:5) composite films. (l) Representative tensile stress–strain curves of TaS_2 freestanding film, TaS_2/BC (10:5), and TaS_2/ANFs (10:5) composite films. Reproduced with permission from Ref. [55], © Deng, F. K. et al. 2023. (m) Schematic illustration of the process used for the preparation of $NbSe_2$ + CNTs composites. (n) Total EMI SE (SE_T) and respective SE_R and SE_A contributions for $NbSe_2$ + 3CNTs. (o) Illustration of the possible EMI shielding mechanism in the $NbSe_2$ + 3CNTs composite. Reproduced with permission from Ref. [131], © American Chemical Society 2023.

(e.g., temperature/pressure monitoring) [168, 171]. These developments lay the foundation for cross-domain applications in medical and consumer electronics.

Zhang et al. [75] constructed WS_2-rGO mountain-wall composites via a "guest-first" self-assembly method (Figs. 8(f) and 8(g)). With 5% rGO, the composites achieved 32 dB SE_T across 2–18 GHz (Fig. 8(h)). Shielding arose from relaxation and conduction, multiple scattering at interfaces and voids, and wedge effects, which together enhanced EMW absorption and dissipation. Wang et al. [173] synthesized WS_2/CNT hybrids via hydrothermal synthesis and studied shielding from 2–18 GHz. At a WS_2:CNT ratio of 0.5:1 and 25 h reaction, the 5WS_2/CNT-25 composite reached 27.8 dB SE_T, dominated by absorption (Fig. 8(i)). This performance was attributed to WS_2's dielectric loss and the CNT network, which promoted multiple reflections, scattering, and polarization. Similarly, Zhang et al. [57] modified WS_2 nanosheets onto carbon fibers (CF) using a hydrothermal method. The 3 mm WS_2/CF composite achieved 36 dB SE_T at 2 GHz (S-band) (Fig. 8(j)), primarily due to enhanced SE_A. Shielding mechanisms included interface polarization, 1T and 2H multiphase defect scattering, and conduction loss. The composites also maintained stable performance after 300 bending cycles and 120 min of ultrasonication, demonstrating potential for flexible wearable applications.

Deng et al. [55] further reported TaS_2 composite films with excellent EMI shielding, high tensile strength, and flexibility. Using a green lithium-ion intercalation strategy, 2H-TaS_2 nanosheets were mass-produced and restacked into films. Combined with BC or ANFs via electrostatic interactions, the 7.5 μm TaS_2/BC and TaS_2/ANFs films achieved EMI SE values of 42 dB and 48 dB, respectively (Fig. 8(k)). The TaS_2/ANFs (10:5) composite reached a tensile strength of 134.13 ± 1.4 MPa. Van der Waals interactions between staggered nanosheets provided strain relaxation, while synergy with fibers optimized the mechanical–electrical balance (Fig. 8(l)).

Luxa et al. [131] pioneered a metallic $NbSe_2$/single-walled CNT composite foil for EMI shielding. Prepared by high-shear homogenization and vacuum filtration, the 219 ± 22 μm foil (Fig. 8(m)) achieved 62.7 dB SE_T at 12.4 GHz (X-band) (Fig. 7(n)), far exceeding pure $NbSe_2$ (31.4 dB) and CNTs (48.5 dB). CNTs enhanced conductivity to 2970 S/m and, together with $NbSe_2$, formed a 3D conductive network. Multiple reflections, polarization, and conduction losses further enhanced EMW attenuation (Fig. 8(o)). $NbSe_2$ thus offers high-frequency shielding at lower thickness and higher efficiency, while maintaining flexibility and stability, making it a strong candidate for 5G communications, wearables, and aerospace. Future work may further explore $NbSe_2$/carbon composites with emerging materials such as MXenes to push SE performance.

As EMI shielding materials evolve toward higher efficiency and multifunctional integration [144, 174, 175], TMD/carbon composites demonstrate clear synergistic advantages. Incorporating metals or metal oxides into multicomponent systems represents a promising strategy to further enhance performance [176–178]. TMDs provide abundant sites for polarization losses, carbon materials maintain conductive networks for reflection [179–181], and metals (Ag, Cu) or oxides (Fe_3O_4, TiO_2) contribute additional loss pathways through charge transfer, magnetic losses, and interfacial polarization [182–186]. This multidimensional synergistic framework—"TMDs control loss pathways, carbon maintains connectivity, metals/oxides compensate deficiencies"—not only delivers superior EMI SE but also improves flexibility, corrosion resistance, and environmental stability through interface engineering.

4.3 TMDs/metal and metal oxide-based material

Prasad et al. [187] synthesized gadolinium-doped MoS_2-rGO (Gd@MoS_2-rGO) nanocomposites via a two-step hydrothermal method to evaluate their EMI shielding in the X-band. Gd doping enhanced shielding, with 20% Gd@MoS_2-rGO achieving 20.47 dB SE_T (Fig. 9(a)), compared to 19.25 dB for 10% doping and 16.18 dB for undoped MoS_2-rGO. The improvement was attributed to Gd-induced conductive networks, which increased conductivity, dielectric loss, and interfacial polarization, facilitating charge migration across multiple interfaces. They also prepared Ni–Cu@MoS_2/rGO composites using the same method (Fig. 9(b)) [188]. Uniformly distributed 5–7 nm Ni–Cu nanoparticles yielded 33.47 dB SE_T at 1.8 mm thickness, compared with 7.17 dB for pure MoS_2 (Fig. 9(c)). The improvement arose from enhanced interfacial polarization, multiple reflections, and conductivity losses introduced by Ni–Cu, while the rGO network promoted electron migration, strengthening absorption loss. They further prepared Co-doped MoS_2/rGO nanocomposites [189]. A 20% Co@MoS_2/rGO sample achieved 46.02 dB SE_T at 1.7 mm, much higher than 28.90 dB for pure MoS_2/rGO (Fig. 9(d)). Co doping increased defect dipole polarization, conductivity, and interfacial polarization, forming conductive and magnetic channels that promoted microwave attenuation and dissipation.

Prasad et al. [190] fabricated 3D micro-flower Al-doped MoS_2/rGO nanohybrids with varying doping levels (Fig. 9(e)). At 12% Al doping, the nanohybrid achieved ~ 33.38 dB SE_T, nearly doubling the 17.07 dB of undoped MoS_2/rGO (Fig. 9(f)). The improvement was attributed to enhanced polarization and conductivity from Al doping, which induced lattice distortion and defect sites, increasing carrier mobility across interfaces and defects and thus boosting EMI SE. They also constructed 3D conductive bridges using bimetallic nanoparticles [191]. A 3D hierarchical Au–Ag@MoS_2-rGO nanohybrid was synthesized via hydrothermal–chemical methods (Fig. 9(g)), and its dielectric and EMI shielding properties were systematically studied. The nanohybrid, consisting of MoS_2-rGO nanosheets uniformly decorated with Au–Ag alloy nanoparticles, improved conductivity and charge transport via 3D conductive bridges, enhanced interfacial interactions, and provided abundant microwave absorption sites. In the X-band, the composite achieved 38.1 dB SE_T at just 1.5 mm thickness (Fig. 9(h)). Au–Ag nanoparticles served as efficient conductive interfaces, enhancing carrier transport, while combined conduction loss, polarization, and multiple reflections produced efficient EM energy dissipation.

Prasad et al. [192] also synthesized Pd-doped MoS_2/CNT nanohybrids with a hierarchical core–shell structure via hydrothermal methods. In this design, CNTs formed the core, while Pd-doped MoS_2 layers constituted the shell, producing a 3D heterostructure. At 1 mm thickness, 10% Pd-MoS_2/CNT achieved 26.50 dB SE_T, outperforming 5% Pd doping (22.50 dB) and undoped composites (21.55 dB) (Fig. 9(i)). The improvement was attributed to Pd-induced conductivity, defect dipole polarization, and interfacial polarization, with the core–shell structure enhancing scattering and dissipation at interfaces.

They also synthesized MoS_2–rGO/Fe_3O_4 nanocomposites via a two-step hydrothermal method and evaluated their X-band EMI

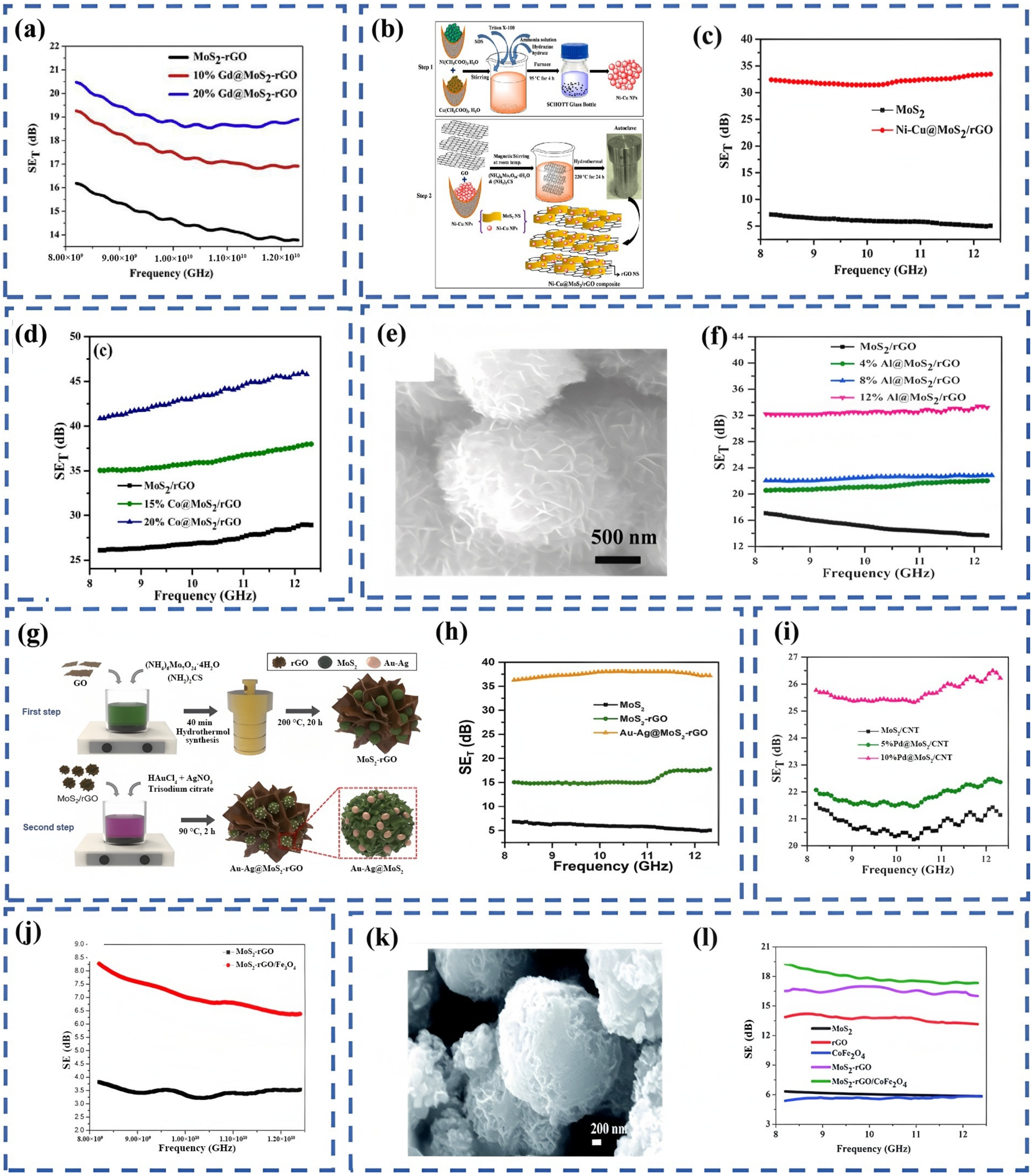

Figure 9 (a) The frequency dependence of EMI shielding effectiveness SE_T values of the nanocomposite in the X-band range. Reproduced with permission from Ref. [187], © Elsevier B.V. 2019. (b) Schematic representation of the synthesis procedure of Ni-Cu@MoS_2/rGO composite. (c) Frequency dependence of EMI cSE_T of MoS_2 and Ni–Cu@MoS_2/rGO composite in the frequency range of 8.0–12.0 GHz. Reproduced with permission from Ref. [188], © Springer Science+Business Media, LLC, part of Springer Nature 2019. (d) The frequency dependence of the EMI shielding effectiveness. Reproduced with permission from Ref. [189], © Springer Science Business Media, LLC, part of Springer Nature 2020. (e) SEM image of the flower-like microspheres 12% Al@MoS_2-rGO nanohybrids at high-magnification. (f) EMI shielding effectiveness of as-prepared samples. Reproduced with permission from Ref. [190], © Elsevier Ltd and Techna Group S.r.l. 2021. (g) Schematic synthesis steps for producing MoS_2, MoS_2-rGO, and Au-Ag@MoS_2-rGO nanohybrid. (h) Frequency-dependent EMI shielding characteristics: SE_T across the frequency range of 8.2–12.4 GHz. Reproduced with permission from Ref. [191], © Elsevier B.V. 2024. (i) Microwave frequency dependence of EMI SE of undoped MoS_2/CNT and Pd–MoS_2/CNT core-shell nanohybrids. Reproduced with permission from Ref. [192], © Elsevier Ltd and Techna Group S.r. 2021. (j) The variation of shielding effectiveness. SE_T values of MoS_2-rGO and MoS_2-rGO/Fe_3O_4 nanocomposite with frequency in the range of 8.0–12.0 GHz. Reproduced with permission from Ref. [193], © IOP Publishing, Ltd. 2018. (k) Typical SEM pictures of as-prepared MoS_2-rGO/$CoFe_2O_4$ at high magnification. (l) SE_T values of MoS_2, rGO, $CoFe_2O_4$, MoS_2-rGO, and the MoS_2-rGO/$CoFe_2O_4$ nanocomposite in the X-band range. Reproduced with permission from Ref. [194], © The Royal Society of Chemistry 2019.

shielding [193]. Spherical Fe_3O_4 nanoparticles (25–30 nm) were uniformly dispersed within the MoS_2–rGO matrix. The nanocomposite reached 8.27 dB SE_T, over double that of MoS_2–rGO (3.81 dB) (Fig. 9(j)). The improvement was attributed to Fe_3O_4-induced interfacial polarization, electromagnetic polarization, and magnetic loss, which improved impedance matching.

Prasad et al. [194] further synthesized MoS_2–rGO/$CoFe_2O_4$ nanocomposites via a two-step hydrothermal method. $CoFe_2O_4$ nanoparticles (8–12 nm) were uniformly distributed on the MoS_2–rGO surface, forming a 3D structure (Fig. 9(k)). The composite achieved 19.26 dB SE_T, higher than MoS_2–rGO (16.52 dB) (Fig. 9(l)), due to $CoFe_2O_4$-induced interfacial polarization, defect dipole polarization, and magnetic loss, which improved impedance matching. Multiple interfaces facilitated charge migration and synergistically enhanced absorption loss ($SE_A \approx 12.62$ dB), demonstrating strong EMI shielding potential.

The Prasad group has conducted systematic and innovative studies on TMD/metal and metal oxide nanocomposites for EMI shielding. Using MoS_2 as the core TMD, they designed composites doped with single metals (Gd, Co, Al, and Pd), bimetallic/alloys (Ni-Cu, Au-Ag), or metal oxides (Fe_3O_4, $CoFe_2O_4$), often combined with carbon-based materials (rGO, CNTs). They further introduced innovative structures such as 3D micro-flowers, hierarchical core–shells, and 3D conductive bridges. These composites improved conductivity, interfacial polarization, and defect dipole polarization via doping/combination, while introducing magnetic loss, thereby enhancing X-band EMI SE. They systematically examined structure–performance relationships among doping concentration, structural design, and shielding, providing clear strategies for optimizing MoS_2-based shielding. Notably, similar efforts by other groups on diverse TMD/metal and metal oxide systems have enriched fabrication strategies and broadened application scenarios.

Sharma et al. [195] investigated synergistic effects of micron-scale MoS_2 and steel slag in a geopolymer matrix, developing composites for EMI shielding in buildings (Fig. 10(a)). Using MoS_2 or steel slag alone yielded 20 and 24 dB SE, respectively. At a 40 wt.% ratio, the

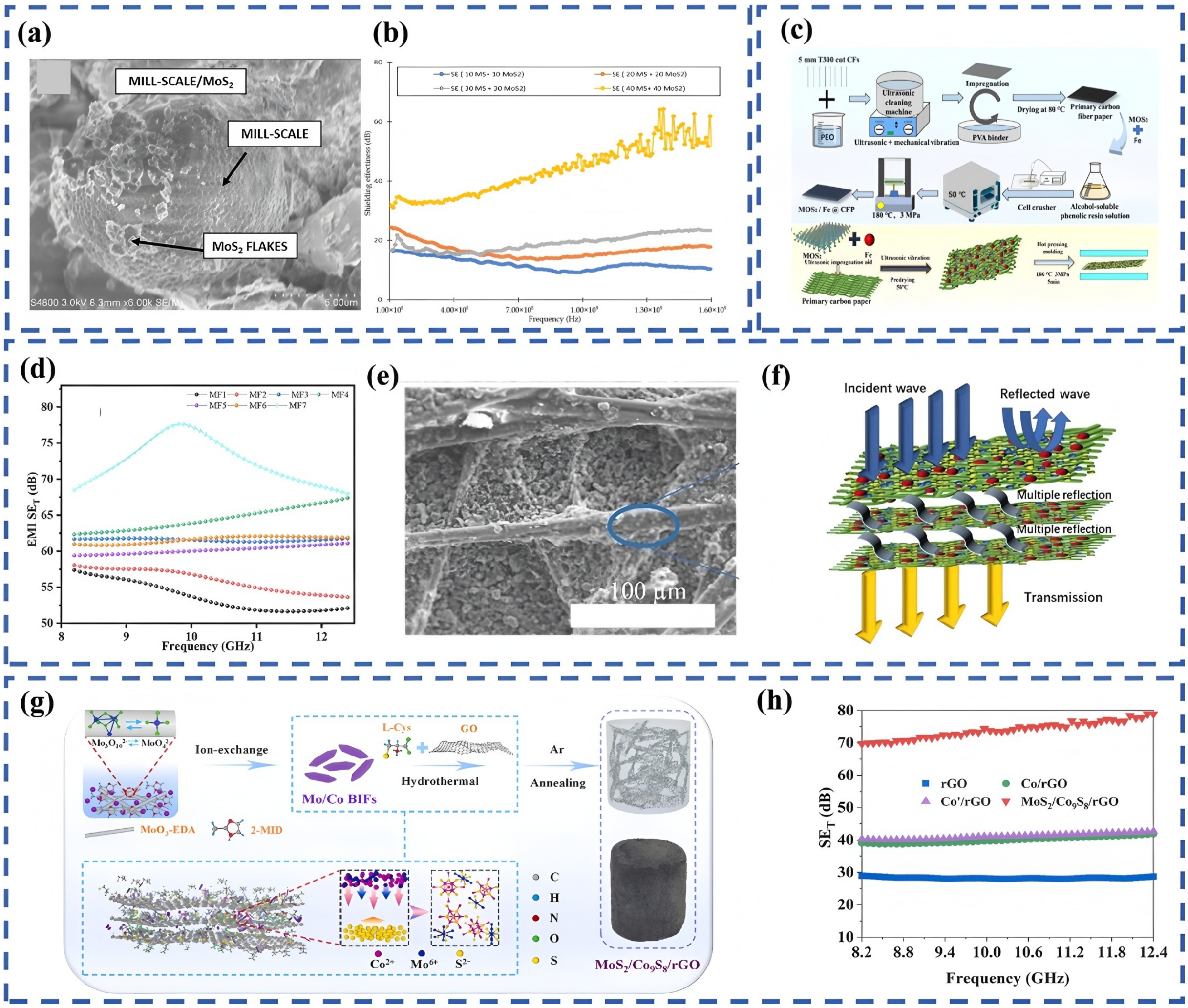

Figure 10 (a) Scanning electron microscopy of Mill scale/MoS_2 geopolymer. (b) EMI shielding effectiveness of Mill scale/MoS_2 geopolymer composite with equal percentage of each filler. Reproduced with permission from Ref. [195], © Sharma, R. et al. 2022, under exclusive licence to Springer Science Business Media, LLC, part of Springer Nature. (c) The process of carbon fiber paper preparation and Schematic diagram of electromagnetic shielding paper synthesis. (d) SE_T values of MF1 to MF7. (e) High magnification SEM view of MF7. (f) Electromagnetic shielding mechanism. Reproduced with permission from Ref. [196], © Liu, Z. et al. 2023, under exclusive licence to Korean Carbon Society. (g) Schematic of the preparation processes for MoS_2/Co_9S_8/rGO aerogel. (h) SE_T of rGO, Co/rGO, Co'/rGO and MoS_2/Co_9S_8/rGO composites. Reproduced with permission from Ref. [197], © Elsevier B.V. 2024.

combined composite achieved 65 dB SE (Fig. 10(b)). The synergy arose from MoS_2 conductivity and steel slag magnetization, which enhanced shielding via reflection and absorption. The composite also satisfied building compressive strength standards, confirming its feasibility for EMI-shielded construction. Liu et al. [196] fabricated MoS_2/Fe@carbon fiber paper (CFP) composites in varying ratios using wet paper-making, impregnation, blending, and hot pressing (Fig. 10(c)). The MF7 sample (MoS_2:Fe = 10:3) achieved 77.63 dB SE (Fig. 10(d)) while remaining lightweight, stable, and mechanically robust. This performance was attributed to synergy between dielectric MoS_2 and magnetic Fe, which, together with the CF matrix, created a robust conductive network (Figs. 10(e) and 10(f)). Ren et al. [197] proposed a Kirkendall effect-based strategy, constructing Mo/Co bimetallic imidazole frameworks (BIFs) via ion exchange. Through hydrothermal self-assembly and pyrolysis, they prepared MoS_2/Co_9S_8 heterostructure nanoparticles (HNPs) uniformly confined within a 3D rGO aerogel (Fig. 10(g)). In the X-band, a MoS_2/Co_9S_8/rGO composite with 40% loading and 1.8 mm thickness achieved 73.9 dB SE, far exceeding single TMD or rGO-based materials (Fig. 10(h)). Abundant defects in MoS_2/Co_9S_8 HNPs generated internal electric fields that accelerated charge transport, while interfaces within the rGO aerogel strengthened interfacial and dipole polarization, synergistically improving conductivity and EM loss.

4.4 TMDs/polymer

Although TMD/metal and metal oxide nanocomposites exhibit strong EMI shielding performance through synergistic dielectric and magnetic losses, their practical use remains limited. The high density of metallic components increases composite weight, conflicting with lightweight design requirements. Moreover, bonding between metal oxides and TMD nanosheets often depends on weak physical adhesion, which may peel under bending or stretching, compromising structural stability. These composites are also typically rigid, reducing compatibility with flexible electronics such as wearable sensors and communication devices [152, 198].

To overcome these limitations, polymers have emerged as attractive matrix materials [47, 199–201]. With low density, high flexibility, and excellent interfacial compatibility, polymers form stable composites with TMD nanosheets through covalent, electrostatic, and van der Waals interactions [202–204]. This improves mechanical flexibility and processability [205–208], while their tunable electrical properties—charge transport in conductive polymers and dielectric polarization in insulating polymers—enable synergistic control of EMW loss mechanisms with TMDs. Consequently, TMD/polymer nanocomposites have become a key research direction, bridging "high electromagnetic performance" with "practical applicability". These composites retain the advantages of TMDs in interfacial polarization and charge transport while overcoming the weight, rigidity, and stability limitations of metal/oxide-based systems.

Saboor et al. [209] prepared PS/PANI/MoS_2 hybrid composites via solution casting. At 5 wt.% PANI and 1 wt.% MoS_2, the composite achieved a theoretical SE of 92 dB at 100 Hz (Fig. 11(a)), attributed to increased dipoles at insulator–conductor interfaces. Menon et al. [210] developed a biomimetic self-healing PU-Dopa nanocomposite, integrating dopamine-functionalized polyurethane with MWNTs and Fe_3O_4@MoS_2. The composite achieved 36.6 dB SE_T across 8–18 GHz (Fig. 11(b)). Uniform dispersion of fillers prevented aggregation, while dopamine groups optimized polarization loss and provided flexibility, ensuring stable shielding performance even after mechanical damage.

Khan et al. [128] produced MoS_2 nanosheets via liquid-phase exfoliation and dispersed them in thermoplastic polyurethane (TPU). Lower centrifugation speed (500 rpm) achieved larger nanosheet size, and the resulting TPU composites achieved ~ 1.02 S/m DC conductivity and 0.02 S/m AC conductivity at 1 GHz, with broadband SE up to 18 dB (Fig. 11(c)). Sharma et al. [211] advanced this system by preparing rGO/MoS_2–TPU foams through water vapor-induced phase separation (Fig. 11(d)). Hydrothermally synthesized rGO/MoS_2 heterostructures prevented nanosheet restacking, enhancing foam performance. At 7 wt.% filler, the composite achieved ~ 32 dB SE_T at 3 mm thickness in the X-band (Fig. 11(e)), 28% higher than rGO–TPU and 166% higher than MoS_2–TPU. Multiple reflections within the microporous rGO/MoS_2 structure boosted attenuation and improved thermal, mechanical, and tensile properties, demonstrating feasibility for practical applications.

Dhanasekaran et al. [167] synthesized ternary PANI/MWCNT/MoS_2 composites via *in situ* polymerization. With 5 wt.% MWCNT, the 10 wt.% MoS_2 composite achieved 48.98 dB SE at 2.8 mm thickness (Fig. 11(f)). They also prepared PANI/TiO_2/MoS_2 composites [212], where a formulation containing 10 wt.% TiO_2 and 20 wt.% MoS_2 reached 50.86 dB SE at 3 mm in the X-band (Fig. 11(g)). These results were attributed to the synergistic effects of MoS_2 and TiO_2 in enhancing impedance matching, conductivity, and EMW dissipation, while PANI provided continuous conductive pathways and improved interfacial polarization.

Zhou et al. [213] fabricated PANI/MoS_2/CF composites by hydrothermally growing MoS_2 nanosheet networks on CF and functionalizing them with PANI. The system achieved integrated structure–function EMI shielding. MoS_2 nanosheets interlocked mechanically with CF, while PANI reinforced bonding with the PEEK matrix via π–π interactions. The composite exhibited a 63.9% increase in interlayer shear strength, reaching 96.62 MPa, while achieving a SE_T of 40.71 dB in high-frequency scenarios (Fig. 11(h)), a 91% improvement over unmodified CF/PEEK.

4.5 TMDs/MXenes

TMD/polymer nanocomposites leverage the low density, high flexibility, and interfacial tunability of polymer matrices to address the limitations of metal- and metal oxide-based composites in lightweight and flexible applications [214, 215]. However, their electromagnetic performance is constrained by the intrinsic electrical properties of polymers [200, 205, 206]. Insulating polymers enhance dielectric polarization but cannot form efficient conductive networks for strong reflection loss, while conductive polymers such as polyaniline and polypyrrole, although superior to insulators, remain far less conductive than metals or carbon-based materials [204]. This limits their effectiveness in higher-frequency electromagnetic fields, such as those encountered in millimeter-wave (mmWave) 5G communications [203]. Moreover, traditional thermoplastic resins may degrade or swell under heat and humidity, reducing both electromagnetic performance and structural stability.

To overcome these challenges, researchers have turned to MXenes [216–219], which combine ultra-high conductivity (10^4–10^5 S/m) with a 2D layered structure [220]. MXenes form efficient conductive networks that enhance reflection loss while their abundant surface groups (–OH, –F, –O) establish hydrogen

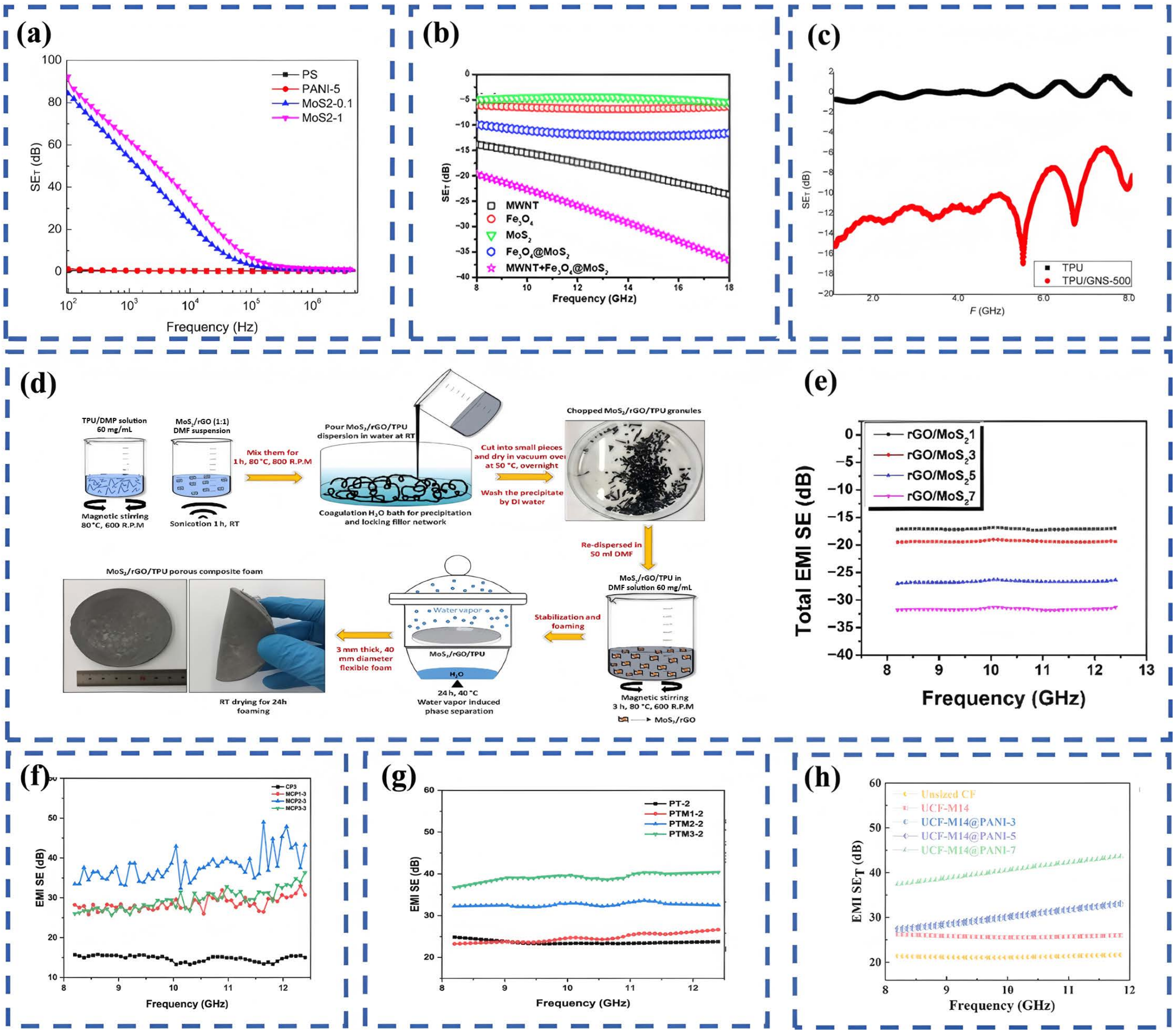

Figure 11 (a) EMI shielding behavior of PS, PANI, PS/PANI-5 wt.% polymer blend, and PS/PANI/MoS_2 hybrid polymer composites at various concentrations of MoS_2 on the basis of SE_T. Reproduced with permission from Ref. [209], © Saboor, A. et al. MDPI 2019. (b) Total shielding effectiveness. Reproduced with permission from Ref. [210], © American Chemical Society 2019. (c) Experimental EMI shielding effectiveness results for TPU and TPU/GNS-500 Composite based on s-parameters as a function of frequency (1–8 GHz). Reproduced with permission from Ref. [128], © Khan, R. et al. 2020. (d) Schematic diagram for the preparation of porous rGO/MoS_2/TPU composite foam by the water-induced phase separation (WVIPS) technique. (e) Total EMI shielding effectiveness of different concentrations of rGO/MoS_2 determined in the X band (8.2–12.4 GHz) frequency range. Reproduced with permission from Ref. [211], © Elsevier Ltd. 2022. (f) SE_T of the 2.8 mm thick PANI/MWCNT and PANI/MoS_2/MWCNT composites. Reproduced with permission from Ref. [167], © American Chemical Society 2024. (g) SE_T of the 1.75 mm thick PANI/TiO_2 and PANI/MoS_2/TiO_2 composites. Reproduced with permission from Ref. [212], © Dhanasekaran, A. et al. 2025. Published by American Chemical Society. (h) SE_T in X band. Reproduced with permission from Ref. [213], © Elsevier Ltd. 2025. All rights are reserved, including those for text and data mining, AI training, and similar technologies.

bonds, electrostatic interactions, and other interfacial effects with TMD nanosheets, yielding stable 2D/2D heterostructures [221–224]. The structural compatibility between MXenes and TMDs further promotes synergistic electromagnetic loss through interfacial polarization, multiple reflections, and charge transfer, while offsetting the conductivity limitations of polymer-based systems [225–227]. As a result, TMD/MXene composites have emerged as a promising strategy to achieve high shielding effectiveness, structural stability, and wide-band adaptability, offering a pathway beyond polymer-based systems.

While MXenes and TMD/MXene composites demonstrate exceptional shielding performance in the X-band, their potential extends to the higher-frequency spectrum critical for next-generation wireless communications. The K-band (18–26.5 GHz) is of particular importance as it falls within the designated frequency range for 5G mmWave applications, where efficient EMI shielding is essential to protect high-speed data links. Promisingly, several composite systems reviewed in this work exhibit outstanding performance in this very band. For instance, the biomass-derived MoS_2/N-doped PCH composite reported by Rezaei et al. [54] achieves nearly 100% EMI shielding efficiency in the K-band, showcasing the potential of TMD-hybrid systems for high-frequency applications. Furthermore, the TMD/MXene system itself proves highly effective, as evidenced by the work of Anand et al. [228], where a PDA-modified MXene/TaS_2 (MXT) film achieved a remarkable shielding effectiveness of 62 dB within the K-band. These results directly underscore the capability of TMD/MXene composites to operate effectively in the high-frequency regime required for advanced 5G mmWave shielding, positioning them as compelling candidates for future flexible and high-performance electronics.

Several studies highlight the advantages of this approach. Xing et al. [229], inspired by the layered structure of pork belly, fabricated an ultrathin MXene@AgNW@MoS_2 (MAM) composite film via vacuum-assisted filtration and atomic layer deposition (Fig. 12(a)). The film comprised alternating MXene/AgNW-doped and AgNW layers with MoS_2 nanosheets as the outer layer. AgNWs built a 3D conductive network, while multilayer heterointerfaces enhanced reflection and scattering. The MoS_2 surface optimized impedance matching, achieving an absorption rate of 83.7% and minimizing secondary reflections. Only 0.03 mm thick, the MAM film reached 86.3 dB SE in the X-band (Fig. 12(b)), driven by synergistic conduction loss, interfacial polarization, and dielectric loss.

Ahmed et al. [230] fabricated $Ti_3C_2T_x$ MXene/MWCNT@MoS_2

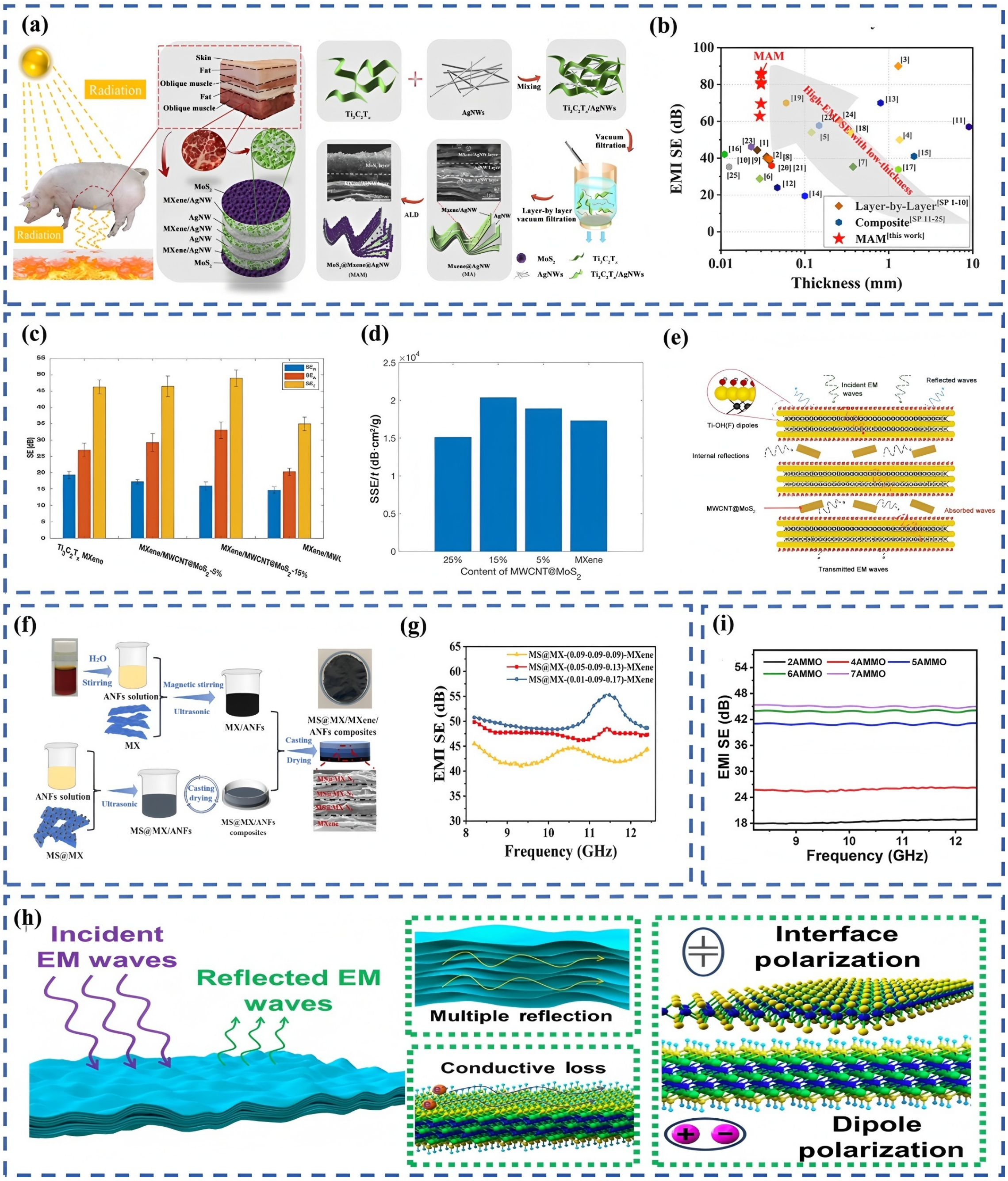

Figure 12 (a) Schematic illustration of the preparation process of MAM. (b) Comparison of EMI SE with previous reports. Reproduced with permission from Ref. [229], © American Chemical Society 2023. (c) Average SE_A, SE_R, and SE_T values for $Ti_3C_2T_x$ MXene and heterogeneous films. (d) Comparison of EMI SSE/*t* of $Ti_3C_2T_x$ and heterogeneous films. (e) Proposed mechanism of EMI shielding for the heterogeneous film. Reproduced with permission from Ref. [230], © Ahmed, S. et al. 2023, published by American Chemical Society. (f) Schematic illustration of ANFs and gradient structure MS@MX/MXene/ANF composite film fabrication process. (g) EMI SE value of MS@MX-(N1-N2-N3)-MXene composites. Reproduced with permission from Ref. [231], © Elsevier B.V. 2024, all rights are reserved, including those for text and data mining, AI training, and similar technologies. (h) EMI shielding effectiveness of ternary MXene/ANF–MoS_2 composite films in X-band. (i) EMI shielding mechanism diagram of ternary MXene/ANF–MoS_2 composite films. Reproduced with permission from Ref. [116], © Wang, J. E. et al. 2024, published by *Nano-Micro Letters*.

heterostructure films via vacuum-assisted filtration. At 15 wt.% MWCNT@MoS_2, the composite achieved 50 dB SE (Fig. 12(c)), surpassing pure MXene (46 dB), with an SSE/t of 20,355 dB·cm^2/g (Fig. 12(d)). This enhancement arose from high conductivity, porous structures introduced by MWCNT@MoS_2, and multiple interface effects that improved reflection and internal scattering (Fig. 12(e)). Importantly, after 35 days of exposure, the SE dropped by only 13%–32% compared with 35%–45% for pure MXene, due to the hydrophobicity of MWCNT@MoS_2, which suppressed MXene oxidation.

Liu et al. [231] introduced a gradient-structured MoS_2@MXene/MXene/aramid nanofiber (ANF) composite prepared by hydrothermal synthesis and layer casting (Fig. 12(f)). The design enabled an "absorption–reflection–reabsorption" shielding mechanism. Low-conductivity MS@MX/ANF surface layers reduced initial reflection, a middle gradient layer facilitated penetration and absorption, and high-conductivity MXene/ANF bottom layers reflected residual EM waves for secondary loss. This 0.15 mm film achieved 50.9 dB SE in the X-band (Fig. 12(g)).

Wang et al. [116] fabricated a shell-like MXene/ANF–MoS_2 ternary composite film using vacuum-assisted filtration, self-assembly, and hot pressing (Fig. 12(h)). MoS_2 improved the toughness of the MXene/ANF system and, together with MXene, constructed an efficient conductive network. The composite achieved 43.9 dB SE in the X-band (Fig. 12(i)), while multiple interfacial polarizations reduced SE_R, minimizing secondary electromagnetic pollution.

In summary, TMD/MXene composites demonstrate significant potential as lightweight, flexible, and high-performance EMI shielding materials [232]. Synergistic interactions between TMDs and MXenes yield efficient conductive networks and multiple heterointerfaces, enhancing conduction and polarization losses [233, 234]. TMDs improve impedance matching, suppress secondary reflections, and enhance flexibility and aging resistance. These ultrathin composites offer promising applications in flexible electronics, aerospace, and other advanced technologies, providing a new pathway for the development of next-generation shielding systems.

4.6 TMDs/other materials

In addition to the materials mentioned above, the combination of TMD composites with emerging materials such as bio-based matrices, conductive polymers, or metal-organic frameworks (MOFs) holds great promise for advancing electromagnetic shielding materials [86]. Bio-based matrices provide a sustainable and environmentally friendly option for electromagnetic shielding materials [235]. Their combination with TMDs is expected to reduce the environmental impact of materials without sacrificing performance. Conductive polymers, due to their unique electrical properties and processability, can be combined with TMDs to form composites with synergistic effects, further enhancing electromagnetic shielding effectiveness [236]. MOFs, with their highly ordered porous structures and tunable chemical compositions, can not only improve the electromagnetic shielding performance of the material when combined with TMDs but also enable multiple reflections and absorptions of electromagnetic waves through their porous structures, thereby enhancing electromagnetic compatibility [237]. The development and application of these composite materials will drive further advancements in electromagnetic shielding technology, particularly in fields such as 5G communication, aerospace, and smart wearables, where there is an increasing demand for high performance, lightweight, and multifunctional materials, offering more effective solutions to the issue of electromagnetic pollution [238–240].

In recent years, biomass materials and their derivatives have garnered significant attention in EMI shielding research due to their renewability, low cost, biodegradability, and wide availability [241]. Depending on their composition, biomass electromagnetic interference materials can be classified into pure biomass electromagnetic shielding materials, metal/biomass electromagnetic shielding composites, inorganic non-metallic/biomass electromagnetic shielding composites, and biomass/polymer electromagnetic shielding composites [242]. In this context, Rezaei et al. [54] treated pyrolyzed corn cob with plasma-assisted nitrogen doping and combined it with MoS_2 nanoflowers to create a composite material (MoS_2/N-doped PCH) with excellent microwave absorption and shielding performance. This material exhibited nearly 100% electromagnetic interference shielding efficiency in the K-band (18–26.5 GHz), with a maximum RL of −95.32 dB and an effective bandwidth (RL ≤ −10 dB) of 7.61 GHz, with a thickness of only 0.45 mm. This study highlights the unique advantages of biomass materials, such as corn cob, in electromagnetic functional materials [243]. Their natural porous structure, high surface area, and self-doping characteristics (such as the presence of nitrogen functional groups) not only promote interface and defect polarization but also enhance multiple reflections and scattering of electromagnetic waves [244]. Additionally, the biomass material composite has good degradability and environmental friendliness, showcasing a green and efficient design strategy for microwave shielding materials, while offering new insights into the synergistic application of two-dimensional transition metal dichalcogenides and biomass carbon [245, 246].

It is worth noting that bio-inspired artificial materials have also provided innovative design concepts for EMI shielding. Bio-inspired materials, such as polydopamine (PDA), have emerged as effective interfacial modifiers that significantly enhance the overall performance of two-dimensional transition metal dichalcogenide nanocomposites [247]. For instance, Anand et al. [228] modified MXene with PDA and combined it with TaS_2 nanosheets to fabricate MXT films. The study found that the introduction of PDA not only acted as a "nano-adhesive" to strengthen interlayer interactions but also promoted the ordered arrangement of the nanosheets through electrostatic repulsion, enhancing the tensile strength and toughness of the composite film to 92 MPa and 2.49 MJ/m^3, respectively. At the same time, PDA modification optimized the charge transport pathway, resulting in a film conductivity of up to 7932 S/cm, allowing the composite to achieve an electromagnetic interference shielding effectiveness of 62 dB in the K-band. This work highlights the significant potential of bio-inspired materials in developing high-performance, stable electromagnetic shielding materials.

5 Challenges in environmental stability of TMD composites

In the research on TMD composites, particularly MXene-based materials, environmental stability (such as oxidation and moisture sensitivity) remains a key challenge limiting their practical applications [248]. To address this issue, several research teams have reported effective solutions. Ahmed et al. [230] introduced MWCNT@MoS_2 clusters into $Ti_3C_2T_x$ MXene to construct a heterogeneous structure film. The study found that the introduction of MoS_2 not only expanded the interlayer spacing of MXene but also significantly enhanced the hydrophobicity of the film. The water contact angle increased from 44.7° for pure MXene to 57.0°, indicating that the enhanced hydrophobicity effectively blocked moisture penetration, thereby slowing down the oxidation process of MXene. Wang et al. [116] reported MXene/ANF-MoS_2 ternary composite films, which, through the design of a nacre-inspired layered structure, achieved excellent interlayer arrangement and compactness. This structure not only improved the mechanical properties but also significantly enhanced the material's stability in humid environments by reducing the diffusion pathways for moisture and oxygen. Anand et al. [228] proposed a self-aligning strategy based on electrostatic repulsion, combining PDA-modified MXene with negatively charged TaS_2 nanosheets. PDA not only acted as an adhesive to enhance interlayer interactions but also formed a physical barrier that effectively prevented the infiltration of oxygen and moisture into MXene. The study further pointed out that the catechol groups in PDA have antioxidant properties, capable of scavenging reactive oxygen species, thus delaying the oxidation process of MXene. After 60 days of environmental exposure, the conductivity, electromagnetic shielding performance, and thermal conductivity of the composite film remained stable, demonstrating excellent environmental durability. These studies indicate that through surface hydrophobic modification, structural densification design, and encapsulation strategies combined with antioxidant coatings, the environmental durability of TMD composites can be systematically enhanced [247]. This lays a solid foundation for their long-term, reliable application in flexible electronics and electromagnetic interference shielding [249].

6 Conclusion and prospects

6.1 Conclusion

TMDs, with their layered structure, tunable electronic properties, and excellent physicochemical stability, have demonstrated significant potential in EMI shielding, making them strong candidates to replace traditional metal-based materials. Table 2 summarizes the thickness, EMI SE and conductivity of some recent transparent EMI shielding materials using them. The key achievements in current research are summarized in Fig. 13. This review provides a comprehensive discussion of various TMD composite systems in the field of EMI shielding and systematically outlines the design principles and core objectives of these composite materials.

(1) TMD-carbon composite materials

The design principle of TMD-carbon composites is to leverage the synergy between TMDs' dielectric polarization properties and the high conductivity of carbon materials. Carbon materials form a conductive network, facilitating charge migration and conductive loss, while TMDs introduce polarization centers such as interfaces, defects, and dipoles, which convert electromagnetic energy into heat. The combination of these elements optimizes impedance matching and induces multiple loss mechanisms, resulting in absorption-dominated electromagnetic shielding. TMDs also enhance interface polarization, improve charge accumulation, and prevent the agglomeration of carbon materials, ensuring efficient absorption and minimal reflection, which aligns with "green shielding" principles.

(2) TMD-metal and metal oxide composite materials

In TMD-metal and metal oxide composites, the design focuses on structural enhancements such as three-dimensional porous or flower-like heterostructures that improve specific surface area, stability, and electromagnetic losses. TMDs serve as polarization enhancers and structural supports, promoting dielectric loss and improving impedance matching. The three-dimensional structure of TMDs prevents nanoparticle agglomeration, while their defects act as dipoles and electron traps, enhancing dielectric loss and polarization relaxation. These composites achieve absorption-dominated shielding, with significant improvements in performance, especially in the X-band, while maintaining lightweight properties.

(3) TMD-polymer composite materials

In TMD/polymer composites, the design focuses on enhancing dielectric loss, polarization, and flexibility. TMDs, with their two-dimensional layered structure, promote dipolar and interface polarization, improving dielectric loss and wave absorption. Their moderate conductivity adjusts impedance matching with free space, optimizing electromagnetic shielding performance. TMDs also enhance the mechanical properties, flexibility, and stability of the composite, ensuring effective and versatile shielding in flexible electronics and wearable devices. The combination of TMDs with

Table 2 EMI SE of pure TMDs and TMDs-based nanocomposites

Category	Materials	Thickness	Frequency range	EMI SE (dB)	Conductivity	Ref.	Reporting date
Pure TMDs	MoS_2	1.8 mm	8.0–12.0 GHz	7.17 dB	—	[188]	2019
	MoS_2	—	1–8 GHz	6 dB	—	[128]	2020
	MoS_2	—	2–18 GHz	20 dB	—	[129]	2019
	MoS_2	1 mm	8–12 GHz	7 dB	—	[165]	2020
	WS_2	3 mm	2–18 GHz	5 dB	—	[173]	2022
	MoS_2	7.5 μm	0.1–1.6 GHz	20 dB	50 S/m	[192]	2022
	$NbSe_2$	203 μm	8.2–12.4 GHz	31.4 dB	—	[131]	2023
	TaS_2	3.1 μm	8.2–12.4 GHz	41.8 dB	2666 S/cm	[55]	2023
	$NbSe_2$	—	8.2–12.4 GHz	20 dB	—	[56]	2023
	$NbSe_2$	5/48 μm	8.2–12.4 GHz	65/113 dB	11,600 S/cm	[78]	2024
	MoS_2	3 mm	8.2–12.4 GHz	32 dB	—	[130]	2025

(Continued)

Category	Materials	Thickness	Frequency range	EMI SE (dB)	Conductivity	Ref.	Reporting date
Carbon-based materials	rGO@MoS_2/PVDF	—	2–18 GHz	27.9 dB	—	[164]	2016
	MoS_2-rGO	—	8.0–12.0 GHz	3.81 dB	—	[193]	2018
	MoS_2-rGO	—	8.0–12.0 GHz	16.52 dB	—	[194]	2019
	CNT/MoS_2-rGO	1 mm	8–12 GHz	40 dB	43 S/m	[165]	2020
	MoS_2-rGO	1 mm	8–12 GHz	28 dB	18 S/m	[165]	2020
	MoS_2/rGO	1.7 mm	8.0–12.0 GHz	28.9 dB	~ 75 S/m	[189]	2020
	MoS_2/rGO	—	8.0–12.0 GHz	17.07 dB	~ 28 S/m	[190]	2021
	MoS_2/CNT	1 mm	8.0–12.0 GHz	21.55 dB	~ 52 S/m	[192]	2021
	MoS_2/GNPs	—	2–18 GHz	24 dB	—	[166]	2022
	MoS_2@WTCC	—	8.2–12.4 GHz	28 dB	—	[88]	2022
	$NbSe_2$+CNTs	219 ± 22 mm	8.2–12.4 GHz	62.7 dB	2970 S/m	[131]	2023
	PANI/MoS_2/MWCNT	2.8 mm	8.2–12.4 GHz	48.98 dB	—	[167]	2024
	MoS_2/MWCNT	2.8 mm	8.2–12.4 GHz	38 dB	—	[167]	2024
	WS_2-rGO	—	2–18 GHz	32 dB	3.658 S/cm	[87]	2019
	WS_2/CNTs	—	2–18 GHz	27.8 dB	—	[173]	2021
	WS_2/CF	3 mm	2–18 GHz	36 dB	—	[57]	2022
	TaS_2/ANFs	7.5 μm	8.2–12.4 GHz	42 dB	1517 S/cm	[55]	2023
	TaS_2/BC	7.5 μm	8.2–12.4 GHz	48 dB	1435 S/cm	[55]	2023
	CC/MoS_2	0.5 mm	8.2–12.4 GHz	25.1 dB	—	[77]	2025
Metals and metal oxides	20%Gd@MoS_2-rGO	—	8.0–12.0 GHz	20.47 dB	~ 0.02 S/cm	[187]	2019
	MoS_2-rGO	—	8.0–12.0 GHz	16.18 dB	0.001 S/cm	[187]	2019
	Ni–Cu@MoS_2/rGO	1.8 mm	8–12 GHz	33.47 dB	—	[188]	2019
	20%Co@MoS_2/rGO	1.7 mm	8.0–12.0 GHz	46.02 dB	~ 150 S/m	[189]	2020
	12%Al@MoS_2/rGO	—	8.0–12.0 GHz	33.38 dB	~ 80 S/m	[190]	2021
	10%Pd-MoS_2/CNT	1 mm	8.0–12.0 GHz	26.5 dB	~ 130 S/m	[192]	2021
	MoS_2/Mill scale	—	0.1–1.6 GHz	65 dB	0.002 S/cm	[195]	2022
	MoS_2/Fe@CFP	—	8.0–12.0 GHz	77.63 dB	48.45 S/cm	[196]	2024
	MoS_2/Co_9S_8/rGO	1.8 mm	8.2–12.4 GHz	73.9 dB	~ 1.75 S/cm	[197]	2024
	Au-Ag@MoS_2-rGO	1.5 mm	8.2–12.4 GHz	38.1 dB	~ 85 S/m	[191]	2024
	MoS_2-rGO/Fe_3O_4	—	8.0–12.0 GHz	8.27 dB	—	[193]	2018
	MoS_2-rGO/$CoFe_2O_4$	—	8.0–12.0 GHz	19.26 dB	—	[194]	2019
Polymer	PS/PANI/MoS_2	—	100 Hz–5 MHz	92 dB	1.076×10^{-8} S/cm	[209]	2019
	MWNTs/Fe_3O_4@MoS_2	—	8–18 GHz	36.6 dB	~ 1.3×10^{-3} S/cm	[210]	2019
	MoS_2/TPU	—	1–8 GHz	18 dB	—	[128]	2020
	rGO/MoS_2/TPU	3 mm	8.2–12.4 GHz	32 dB	23.78 S/m	[211]	2023
	PANI/MoS_2/MWCNT	2.8 mm	8.2–12.4 GHz	48.98 dB	—	[167]	2024
	PANI/TiO_2/MoS_2	3 mm	8.2–12.4 GHz	50.86 dB	—	[212]	2025
	PANI/MoS_2/CF	—	8.0–12.0 GHz	40.71 dB	~ 38.42 S/cm	[213]	2025
MXene	MXene@AgNW@MoS_2	0.03 mm	8.2–12.4 GHz	86.3 dB	~ 2260 S/cm	[229]	2024
	Mxene-MWCNT@MoS_2	—	8.2–12.4 GHz	50 dB	~ 2800 S/cm	[230]	2023
	MoS_2@MXene/MXene/ANF	0.15 mm	8.2–12.4 GHz	50.9 dB	~ 15 S/cm	[231]	2024
	MXene/ANF-MoS_2	—	8.2–12.4 GHz	43.9 dB	~ 27,500 S/m	[116]	2025
	MXene/TaS_2	16.5 mm	8.2–12.4 GHz	62 dB	~ 7932 S/cm	[228]	2025

conductive fillers further improves polarization and enhances shielding effectiveness.

(4) TMD-MXene composite materials

The design of TMD/MXene composites aims to optimize electromagnetic wave absorption through gradient and multi-layer structures that enhance interface polarization and reflection. TMDs regulate the electromagnetic properties, improving impedance matching and promoting absorption-dominated shielding. The heterojunctions formed between TMDs and MXenes induce strong interface polarization, which enhances wave absorption and

Figure 13 Systematic summary of design principles and design objectives for various TMD composites in the field of electromagnetic shielding.

conversion. TMDs also contribute to the mechanical strength, moisture resistance, and oxidation stability of the composite, expanding its potential applications in advanced technologies like flexible electronics and smart response systems (e.g., photothermal and electrothermal conversion).

6.2 Prospects

Despite significant progress in the research of TMD-based composites, their transition to practical application still faces multiple challenges. One of the core issues lies in the incomplete decoupling of various loss mechanisms—such as interfacial polarization at heterojunctions, defect-induced dipole polarization, and charge transport in hybrid conductive networks—which constrains the rational design and predictability of material performance. Future efforts must integrate in situ characterization and multiscale theoretical modeling to clarify the intrinsic relationships within the "structure–defect–interface–property" framework. At the same time, with the evolution of communication technologies toward 6G, the effective frequency range for electromagnetic protection must extend from the GHz band into the terahertz (THz, 0.1–10 THz) regime. Terahertz waves, characterized by higher frequencies and shorter wavelengths, impose more stringent demands on the microstructural design and impedance matching of materials. Accordingly, research focus should shift toward intelligent structural design tailored for the THz band, such as constructing gradient conductivity profiles, alternating electromagnetic layers, or core–shell fiber-based multiscale heterogeneous architectures. These designs can establish gradual impedance distributions and multiple scattering interfaces within the material, thereby reconciling the inherent conflict between high conductivity and good impedance matching, and ultimately enabling ultra-broadband, absorption-dominant electromagnetic shielding from GHz to THz frequencies.

Further advancement requires precise control over defects and interfaces at the atomic scale, along with the use of spatially heterogeneous structures—such as multilayered, porous, or Janus (dual-asymmetric) configurations—to enhance polarization relaxation and conductive loss in the THz band. This promotes an "absorption–reflection–reabsorption" cycle of electromagnetic waves within the material, improving shielding effectiveness while suppressing secondary electromagnetic pollution. Moreover, TMD composites must address key challenges related to environmental stability, multifunctional integration, and scalable manufacturing. Future electromagnetic shielding materials should evolve toward multifunctional integration, incorporating capabilities such as THz shielding, infrared stealth, photothermal conversion, sensing, or energy storage to meet the comprehensive protection needs of flexible electronics, wearable devices, aerospace, and other fields in complex environments. Ultimately, bridging the gap between fundamental material research and scalable fabrication processes will unlock the full potential of TMD composites for future all-spectrum communication and advanced electronic technologies.

Data availability

Not applicable.

Acknowledgements

The work was financially supported by the National Key R&D Program of China (No. 2023YFB3811301) and Guangxi Special Program on Talent Training for Agriculture and Rural Revitalization (No. GXQNTJ242126).

Declaration of competing interest

All the contributing authors reports no conflict of interests in this work.

Author contribution statement

L. L. X.: Data curation, project administration, validation, writing manuscript. F. X. H.: Data curation, writing manuscript. D. B. N.: Project administration, writing manuscript. K. L.: Project administration, funding acquisition. Y. G. H.: Project administration. F. K. D.: Project administration, funding acquisition, writing manuscript. All the authors have approved the final manuscript.

Use of AI statement

None.

References

[1] Chen, Y. H.; Meng, Y.; Zhang, J. Y.; Xie, Y. H.; Guo, H.; He, M. K.; Shi, X. T.; Mei, Y.; Sheng, X. X.; Xie, D. L. Leakage proof, flame-retardant, and electromagnetic shield wood morphology genetic composite phase change materials for solar thermal energy harvesting. *Nano-Micro Lett.* **2024**, *16*, 196.

[2] Hou, X.; Feng, X. R.; Jiang, K.; Zheng, Y. C.; Liu, J. T.; Wang, M. Recent progress in smart electromagnetic interference shielding materials. *J. Mater. Sci. Technol.* **2024**, *186*, 256–271.

[3] Lee, H.; Ryu, S. H.; Kwon, S. J.; Choi, J. R.; Lee, S. B.; Park, B. Absorption-dominant mmWave EMI shielding films with ultralow reflection using ferromagnetic resonance frequency tunable M-type ferrites. *Nano-Micro Lett.* **2023**, *15*, 76.

[4] Li, X. F.; Chen, C. Y.; Li, Z. Y.; Yi, P.; Zou, H. H.; Deng, G.; Fang, M.; He, J. Z.; Sun, X.; Yu, R. H. et al. Inter-skeleton conductive routes tuning multifunctional conductive foam for electromagnetic interference shielding, sensing and thermal management. *Nano-Micro Lett.* **2025**, *17*, 52.

[5] Redlarski, G.; Lewczuk, B.; Żak, A.; Koncicki, A.; Krawczuk, M.; Piechocki, J.; Jakubiuk, K.; Tojza, P.; Jaworski, J.; Ambroziak, D. et al. The influence of electromagnetic pollution on living organisms: Historical trends and forecasting changes. *BioMed Res. Int.* **2015**, *2015*, 234098.

[6] Zhang, H. X.; Jia, Z. R.; Feng, A. L.; Zhou, Z. H.; Chen, L.; Zhang, C. H.; Liu, X. H.; Wu, G. L. *In situ* deposition of pitaya-like Fe_3O_4@C magnetic microspheres on reduced graphene oxide nanosheets for electromagnetic wave absorber. *Compos. Part B: Eng.* **2020**, *199*, 108261.

[7] Gao, Z. G.; Xu, B. H.; Ma, M. L.; Feng, A. L.; Zhang, Y.; Liu, X. H.; Jia, Z. R.; Wu, G. L. Electrostatic self-assembly synthesis of $ZnFe_2O_4$ quantum dots ($ZnFe_2O_4$@C) and electromagnetic microwave absorption. *Compos. Part B: Eng.* **2019**, *179*, 107417.

[8] Wang, Y.; Gao, X.; Lin, C. H.; Shi, L. Y.; Li, X. H.; Wu, G. L. Metal organic frameworks-derived Fe–Co nanoporous carbon/graphene composite as a high-performance electromagnetic wave absorber. *J. Alloys Compd.* **2019**, *785*, 765–773.

[9] Lv, Q. N.; Peng, Z. L.; Pei, H. R.; Zhang, X. X.; Chen, Y. H.; Zhang, H. R.; Zhu, X.; Wu, S. L. 3D printing of periodic porous metamaterials for tunable electromagnetic shielding across broad frequencies. *Nano-Micro Lett.* **2024**, *16*, 279.

[10] Qi, C. Z.; Min, P.; Zhou, X. F.; Jin, M.; Sun, X.; Wu, J. J.; Liu, Y. J.; Zhang, H. B.; Yu, Z. Z. Multifunctional asymmetric bilayer aerogels for highly efficient electromagnetic interference shielding with ultrahigh electromagnetic wave absorption. *Nano-Micro Lett.* **2025**, *17*, 291.

[11] Von Klemperer, C. J.; Maharaj, D. Composite electromagnetic interference shielding materials for aerospace applications. *Compos. Struct.* **2009**, *91*, 467–472.

[12] Cao, M. S.; Wang, X. X.; Zhang, M.; Shu, J. C.; Cao, W. Q.; Yang, H. J.; Fang, X. Y.; Yuan, J. Electromagnetic response and energy conversion for functions and devices in low-dimensional materials. *Adv. Funct. Mater.* **2019**, *29*, 1807398.

[13] Liu, T.; Feng, H. Y.; Jin, C. H.; Pawlak, M.; Saeb, M. R.; Kuang, T. R. Green segregated honeycomb biopolymer composites for electromagnetic interference shielding biomedical devices. *Chem. Eng. J.* **2024**, *493*, 152438.

[14] Shi, Y.; Wu, M. J.; Ge, S. B.; Li, J. Z.; Alshammari, A. S.; Luo, J.; Amin, M. A.; Qiu, H.; Jiang, J. X.; Asiri, Y. M. et al. Advanced functional electromagnetic shielding materials: A review based on micro-nano structure interface control of biomass cell walls. *Nano-Micro Lett.* **2025**, *17*, 3.

[15] Wang, J.; Wu, X. Y.; Wang, Y. J.; Zhao, W. Y.; Zhao, Y.; Zhou, M.; Wu, Y.; Ji, G. B. Green, sustainable architectural bamboo with high light transmission and excellent electromagnetic shielding as a candidate for energy-saving buildings. *Nano-Micro Lett.* **2023**, *15*, 11.

[16] Ma, Z. L.; Jiang, R. C.; Jing, J. Y.; Kang, S. L.; Ma, L.; Zhang, K. F.; Li, J. X.; Zhang, Y.; Qin, J. B.; Yun, S. H. et al. Lightweight dual-functional segregated nanocomposite foams for integrated infrared stealth and absorption-dominant electromagnetic interference shielding. *Nano-Micro Lett.* **2024**, *16*, 223.

[17] Nan, Z.; Wei, W.; Lin, Z. H.; Yuan, R. M.; Zhang, M.; Zhang, J. C.; Ouyang, J. Y.; Chang, J. J.; Li, H. J.; Hao, Y. Electromagnetic functions modulation of recycled by-products by heterodimensional structure. *Nano-Micro Lett.* **2025**, *17*, 137.

[18] Wang, L.; Ma, Z. L.; Qiu, H.; Zhang, Y. L.; Yu, Z.; Gu, J. W. Significantly enhanced electromagnetic interference shielding performances of epoxy nanocomposites with long-range aligned lamellar structures. *Nano-Micro Lett.* **2022**, *14*, 224.

[19] Wang, G. H.; Zhao, Y.; Yang, F.; Zhang, Y.; Zhou, M.; Ji, G. B. Multifunctional integrated transparent film for efficient electromagnetic protection. *Nano-Micro Lett.* **2022**, *14*, 65.

[20] Yu, X. C.; Guo, J.; Mao, Y. L.; Shan, C. W.; Tian, F. S.; Meng, B. H.; Wang, Z. J.; Zhang, T. Q.; Kyaw, A. K. K.; Chen, S. M. et al. Enhancing the performance of perovskite light-emitting diodes via synergistic effect of defect passivation and dielectric screening. *Nano-Micro Lett.* **2024**, *16*, 205.

[21] Peng, Y. D.; Dong, J. C.; Long, J. Y.; Zhang, Y. X.; Tang, X. W.; Lin, X.; Liu, H. R.; Liu, T. Q.; Fan, W.; Liu, T. X. et al. Thermally conductive and UV-EMI shielding electronic textiles for unrestricted

and multifaceted health monitoring. Nano-Micro Lett. **2024**, *16*, 199.
[22] Wang, T.; Kong, W. W.; Yu, W. C.; Gao, J. F.; Dai, K.; Yan, D. X.; Li, Z. M. A healable and mechanically enhanced composite with segregated conductive network structure for high-efficient electromagnetic interference shielding. Nano-Micro Lett. **2021**, *13*, 162.
[23] Xue, B.; Li, Y.; Cheng, Z. L.; Yang, S. D.; Xie, L.; Qin, S. H.; Zheng, Q. Directional electromagnetic interference shielding based on step-wise asymmetric conductive networks. Nano-Micro Lett. **2022**, *14*, 16.
[24] Liu, J.; Yu, M. Y.; Yu, Z. Z.; Nicolosi, V. Design and advanced manufacturing of electromagnetic interference shielding materials. Mater. Today **2023**, *66*, 245–272.
[25] Zhang, M.; Han, C.; Cao, W. Q.; Cao, M. S.; Yang, H. J.; Yuan, J. A nano-micro engineering nanofiber for electromagnetic absorber, green shielding and sensor. Nano-Micro Lett. **2021**, *13*, 27.
[26] Zhang, X. L.; Luo, W. L.; Chen, Y. Q.; Guo, Q. H.; Luo, J.; Burey, P.; Gao, Y. Y.; Lu, Y. L.; Gao, Q.; Li, J. C. et al. Highly thermal conductive and electromagnetic shielding polymer nanocomposites from waste masks. Nano-Micro Lett. **2025**, *17*, 263.
[27] Roh, W.; Seol, J. Y.; Park, J.; Lee, B.; Lee, J.; Kim, Y.; Cho, J.; Cheun, K.; Aryanfar, F. Millimeter-wave beamforming as an enabling technology for 5G cellular communications: Theoretical feasibility and prototype results. IEEE Commun. Mag. **2014**, *52*, 106–113.
[28] Esfahani, A. N.; Katbab, A.; Taeb, A.; Simon, L.; Pope, M. A. Correlation between mechanical dissipation and improved X-band electromagnetic shielding capabilities of amine functionalized graphene/thermoplastic polyurethane composites. Eur. Polym. J. **2017**, *95*, 520–538.
[29] Hu, Z. K.; Ji, X. X.; Li, B. Y.; Luo, Y. Z. A self-assembled graphene/polyurethane sponge for excellent electromagnetic interference shielding performance. RSC Adv. **2019**, *9*, 25829–25835.
[30] Nulli, S. A.; Ukhtary, M. S.; Saito, R. Significant enhancement of light absorption in undoped graphene using dielectric multilayer system. Appl. Phys. Lett. **2018**, *112*, 073101.
[31] Pu, J. H.; Zha, X. J.; Tang, L. S.; Bai, L.; Bao, R. Y.; Liu, Z. Y.; Yang, M. B.; Yang, W. Human skin-inspired electronic sensor skin with electromagnetic interference shielding for the sensation and protection of wearable electronics. ACS Appl. Mater. Interfaces **2018**, *10*, 40880–40889.
[32] Wen, J.; Wu, Y. C.; Gao, Y. X.; Su, Q.; Liu, Y. T.; Wu, H. D.; Zhang, H. C.; Liu, Z. Q.; Yao, H.; Huang, X. W. et al. Nanofiber composite reinforced organohydrogels for multifunctional and wearable electronics. Nano-Micro Lett. **2023**, *15*, 174.
[33] Gao, H.; Wang, C. H.; Yang, Z. J.; Zhang, Y. 3D porous nickel metal foam/polyaniline heterostructure with excellent electromagnetic interference shielding capability and superior absorption based on pre-constructed macroscopic conductive framework. Compos. Sci. Technol. **2021**, *213*, 108896.
[34] Xu, Y. D.; Lin, Z. Q.; Rajavel, K.; Zhao, T.; Zhu, P. L.; Hu, Y. G.; Sun, R.; Wong, C. P. Tailorable, lightweight and superelastic liquid metal monoliths for multifunctional electromagnetic interference shielding. Nano-Micro Lett. **2022**, *14*, 29.
[35] Ding, H.; Zang, W. P.; Yu, M.; Wang, Y. H.; Jiang, Y. J.; Ning, N. Y.; Yu, B.; Tian, M. Large-scale ultralight and flexible metal foil/polymer sandwich composites with excellent electromagnetic interference shielding. Adv. Mater. Technol. **2023**, *8*, 2300393.
[36] Ji, H.; Zhao, R.; Zhang, N.; Jin, C. X.; Lu, X. F.; Wang, C. Lightweight and flexible electrospun polymer nanofiber/metal nanoparticle hybrid membrane for high-performance electromagnetic interference shielding. NPG Asia Mater. **2018**, *10*, 749–760.
[37] Yang, M.; Jia, X. T.; He, D. Y.; Ma, Y. Y.; Cheng, Y.; Wang, J.; Li, Y. X.; Wang, C. Superhydrophobic and corrosion-resistant electrospun hybrid membrane for high-efficiency electromagnetic interference shielding. ACS Appl. Electron. Mater. **2021**, *3*, 2067–2078.
[38] Tiwari, A.; Tiwari, A.; Bhatia, A.; Chadha, U.; Kandregula, S.; Selvaraj, S. K.; Bhardwaj, P. Nanomaterials for electromagnetic interference shielding applications: A review. Nano **2022**, *17*, 2230001.
[39] Ghosh, S.; Ganguly, S.; Remanan, S.; Das, N. C. Fabrication and investigation of 3D tuned PEG/PEDOT: PSS treated conductive and durable cotton fabric for superior electrical conductivity and flexible electromagnetic interference shielding. Compos. Sci. Technol. **2019**, *181*, 107682.
[40] Gai, L. X.; Guo, L.; An, Q. D.; Xiao, Z. Y.; Zhai, S. R.; Li, Z. C. Facile fabrication of SBA-15/polypyrrole composites with long-rod shape for enhanced electromagnetic wave absorption. Micropor. Mesopor. Mater. **2019**, *288*, 109584.
[41] Deng, R. X.; Chen, B. B.; Li, H. G.; Zhang, K.; Zhang, T.; Yu, Y.; Song, L. X. MXene/Co_3O_4 composite material: Stable synthesis and its enhanced broadband microwave absorption. Appl. Surf. Sci. **2019**, *488*, 921–930.
[42] Gupta, S.; Sharma, S. K.; Pradhan, D.; Tai, N. H. Ultra-light 3D reduced graphene oxide aerogels decorated with cobalt ferrite and zinc oxide perform excellent electromagnetic interference shielding effectiveness. Compos. Part A: Appl. Sci. Manuf. **2019**, *123*, 232–241.
[43] Liu, P. J.; Yao, Z. J.; Ng, V. M. H.; Zhou, J. T.; Kong, L. B. Novel multilayer-like structure of $Ti_3C_2T_x$/CNZF composites for low-frequency electromagnetic absorption. Mater. Lett. **2019**, *248*, 214–217.
[44] An, J.; Fei, G. Q.; Chen, H. J.; Zhang, B. Y.; Bai, Y. Flexible multifunctional Janus film towards self-healing, self-adhesive and streachable EMI shielding. J. Colloid Interface Sci. **2025**, *685*, 1056–1067.
[45] Shen, M. X.; Li, X. J.; Qi, J. L.; Sun, J. J.; Cao, W. S.; Xiu, H. J.; Li, J. B.; Zhang, Z. L.; Zheng, X. F.; Shang, Z. Magnetic metal-loaded wood carbon aerogel composites for electromagnetic shielding and microwave absorption. Compos. Part A: Appl. Sci. Manuf. **2025**, *198*, 109070.
[46] Zhou, Z. X. Y.; Huang, Y. Q.; Shen, Q.; Li, Y. Y.; Cheng, X. M. Composite phase change materials with carbon-mesh/CuS/ZnO interface biocarbon skeleton for solar energy storage, solar photocatalysis and electromagnetic shielding. J. Energy Storage **2024**, *90*, 111937.
[47] Chen, M. Y.; Zhu, J.; Zhang, K.; Zhou, H. K.; Gao, Y. F.; Fan, J.; Chen, R. X.; Wang, H. L. Carbon nanofiber/polyaniline composite aerogel with excellent electromagnetic interference shielding, low thermal conductivity, and extremely low heat release. Nano-Micro Lett. **2025**, *17*, 80.
[48] Sharma, G. K.; Harel, P. G.; James, N. R. Flexible N-doped carbon nanofiber containing Nb_2O_5 nanoparticle and its polydimethylsiloxane composite for electromagnetic interference shielding. Carbon **2023**, *214*, 118367.
[49] Zhang, Z. H.; Cheng, L. S.; Sheng, T. Y.; Yu, J. C.; Tan, J.; Yang, W. M. SiC nanofiber-coated carbon/carbon composite for electromagnetic interference shielding. ACS Appl. Nano Mater. **2022**, *5*, 195–204.
[50] Sun, H. B.; Shi, G. Y.; Kang, Z. L.; Zhong, H. Y.; Han, W. J.; Luo, Z. H.; Zhang, B. X. Thin and flexible multilayer carbon/silicon carbide composite films with extraordinary electromagnetic shielding performance and ablative resistance. Carbon **2024**, *230*, 119660.
[51] Liu, H. M.; Zhang, X.; Li, K. Z.; Cui, Q. A.; Shen, Q. L.; Li, H. J.; Yin, X. M. Functional integrated electromagnetic interference shielding in supercapacitors based on aligned SiC nanowires decorated vertical graphene nanosheets. Carbon **2024**, *220*, 118864.
[52] Tohidifar, M. R. Highly-efficient electromagnetic interference shielding and microwave dielectric behavior of a (Bi_2O_3 + B_2O_3)-doped MWCNT/$BaTiO_3$ ceramic nanocomposite. Ceram. Int. **2018**,

44, 13613–13622.

[53] Zhou, J. Q.; Yuan, X. M.; Sun, N.; Yan, S. H.; Zhang, X. M.; Wang, B. M.; Zhu, B.; Cai, X.; Qiao, K. MoS_2 nanosheet/CF network: Realizing high-efficiency electromagnetic protection and enhanced thermal conductivity via structure-function integration. *Compos. Part A: Appl. Sci. Manuf.* **2025**, *192*, 108790.

[54] Rezaei, H.; Soltani-Mohammadi, F.; Dogari, H.; Ghafuri, H.; Peymanfar, R. Plasma-assisted doping of pyrolyzed corn husk strengthened by MoS_2/polyethersulfone for fascinating microwave absorbing/shielding and energy saving properties. *Nanoscale* **2024**, *16*, 18962–18975.

[55] Deng, F. K.; Wei, J. H.; Xu, Y. D.; Lin, Z. Q.; Lu, X.; Wan, Y. J.; Sun, R.; Wong, C. P.; Hu, Y. G. Regulating the electrical and mechanical properties of TaS_2 films via van der Waals and electrostatic interaction for high performance electromagnetic interference shielding. *Nano-Micro Lett.* **2023**, *15*, 106.

[56] Kang, B. H.; Lee, D. K.; Kim, D. S.; Hur, O. N.; Lee, C. S.; Bae, J.; Park, S. H. High-yield exfoliation of $NbSe_2$ through optimized lithium-ion intercalation and its application in electromagnetic-interference shielding. *Appl. Surf. Sci.* **2023**, *637*, 157954.

[57] Zhang, H. B.; Liu, T. T.; Huang, Z. H.; Cheng, J. Y.; Wang, H. H.; Zhang, D. Q.; Ba, X. W.; Zheng, G. P.; Yan, M.; Cao, M. S. Engineering flexible and green electromagnetic interference shielding materials with high performance through modulating WS_2 nanosheets on carbon fibers. *J. Materiomics* **2022**, *8*, 327–334.

[58] Ai, R. Q.; Cui, X. M.; Li, Y.; Zhuo, X. L. Local strain engineering of two-dimensional transition metal dichalcogenides towards quantum emitters. *Nano-Micro Lett.* **2025**, *17*, 104.

[59] Han, J. H.; Park, J.; Kim, M.; Lee, S.; Heo, J. M.; Jin, Y. H.; Chae, Y.; Han, J.; Wang, J.; Seok, S. H. et al. Ultrahigh conductive MXene films for broadband electromagnetic interference shielding. *Adv. Mater.* **2025**, *37*, 2502443.

[60] Wang, Y. J.; Zhao, C. X.; Tian, Y. Z.; Sun, Y.; Zhang, M. F.; Wang, K. J.; Xia, B. H.; Wang, Y.; Li, T.; Zhang, X. H. et al. Lightweight MXene composite films with hollow egg-box structures: Enhanced electromagnetic shielding performance beyond pure MXene. *Adv. Sci.* **2025**, *12*, 2411932.

[61] Feng, W. D.; Zou, L. H.; Lan, C. T.; E, S. J.; Pu, X. Core-sheath CNT@MXene fibers toward absorption-dominated electromagnetic interference shielding fabrics. *Adv. Fiber Mater.* **2024**, *6*, 1657–1668.

[62] Hassan, T.; Iqbal, A.; Yoo, B.; Jo, J. Y.; Cakmakci, N.; Naqvi, S. M.; Kim, H.; Jung, S.; Hussain, N.; Zafar, U. et al. Multifunctional MXene/carbon nanotube Janus film for electromagnetic shielding and infrared shielding/detection in harsh environments. *Nano-Micro Lett.* **2024**, *16*, 216.

[63] Ghaffarkhah, A.; Hashemi, S. A.; Rostami, S.; Amini, M.; Ahmadijokani, F.; Isfahani, A. P.; Mhatre, S. E.; Rojas, O. J.; Kamkar, M.; Wuttke, S. et al. Ultra-flyweight cryogels of MXene/graphene oxide for electromagnetic interference shielding. *Adv. Funct. Mater.* **2023**, *33*, 2304748.

[64] Huang, P. F.; Han, W. Q. Recent advances and perspectives of Lewis acidic etching route: An emerging preparation strategy for MXenes. *Nano-Micro Lett.* **2023**, *15*, 68.

[65] Jin, L. Y.; Cao, W. J.; Wang, P.; Song, N.; Ding, P. Interconnected MXene/graphene network constructed by soft template for multi-performance improvement of polymer composites. *Nano-Micro Lett.* **2022**, *14*, 133.

[66] Dastgeer, G.; Zulfiqar, M. W.; Nisar, S.; Zulfiqar, R.; Imran, M.; Panchanan, S.; Dutta, S.; Akbar, K.; Vomiero, A.; Wang, Z. M. Emerging role of 2D materials in photovoltaics: Efficiency enhancement and future perspectives. *Nano-Micro Lett.* **2026**, *18*, 32.

[67] Sun, Y. Z.; He, W. Y.; Jiang, C.; Li, J.; Liu, J. L.; Liu, M. J. Wearable biodevices based on two-dimensional materials: From flexible sensors to smart integrated systems. *Nano-Micro Lett.* **2025**, *17*, 109.

[68] Yu, K. L.; Pan, Y. L.; Zhang, Z. L.; Xiang, H. Y.; Zeng, H. B.; Chen, Z. S. Recent progress in low-dimensional transition metal dichalcogenides materials for electromagnetic wave absorption. *Chem. Eng. J.* **2025**, *512*, 162622.

[69] Xia, Y. X.; Gao, W. W.; Gao, C. A review on graphene-based electromagnetic functional materials: Electromagnetic wave shielding and absorption. *Adv. Funct. Mater.* **2022**, *32*, 2204591.

[70] Yang, Y. C.; Liu, Z.; Wang, Y. J.; Zhang, Z. H.; Wang, X. C. Research progress of two-dimensional materials in the field of electromagnetic shielding. *Mater. Today Phys.* **2025**, *50*, 101617.

[71] Liu, J. K.; Jia, Z. R.; Zhou, W. H.; Liu, X. H.; Zhang, C. H.; Xu, B. H.; Wu, G. L. Self-assembled MoS_2/magnetic ferrite $CuFe_2O_4$ nanocomposite for high-efficiency microwave absorption. *Chem. Eng. J.* **2021**, *429*, 132253.

[72] Zhang, H. B.; Cheng, J. Y.; Wang, H. H.; Huang, Z. H.; Zheng, Q. B.; Zheng, G. P.; Zhang, D. Q.; Che, R. C.; Cao, M. S. Initiating VB-group laminated NbS_2 electromagnetic wave absorber toward superior absorption bandwidth as large as 6.48GHz through phase engineering modulation. *Adv. Funct. Mater.* **2021**, *32*, 2108194.

[73] Zhang, S. J.; Li, J. Y.; Jin, X. T.; Wu, G. L. Current advances of transition metal dichalcogenides in electromagnetic wave absorption: A brief review. *Int. J. Miner. Metall. Mater.* **2023**, *30*, 428–445.

[74] Jiang, Q. L.; Xu, L.; Tang, Z. M.; Xie, C.; Lu, J. Y.; Han, Z. H.; Zhang, D.; Zuo, C. H. A competitive strategy toward 1T/2H MoS_2 to balance impedance for optimizing electromagnetic wave absorption. *Chem. Eng. J.* **2024**, *491*, 151854.

[75] Song, K. R.; Shui, A. Z.; Hu, M. Y.; Yu, H. L. Integration of phase engineering and defect engineering on O-doped 1T/2H MoS_2 for boosting electromagnetic wave absorption. *J. Alloys Compd.,* **2025**, *1039*, 183164.

[76] Navik, R.; Tan, H. J.; Zhang, H.; Shi, L. Y.; Li, J.; Zhao, Y. P. High-throughput and scalable exfoliation of large-sized ultrathin 2D materials by ball-milling in supercritical carbon dioxide. *Small Methods* **2024**, *8*, 2301334.

[77] Zu, C. Z.; Rong, H. W.; Zhao, R. Z.; Liu, Y.; Zhang, J.; Zhang, X. F. Flexible, hydrophobic MoS_2 nanosheets decorated carbon cloth composites for efficient electromagnetic interference shielding. *Mater. Res. Bull.* **2025**, *190*, 113533.

[78] Li, Y.; Cao, J. Y.; Chen, G. L.; He, L. J.; Du, X. C.; Xie, J. Y.; Wang, Y. M.; Hu, W. B. Scalable production of highly conductive 2D $NbSe_2$ monolayers with superior electromagnetic interference shielding performance. *ACS Appl. Mater. Interfaces* **2024**, *16*, 6250–6260.

[79] Ali, M. S.; Ali, M. S.; Bhandari, S.; Saini, S.; Karmakar, S.; Chattopadhyay, D. Recent progress on MXene-polymer nanocomposites and their applications. *Sustain. Mater. Technol.* **2025**, *45*, e01563.

[80] Deng, Y. L.; Chen, Y. Q.; Liu, W.; Wu, L. L.; Wang, Z.; Xiao, D.; Meng, D. C.; Jiang, X. G.; Liu, J. R.; Zeng, Z. H. et al. Transparent electromagnetic interference shielding materials using MXene. *Carbon Energy* **2024**, *6*, e593.

[81] Zhao, X. X.; Huang, Y.; Liu, X. D.; Jiang, H. Y.; Yu, M.; Ma, X. F.; Zong, M.; Liu, P. B. Hollow multi-layer bowknot like nanoparticles surface modified by TMDs derived flexible fiber membranes for electromagnetic wave absorption. *Chem. Eng. J.* **2024**, *483*, 149085.

[82] Yan, Y. F.; Zhang, K. L.; Qin, G. Y.; Gao, B. S.; Zhang, T.; Huang, X. X.; Zhou, Y. Phase engineering on MoS_2 to realize dielectric gene engineering for enhancing microwave absorbing performance. *Adv. Funct. Mater.* **2024**, *34*, 2316338.

[83] Long, L. N.; Bich, T. T. N. Hydrothermal phase engineering of 1T/2H MoS_2/graphene nanocomposites for enhanced electronic, catalytic, and electrochemical performance. *Adv. Mater. Technol.* **2025**, *10*, e00454.

[84] Qin, J. L.; Pei, F.; Wang, R.; Wu, L.; Han, Y.; Xiao, P.; Shen, Y.; Yuan, L. X.; Huang, Y. H.; Wang, D. L. Sulfur vacancies and 1T phase-rich MoS_2 nanosheets as an artificial solid electrolyte

interphase for 400 Wh·kg−1 lithium metal batteries. *Adv. Mater.* **2024**, *36*, 2312773.

[85] Hemanth, N. R.; Kim, T.; Kim, B.; Jadhav, A. H.; Lee, K.; Chaudhari, N. K. Transition metal dichalcogenide-decorated MXenes: Promising hybrid electrodes for energy storage and conversion applications. *Mater. Chem. Front.* **2021**, *5*, 3298–3321.

[86] Kumari, S.; Dalal, J.; Kumar, V.; Kumar, A.; Ohlan, A. Emerging two-dimensional materials for electromagnetic interference shielding application. *Int. J. Mol. Sci.* **2023**, *24*, 12267.

[87] Zhang, D. Q.; Liu, T. T.; Shu, J. C.; Liang, S.; Wang, X. X.; Cheng, J. Y.; Wang, H.; Cao, M. S. Self-assembly construction of WS_2–rGO architecture with green EMI shielding. *ACS Appl. Mater. Interfaces* **2019**, *11*, 26807–26816.

[88] Uddin, A.; Khatoon, R.; Estevez, D.; Salem, M.; Ali, A.; Attique, S.; Lu, J.; Qin, F. X. Waste paper cellulose based-MoS_2 hybrid composites: Towards sustainable green shielding. *Mater. Today Commun.* **2022**, *31*, 103858.

[89] Wang, L.; Cheng, J. W.; Zou, Y. X.; Zheng, W. Y.; Wang, Y. R.; Liu, Y. Q.; Zhang, H. R.; Zhang, D.; Ji, X. H. Current advances and future perspectives of MXene-based electromagnetic interference shielding materials. *Adv. Compos. Hybrid Mater.* **2023**, *6*, 172.

[90] Omana, L.; Chandran, A.; John, R. E.; Wilson, R.; George, K. C.; Unnikrishnan, N. V.; Varghese, S. S.; George, G.; Simon, S. M.; Paul, I. Recent advances in polymer nanocomposites for electromagnetic interference shielding: A review. *ACS Omega* **2022**, *7*, 25921–25947.

[91] Zou, L. H.; Lan, C. T.; Zhang, S. L.; Zheng, X. H.; Xu, Z. Z.; Li, C. L.; Yang, L.; Ruan, F. T.; Tan, S. C. Near-instantaneously self-healing coating toward stable and durable electromagnetic interference shielding. *Nano-Micro Lett.* **2021**, *13*, 190.

[92] Abbasi, H.; Antunes, M.; Velasco, J. I. Recent advances in carbon-based polymer nanocomposites for electromagnetic interference shielding. *Prog. Mater. Sci.* **2019**, *103*, 319–373.

[93] Oliveira, F. M.; Gusmão, R. Recent advances in the electromagnetic interference shielding of 2D materials beyond graphene. *ACS Appl. Electron. Mater.* **2020**, *2*, 3048–3071.

[94] Shahzad, F.; Alhabeb, M.; Hatter, C. B.; Anasori, B.; Man Hong, S.; Koo, C. M.; Gogotsi, Y. Electromagnetic interference shielding with 2D transition metal carbides (MXenes). *Science* **2016**, *353*, 1137–1140.

[95] Simon, R. M. EMI shielding through conductive plastics. *Polym.-Plast. Technol. Eng.* **1981**, *17*, 1–10.

[96] Das, N. C.; Liu, Y. Y.; Yang, K. K.; Peng, W. Q.; Maiti, S.; Wang, H. Single-walled carbon nanotube/poly(methyl methacrylate) composites for electromagnetic interference shielding. *Polym. Eng. Sci.* **2009**, *49*, 1627–1634.

[97] Farukh, M.; Dalal, J.; Ohlan, A.; Dhawan, S. K. Synthesis of poly (3, 4-ethylene dioxythiophene) conducting polymer composites for EMI shielding applications. In *Smart Materials Design for Electromagnetic Interference Shielding Applications*. Dhawan, S. K.; Singh, A. P.; Ohlan, A.; Kakran, K. S.; Sambyal, P., Eds.; Bentham Science Publishers: Québec, 2022; pp 213–270.

[98] Dhanasekaran, A.; Dhanaraj, K.; Venugopal, V. 2D transition metal dichalcogenides-based composites for electromagnetic interference shielding and microwave absorption applications. *Phys. Status Solidi (A) Appl. Mater. Sci.* **2024**, *221*, 2300903.

[99] Santos, K. M. G.; Novo, M. S.; Fontgalland, G.; Perotoni, M. B.; Andrade, C. L. Shielding effectiveness measurements of coaxial cable and connectors using compact open area test site. *J. Microw. Optoelectron. Electromagn. Appl.* **2017**, *16*, 997–1011.

[100] Cirielli, D. Microwave shielding effectiveness study of composites materials and coating based ongraphene, MWCNT and Biochar. Master Degree Thesis, Politecnico di Torino, Torino, Italy, 2019.

[101] Šafářová, V.; Tunák, M.; Truhlář, M.; Militký, J. A new method and apparatus for evaluating the electromagnetic shielding effectiveness of textiles. *Text. Res. J.* **2016**, *86*, 44–56.

[102] Mathur, P.; Raman, S. Electromagnetic interference (EMI): Measurement and reduction techniques. *J. Electron. Mater.* **2020**, *49*, 2975–2998.

[103] Zhao, J. Y.; Zhang, D.; Sun, J. J.; Zhang, H. F. Dynamic field nulling method for magnetically shielded room based on Smith predictor assisted GADRC. *Sens. Actuat. A: Phys.* **2025**, *387*, 116394.

[104] Jin, Q.; Sheng, W. X.; Gao, C.; Han, Y. B. Internal and external transmission line transfer matrix and near-field radiation of braided coaxial cables. *IEEE Trans. Electromagn. C.* **2021**, *63*, 206–214.

[105] Hong, J.; Xu, P.; Xia, H.; Xu, Z. Z.; Ni, Q. Q. Electromagnetic interference shielding anisotropy enhanced by CFRP laminated structures. *Compos. Sci. Technol.* **2021**, *203*, 108616.

[106] Domae, A.; Horibe, M. Development of inductance reference standard using coaxial transmission lines. *IEEJ Trans. Electr. Electron. Eng.* **2020**, *15*, 496–500.

[107] Jha, B. K.; Yoon, J. C.; Jang, J. H. 3D graphene for energy technologies: Chemical strategies and industrial challenges. *Acc. Mater. Res.* **2025**, *6*, 799–813.

[108] Chhowalla, M.; Shin, H. S.; Eda, G.; Li, L. J.; Loh, K. P.; Zhang, H. The chemistry of two-dimensional layered transition metal dichalcogenide nanosheets. *Nat. Chem.* **2013**, *5*, 263–275.

[109] Liu, F.; Wu, W. J.; Bai, Y. S.; Chae, S. H.; Li, Q. Y.; Wang, J.; Hone, J.; Zhu, X. Y. Disassembling 2D van der Waals crystals into macroscopic monolayers and reassembling into artificial lattices. *Science* **2020**, *367*, 903–906.

[110] Liu, Z. H.; Chen, X. Y.; Zhao, Y.; Pang, Y. T.; Wei, D. G.; Wangchen, J. Y.; Yao, C. B. Constructing MO/TMDs heterostructures: Photoelectrochemical activity and charge transfer mechanism investigation. *Chem. Eng. J.* **2025**, *511*, 161981.

[111] Zhai, D. W.; Yu, H. Y.; Yao, W. Twistronics and moiré superlattice physics in 2D transition metal dichalcogenides. *Rep. Prog. Phys.* **2025**, *88*, 084501.

[112] Kumar, B. A.; Elangovan, T.; Raju, K.; Ramalingam, G.; Sambasivam, S.; Alam, M. M. Green solvent exfoliation of few layers 2D-MoS_2 nanosheets for efficient energy harvesting and storage application. *J. Energy Storage* **2023**, *65*, 107336.

[113] Nakata, Y.; Sugawara, K.; Chainani, A.; Oka, H.; Bao, C. H.; Zhou, S. H.; Chuang, P. Y.; Cheng, C. M.; Kawakami, T.; Saruta, Y. et al. Robust charge-density wave strengthened by electron correlations in monolayer 1T–$TaSe_2$ and 1T–$NbSe_2$. *Nat. Commun.* **2021**, *12*, 5873.

[114] Zeng, H. L.; Dai, J. F.; Yao, W.; Xiao, D.; Cui, X. D. Valley polarization in MoS_2 monolayers by optical pumping. *Nat. Nanotechnol.* **2012**, *7*, 490–493.

[115] Ren, T. T.; Tian, W. R.; Shen, Q.; Yuan, Z. T.; Chen, D. Y.; Li, N. J.; Lu, J. M. Enhanced piezocatalysis of polymorphic few-layered MoS_2 nanosheets by phase engineering. *Nano Energy* **2021**, *90*, 106527.

[116] Wang, J. E.; Ming, W.; Chen, L. F.; Song, T. L.; Yele, M. X.; Zhang, H.; Yang, L.; Sarula, G.; Liang, B. L.; Yan, L. T. et al. MoS_2 lubricate-toughened MXene/ANF composites for multifunctional electromagnetic interference shielding. *Nano-Micro Lett.* **2025**, *17*, 36.

[117] Azam, A.; Yang, J.; Li, W. X.; Huang, J. K.; Li, S. A. Tungsten diselenides (WSe_2) quantum dots: Fundamental, properties, synthesis and applications. *Prog. Mater. Sci.* **2023**, *132*, 101042.

[118] Pan, J.; Guo, C. G.; Song, C. S.; Lai, X. F.; Li, H.; Zhao, W.; Zhang, H.; Mu, G.; Bu, K. J.; Lin, T. Q. et al. Enhanced superconductivity in restacked TaS_2 nanosheets. *J. Am. Chem. Soc.* **2017**, *139*, 4623–4626.

[119] Li, L. J.; Deng, X. Y.; Wang, Z.; Liu, Y.; Abeykoon, M.; Dooryhee, E.; Tomic, A.; Huang, Y. N.; Warren, J. B.; Bozin, E. S. et al. Superconducting order from disorder in 2H–$TaSe_{2-x}S_x$. *npj Quantum Mater.* **2017**, *2*, 11.

[120] Zong, P. A.; Yoo, D.; Zhang, P.; Wang, Y. F.; Huang, Y. J.; Yin, S. J.; Liang, J.; Wang, Y. L.; Koumoto, K.; Wan, C. L. Flexible foil of

hybrid TaS_2/organic superlattice: Fabrication and electrical properties. *Small* **2020**, *16*, 1901901.
[121] Kovalska, E.; Roy, P. K.; Antonatos, N.; Mazanek, V.; Vesely, M.; Wu, B.; Sofer, Z. Photocatalytic activity of twist-angle stacked 2D TaS_2. *npj 2D Mater. Appl.* **2021**, *5*, 68.
[122] Ganal, P.; Olberding, W.; Butz, T.; Ouvrard, G. Soft chemistry induced host metal coordination change from octahedral to trigonal prismatic in 1T–TaS_2. *Solid State Ionics* **1993**, *59*, 313–319.
[123] Zhang, L. Z.; Chen, C.; Zhou, J. D.; Yang, G. L.; Wang, J. M.; Liu, D.; Chen, Z. Q.; Lei, W. W. Solid phase exfoliation for producing dispersible transition metal dichalcogenides nanosheets. *Adv. Funct. Mater.* **2020**, *30*, 2004139.
[124] Ao, Y.; Jin, L.; Wang, S. L.; Lan, B. L.; Tian, G.; Xu, T. P.; Huang, L. C.; Wang, Z. H.; Sun, Y.; Yang, T. et al. Dual structure reinforces interfacial polarized MXene/PVDF–TrFE piezoelectric nanocomposite for pressure monitoring. *Nano-Micro Lett.* **2025**, *17*, 320.
[125] Cao, W. T.; Ma, C.; Tan, S.; Ma, M. G.; Wan, P. B.; Chen, F. Ultrathin and flexible CNTs/MXene/cellulose nanofibrils composite paper for electromagnetic interference shielding. *Nano-Micro Lett.* **2019**, *11*, 72.
[126] Guo, J. L.; Zhang, T. Y.; Hao, X. Y.; Liu, S. J.; Zou, Y. X.; Li, J. J.; Wu, W.; Chen, L. M.; Liu, X. Q. Aramid nanofiber/MXene-reinforced polyelectrolyte hydrogels for absorption-dominated electromagnetic interference shielding and wearable sensing. *Nano-Micro Lett.* **2025**, *17*, 271.
[127] Han, Z. Y.; Niu, Y. T.; Shi, X. T.; Pan, D.; Liu, H.; Qiu, H.; Chen, W. H.; Xu, B. B.; El-Bahy, Z. M.; Hou, H. et al. MXene@c-MWCNT adhesive silica nanofiber membranes enhancing electromagnetic interference shielding and thermal insulation performance in extreme environments. *Nano-Micro Lett.* **2024**, *16*, 195.
[128] Khan, R.; Khan, Z. M.; Aqeel, H. B.; Javed, S.; Shafqat, A.; Qazi, I.; Basit, M. A.; Jan, R. 2D nanosheets and composites for EMI shielding analysis. *Sci. Rep*. **2020**, *10*, 21550.
[129] Zhang, D. Q.; Liang, S.; Chai, J. X.; Liu, T. T.; Yang, X. Y.; Wang, H.; Cheng, J. Y.; Zheng, G. P.; Cao, M. S. Highly effective shielding of electromagnetic waves in MoS_2 nanosheets synthesized by a hydrothermal method. *J. Phys. Chem. Solids* **2019**, *134*, 77–82.
[130] Anwar, U.; Alburaih, H. A.; Abid, A. Y.; Noor, N. A.; Mumtaz, S. Structural and functional analysis of MoS_2 nanoparticles: A multi-temperature approach to impedance and X-band shielding applications. *Mater. Today Commun.* **2025**, *47*, 113188.
[131] Luxa, J.; Oliveira, F. M.; Jellet, C. W.; Gusmão, R.; Sofer, Z. Freestanding foils of $NbSe_2$ and carbon nanotubes for efficient electromagnetic shielding. *ACS Appl. Nano Mater.* **2023**, *6*, 3333–3343.
[132] Kumar, P.; Shahzad, F.; Yu, S.; Hong, S. M.; Kim, Y. H.; Koo, C. M. Large-area reduced graphene oxide thin film with excellent thermal conductivity and electromagnetic interference shielding effectiveness. *Carbon* **2015**, *94*, 494–500.
[133] Wei, Q. W.; Pei, S. F.; Qian, X. T.; Liu, H. P.; Liu, Z. B.; Zhang, W. M.; Zhou, T. Y.; Zhang, Z. C.; Zhang, X. F.; Cheng, H. M. et al. Superhigh electromagnetic interference shielding of ultrathin aligned pristine graphene nanosheets film. *Adv. Mater.* **2020**, *32*, 1907411.
[134] Zhu, E. H.; Pang, K.; Chen, Y. R.; Liu, S. P.; Liu, X. T.; Xu, Z.; Liu, Y. J.; Gao, C. Ultra-stable graphene aerogels for electromagnetic interference shielding. *Sci. China Mater.* **2023**, *66*, 1106–1113.
[135] Chen, Y.; Li, J. Z.; Li, T.; Zhang, L. K.; Meng, F. B. Recent advances in graphene-based films for electromagnetic interference shielding: Review and future prospects. *Carbon* **2021**, *180*, 163–184.
[136] Tang, H. J.; Wang, J. Y.; Yin, H. J.; Zhao, H. J.; Wang, D.; Tang, Z. Y. Growth of polypyrrole ultrathin films on MoS_2 monolayers as high-performance supercapacitor electrodes. *Adv. Mater.* **2015**, *27*, 1117–1123.
[137] Liu, J. L.; Liang, H. S.; Wu, H. J. Hierarchical flower-like Fe_3O_4/MoS_2 composites for selective broadband electromagnetic wave absorption performance. *Compos. Part A: Appl. Sci. Manuf.* **2020**, *130*, 105760.
[138] Han, M. K.; Shuck, C. E.; Rakhmanov, R.; Parchment, D.; Anasori, B.; Koo, C. M.; Friedman, G.; Gogotsi, Y. Beyond $Ti_3C_2T_x$: MXenes for electromagnetic interference shielding. *ACS Nano* **2020**, *14*, 5008–5016.
[139] Verma, R.; Thakur, P.; Chauhan, A.; Jasrotia, R.; Thakur, A. A review on MXene and its' composites for electromagnetic interference (EMI) shielding applications. *Carbon* **2023**, *208*, 170–190.
[140] Dhanasekaran, A.; Lakshmanan, A.; Malakar, A.; Bose, S.; Dhanaraj, K.; Venugopal, V. Polyaniline/$BaTiO_3$/MoS_2 Hybrid Nanocomposites for High-Frequency EMI Shielding Applications. *ACS Appl. Nano Mater.* **2025**, *8*, 17561–17566.
[141] Kumari, C.; Sharma, D.; Kakkar, A.; Jangid, N. K. Applications of 2D materials in electromagnetic interference shielding. In *2D Materials: Fundamentals, Fabrication, and Applications*. Sharma, R.; Raghav, S., Eds.; Springer: Singapore, 2025; pp 161–180.
[142] Ma, Z. K.; He, J. Z.; Liu, S. L.; Zhang, W. T.; Gan, M. H.; Wu, Q. L.; Xing, M. Adjustable humidity response: Ultrahigh green EMI shielding gel with double-side constant temperature capability. *Adv. Funct. Mater.* **2025**, *35*, 2414942.
[143] Liu, J.; Zhang, H. B.; Sun, R. H.; Liu, Y. F.; Liu, Z. S.; Zhou, A. G.; Yu, Z. Z. Hydrophobic, flexible, and lightweight MXene foams for high-performance electromagnetic-interference shielding. *Adv. Mater.* **2017**, *29*, 1702367.
[144] Liu, Y.; Wang, Y. D.; Wu, N.; Han, M. R.; Liu, W.; Liu, J. R.; Zeng, Z. H. Diverse structural design strategies of MXene-based macrostructure for high-performance electromagnetic interference shielding. *Nano-Micro Lett.* **2023**, *15*, 240.
[145] Yost, D. C.; Friedman, A. L.; Hanbicki, A. T.; Grossman, J. C. 2D monolayers for superior transparent electromagnetic interference shielding. *ACS Nano* **2022**, *16*, 9498–9509.
[146] Zhang, J.; Zhang, J. C.; Shuai, X. F.; Zhao, R. H.; Guo, T. Y.; Li, K. X.; Wang, D. H.; Ma, C.; Li, J. P.; Du, J. P. Design and synthesis strategies: 2D materials for electromagnetic shielding/absorbing. *Chem. Asian J.* **2021**, *16*, 3817–3832.
[147] Bian, R. J.; He, G. L.; Zhi, W. Q.; Xiang, S. L.; Wang, T. W.; Cai, D. Y. Ultralight MXene-based aerogels with high electromagnetic interference shielding performance. *J. Mater. Chem. C* **2019**, *7*, 474–478.
[148] Iqbal, A.; Shahzad, F.; Hantanasirisakul, K.; Kim, M. K.; Kwon, J.; Hong, J.; Kim, H.; Kim, D.; Gogotsi, Y.; Koo, C. M. Anomalous absorption of electromagnetic waves by 2D transition metal carbonitride Ti_3CNT_x(MXene). *Science* **2020**, *369*, 446–450.
[149] Huang, W. Q.; Liu, X. B.; Wang, Y. F.; Feng, J. Y.; Huang, J. H.; Dai, Z. X.; Yang, S. D.; Pei, S. F.; Zhong, J.; Gui, X. C. Ultra- broadband and ultra-high electromagnetic interference shielding performance of aligned and compact MXene films. *Nano-Micro Lett.* **2025**, *17*, 234.
[150] Li, Y. H.; Chen, Y. A.; He, X. F.; Xiang, Z. Y.; Heinze, T.; Qi, H. S. Lignocellulose nanofibril/gelatin/MXene composite aerogel with fire-warning properties for enhanced electromagnetic interference shielding performance. *Chem. Eng. J.* **2022**, *431*, 133907.
[151] Liu, L. X.; Chen, W.; Zhang, H. B.; Ye, L. X.; Wang, Z. G.; Zhang, Y.; Min, P.; Yu, Z. Z. Super-tough and environmentally stable aramid. Nanofiber@MXene coaxial fibers with outstanding electromagnetic interference shielding efficiency. *Nano-Micro Lett.* **2022**, *14*, 111.
[152] Cheng, J. Y.; Li, C. B.; Xiong, Y. F.; Zhang, H. B.; Raza, H.; Ullah, S.; Wu, J. Y.; Zheng, G. P.; Cao, Q.; Zhang, D. Q. et al. Recent advances in design strategies and multifunctionality of flexible electromagnetic interference shielding materials. *Nano-Micro Lett.* **2022**, *14*, 80.
[153] Kumar, R.; Sahoo, S.; Joanni, E. Composites based on layered

materials for absorption of microwaves and electromagnetic shielding. *Carbon* **2023**, *211*, 118072.
[154] Liu, H. G.; Wu, S. Q.; You, C. Y.; Tian, N.; Li, Y.; Chopra, N. Recent progress in morphological engineering of carbon materials for electromagnetic interference shielding. *Carbon* **2021**, *172*, 569–596.
[155] Yu, Y. Y.; Liu, X. B.; Lu, D. Q.; Liu, T.; Li, Y. S.; Wu, Z. P. Recent progress in graphene based materials for high-performance electromagnetic shielding. *Carbon* **2025**, *236*, 120093.
[156] Cao, C. F.; Yu, B.; Chen, Z. Y.; Qu, Y. X.; Li, Y. T.; Shi, Y. Q.; Ma, Z. W.; Sun, F. N.; Pan, Q. H.; Tang, L. C. et al. Fire intumescent, high-temperature resistant, mechanically flexible graphene oxide network for exceptional fire shielding and ultra-fast fire warning. *Nano-Micro Lett.* **2022**, *14*, 92.
[157] Gong, X. F.; Hu, T. J.; Zhang, Y.; Zeng, Y. N.; Zhang, Y.; Jiang, Z. H.; Tan, Y. L.; Zou, Y. H.; Wang, J.; Dai, J. Y. et al. Trunk-inspired SWCNT-based wrinkled films for highly-stretchable electromagnetic interference shielding and wearable thermotherapy. *Nano-Micro Lett.* **2024**, *16*, 243.
[158] Han, X. W.; Hao, C.; Peng, Y. K.; Yu, H.; Zhang, T.; Zhang, H. N.; Chen, K. W.; Chen, H. Y.; Wang, Z. X.; Yan, N. et al. Novel cellulosic fiber composites with integrated multi-band electromagnetic interference shielding and energy storage functionalities. *Nano-Micro Lett.* **2025**, *17*, 122.
[159] Jia, Z. X.; Zhang, M. F.; Liu, B.; Wang, F. C.; Wei, G.; Su, Z. Q. Graphene foams for electromagnetic interference shielding: A review. *ACS Appl. Nano Mater.* **2020**, *3*, 6140–6155.
[160] Lee, J. H.; Kim, Y. S.; Ru, H. J.; Lee, S. Y.; Park, S. J. Highly flexible fabrics/epoxy composites with hybrid carbon nanofillers for absorption-dominated electromagnetic interference shielding. *Nano-Micro Lett.* **2022**, *14*, 188.
[161] Lee, J. S.; Kim, J. W.; Lee, J. H.; Son, Y. K.; Kim, Y. B.; Woo, K.; Lee, C.; Kim, I. D.; Seok, J. Y.; Yu, J. W. et al. Flash-induced high-throughput porous graphene via synergistic photo-effects for electromagnetic interference shielding. *Nano-Micro Lett.* **2023**, *15*, 191.
[162] Ma, H. Y.; Fashandi, M.; Rejeb, Z. B.; Ming, X.; Liu, Y. J.; Gong, P. J.; Li, G. X.; Park, C. B. Efficient electromagnetic wave absorption and thermal infrared stealth in PVTMS@MWCNT nano-aerogel via abundant nano-sized cavities and attenuation interfaces. *Nano-Micro Lett.* **2024**, *16*, 20.
[163] Shi, S. H.; Jiang, Y. H.; Ren, H.; Deng, S. W.; Sun, J. P.; Cheng, F. C.; Jing, J. J.; Chen, Y. H. 3D-printed carbon-based conformal electromagnetic interference shielding module for integrated electronics. *Nano-Micro Lett.* **2024**, *16*, 85.
[164] Guo, A. P.; Zhang, X. J.; Wang, S. W.; Zhu, J. Q.; Yang, L.; Wang, G. S. Excellent microwave absorption and electromagnetic interference shielding based on reduced graphene oxide@MoS_2/poly(vinylidene fluoride) composites. *ChemPlusChem* **2016**, *81*, 1305–1311.
[165] Prasad, J.; Singh, A. K.; Yadav, A. N.; Kumar, A.; Tomar, M.; Srivastava, A.; Kumar, P.; Gupta, V.; Singh, K. Molybdenum disulfide-wrapped carbon nanotube-reduced graphene oxide (CNT/MoS_2-rGO) nanohybrids for excellent and fast removal of electromagnetic interference pollution. *ACS Appl. Mater. Interfaces* **2020**, *12*, 40828–40837.
[166] Sajid, H. M.; Afzal, H.; Irfan, M.; Saleem, M.; Jan, R.; Javed, S.; Akram, M. A. Design of multilayered 2D nanomaterial composite structures for EMI shielding analysis. *ACS Omega* **2022**, *7*, 35586–35594.
[167] Dhanasekaran, A.; Dhanaraj, K.; Venugopal, V. Polyaniline/MoS_2/MWCNT ternary nanocomposite for effective electromagnetic interference shielding. *ACS Appl. Nano Mater.* **2024**, *7*, 25983–25994.
[168] Zhao, Z. H.; Qing, Y. C.; Kong, L.; Xu, H. L.; Fan, X. M.; Yun, J. J.; Zhang, L. M.; Wu, H. J. Advancements in microwave absorption motivated by interdisciplinary research. *Adv. Mater.* **2024**, *36*, 2304182.
[169] Gao, Z. G.; Ma, Z. H.; Lan, D.; Zhao, Z. H.; Zhang, L. M.; Wu, H. J.; Hou, Y. L. Synergistic polarization loss of MoS_2-based multiphase solid solution for electromagnetic wave absorption. *Adv. Funct. Mater.* **2022**, *32*, 2112294.
[170] Wen, J. M.; Deng, L. C.; Shen, H.; Chen, Q.; Wu, H. J. Plasma-assisted bipolarity carrier modulation in TMDs to accelerate dipole polarization for enhanced electromagnetic attenuation. *Adv. Funct. Mater.* **2026**, *36*>/, e19086.
[171] Chen, G.; Li, Z. J.; Zhang, L. M.; Chang, Q.; Chen, X. J.; Fan, X. M.; Chen, Q.; Wu, H. J. Mechanisms, design, and fabrication strategies for emerging electromagnetic wave-absorbing materials. *Cell Rep. Phys. Sci.* **2024**, *5*, 102097.
[172] Li, M. H.; Zhu, W. J.; Li, X.; Xu, H. L.; Fan, X. M.; Wu, H. J.; Ye, F.; Xue, J. M.; Li, X. Q.; Cheng, L. F. et al. $Ti_3C_2T_x$/MoS_2 self-rolling rod-based foam boosts interfacial polarization for electromagnetic wave absorption. *Adv. Sci.* **2022**, *9*, 2201118.
[173] Wang, H. H.; Zhang, D. Q.; Zhang, H. B.; Liu, T. T.; Xu, J. Y.; Cao, M. S. High absorption efficiency of WS_2/CNT_S hybrids with conductive network for high performance EMI shielding. *J. Phys.: Conf. Ser.* **2021**, *1948*, 012172.
[174] Mai, T.; Chen, L.; Wang, P. L.; Liu, Q.; Ma, M. G. Hollow metal-organic framework/MXene/nanocellulose composite films for giga/terahertz electromagnetic shielding and photothermal conversion. *Nano-Micro Lett.* **2024**, *16*, 169.
[175] Ruan, L. Y.; Meng, F. M.; Guo, H. T.; Jiang, H. J.; Qi, Y. Y.; Li, C. Y.; Zhang, R. N.; Pan, F.; Jia, W. W.; Yang, Y. et al. Simultaneously achieving ultra-stretchability and biocompatibility in electromagnetic interference shielding materials through a biomimetic strategy and MXene enhancement. *Adv. Funct. Mater.* **2025**, *35*, 2501821.
[176] Chen, Z. B.; Yang, S. D.; Huang, J. H.; Gu, Y. F.; Huang, W. B.; Liu, S. Y.; Lin, Z. Q.; Zeng, Z. P.; Hu, Y. G.; Chen, Z. M. et al. Flexible, transparent and conductive metal mesh films with ultra-high FoM for stretchable heating and electromagnetic interference shielding. *Nano-Micro Lett.* **2024**, *16*, 92.
[177] Liang, Q. Q.; He, M. K.; Zhan, B. B.; Guo, H.; Qi, X. S.; Qu, Y. P.; Zhang, Y. L.; Zhong, W.; Gu, J. W. Yolk-shell CoNi@N-doped carbon-CoNi@CNTs for enhanced microwave absorption, photothermal, anti-corrosion, and antimicrobial properties. *Nano-Micro Lett.* **2025**, *17*, 167.
[178] Pan, F.; Cai, L.; Shi, Y. Y.; Dong, Y. Y.; Zhu, X. J.; Cheng, J.; Jiang, H. J.; Wang, X.; Jiang, Y. F.; Lu, W. Heterointerface engineering of β-chitin/carbon nano-onions/Ni–p composites with boosted Maxwell-Wagner-Sillars effect for highly efficient electromagnetic wave response and thermal management. *Nano-Micro Lett.* **2022**, *14*, 85.
[179] Song, P.; Liu, B.; Liang, C. B.; Ruan, K. P.; Qiu, H.; Ma, Z. L.; Guo, Y. Q.; Gu, J. W. Lightweight, flexible cellulose-derived carbon aerogel@reduced graphene oxide/PDMS composites with outstanding EMI shielding performances and excellent thermal conductivities. *Nano-Micro Lett.* **2021**, *13*, 91.
[180] Zeng, Z. H.; Wang, G.; Wolan, B. F.; Wu, N.; Wang, C. X.; Zhao, S. Y.; Yue, S. Y.; Li, B.; He, W. D.; Liu, J. R. et al. Printable aligned single-walled carbon nanotube film with outstanding thermal conductivity and electromagnetic interference shielding performance. *Nano-Micro Lett.* **2022**, *14*, 179.
[181] >Zhou, M.; Tan, S. J.; Wang, J. W.; Wu, Y.; Liang, L. L.; Ji, G. B. "Three-in-One" multi-scale structural design of carbon fiber-based composites for personal electromagnetic protection and thermal management. *Nano-Micro Lett*. **2023**, *15*, 176.
[182] Shao, R. Z.; Wang, G. L.; Chai, J. L.; Lin, J.; Zhao, G. Q.; Zeng, Z. H.; Wang, G. Z. Multifunctional Janus-structured polytetrafluoroethylene-carbon nanotube-Fe_3O_4/MXene membranes

for enhanced EMI shielding and thermal management. *Nano-Micro Lett.* **2025**, *17*, 136.

[183] Shi, Y. Y.; Liao, S. Y.; Wang, Q. F.; Xu, X. Y.; Wang, X. Y.; Gu, X. Y.; Hu, Y. G.; Zhu, P. L.; Sun, R.; Wan, Y. J. Enhancing the interaction of carbon nanotubes by metal-organic decomposition with improved mechanical strength and ultra-broadband EMI shielding performance. *Nano-Micro Lett.* **2024**, *16*, 134.

[184] Song, P.; Ma, Z. L.; Qiu, H.; Ru, Y. F.; Gu, J. W. High-efficiency electromagnetic interference shielding of rGO@FeNi/epoxy composites with regular honeycomb structures. *Nano-Micro Lett.* **2022**, *14*, 51.

[185] Wang, X.; Dong, G. L.; Pan, F.; Lin, C.; Yuan, B.; Yang, Y.; Lu, W. Metal-support interaction induced electron localization in rationally designed metal sites anchored MXene enables boosted electromagnetic wave attenuation. *Nano-Micro Lett.* **2025**, *17*, 309.

[186] Wei, Y. W.; Bhuyan, P.; Kwon, S. J.; Kim, S.; Bae, Y.; Singh, M.; Tran, D. T.; Ha, M.; Jeong, K. U.; Ma, X. et al. Liquid metal grid patterned thin film devices toward absorption-dominant and strain-tunable electromagnetic interference shielding. *Nano-Micro Lett.* **2024**, *16*, 248.

[187] Prasad, J.; Singh, A. K.; Haldar, K. K.; Gupta, V.; Singh, K. Electromagnetic interference shielding effectiveness in 3D flower-like MoS_2-rGO/gadolinium-doped nanocomposites. *J. Alloys Compd.* **2019**, *788*, 861–872.

[188] Prasad, J.; Singh, A. K.; Tomar, M.; Gupta, V.; Singh, K. Strong electromagnetic wave absorption and microwave shielding in the Ni–Cu@MoS_2/rGO composite. *J. Mater. Sci.: Mater. Electron.* **2019**, *30*, 18666–18677.

[189] Prasad, J.; Singh, A. K.; Tomar, M.; Gupta, V.; Singh, K. High-efficiency microwave absorption and electromagnetic interference shielding of Cobalt-doped MoS_2 nanosheet anchored on the surface reduced graphene oxide nanosheet. *J. Mater. Sci.: Mater. Electron.* **2020**, *31*, 19895–19909.

[190] Prasad, J.; Singh, A. K.; Tomar, M.; Gupta, V.; Singh, K. Hydrothermal synthesis of micro-flower like morphology aluminum-doped MoS_2/rGO nanohybrids for high efficient electromagnetic wave shielding materials. *Ceram. Int.* **2021**, *47*, 15648–15660.

[191] Prasad, J.; Choi, Y. W.; Nam, M. G.; Moon, M. W.; Yoo, P. J. Enhanced dielectric properties and electromagnetic interference shielding effectiveness of 3D hierarchical nanohybrid of Au–Ag@MoS_2-rGO. *J. Alloys Compd.* **2024**, *999*, 175016.

[192] Prasad, J.; Singh, A. K.; Gahlot, A. P. S.; Tomar, M.; Gupta, V.; Singh, K. Electromagnetic interference shielding properties of hierarchical core-shell palladium-doped MoS_2/CNT nanohybrid materials. *Ceram. Int.* **2021**, *47*, 27586–27597.

[193] Prasad, J.; Singh, A. K.; Shah, J.; Kotnala, R. K.; Singh, K. Synthesis of MoS_2-reduced graphene oxide/Fe_3O_4 nanocomposite for enhanced electromagnetic interference shielding effectiveness. *Mater. Res. Express* **2018**, *5*, 055028.

[194] Prasad, J.; Singh, A. K.; Haldar, K. K.; Tomar, M.; Gupta, V.; Singh, K. $CoFe_2O_4$ nanoparticles decorated MoS_2-reduced graphene oxide nanocomposite for improved microwave absorption and shielding performance. *RSC Adv.* **2019**, *9*, 21881–21892.

[195] Sharma, R.; Seetala, N.; Clower, W.; Amritphale, S.; Alam, S.; Gordon, S.; Matthews, J.; Radadia, A. D. Synergistic effect of Mill scale and MoS_2 in geopolymer composites for EMI shielding application. *J. Mater. Sci.: Mater. Electron.* **2022**, *33*, 20056–20067.

[196] Liu, Z.; Liu, C. H.; Wang, Y.; Mi, R. Z.; Gao, X. P. Preparation and simulation performance of light carbon fiber paper-based electromagnetic shielding materials. *Carbon Lett.* **2024**, *34*, 1287–1299.

[197] Ren, Y. M.; Li, P. C.; Qin, Z.; Yan, Z. M.; Yang, S.; Zhang, Z. X.; Feng, D. S.; Xu, D. W.; Zheng, Y. J.; Yang, R. et al. Homodispersed MoS_2/Co_9S_8 heterostructure nanoparticles confined in rGO aerogels via Kirkendall effect for efficient electromagnetic interference shielding. *J. Alloys Compd.* **2024**, *989*, 174310.

[198] Li, X. L.; Sheng, M. J.; Gong, S.; Wu, H.; Chen, X. L.; Lu, X.; Qu, J. P. Flexible and multifunctional phase change composites featuring high-efficiency electromagnetic interference shielding and thermal management for use in electronic devices. *Chem. Eng. J.* **2022**, *430*, 132928.

[199] Guo, Y. Q.; Qiu, H.; Ruan, K. P.; Zhang, Y. L.; Gu, J. W. Hierarchically multifunctional polyimide composite films with strongly enhanced thermal conductivity. *Nano-Micro Lett.* **2022**, *14*, 26.

[200] Li, J.; Sun, H.; Yi, S. Q.; Zou, K. K.; Zhang, D.; Zhong, G. J.; Yan, D. X.; Li, Z. M. Flexible polydimethylsiloxane composite with multi-scale conductive network for ultra-strong electromagnetic interference protection. *Nano-Micro Lett.* **2023**, *15*, 15.

[201] Liang, C. B.; Gu, Z. J.; Zhang, Y. L.; Ma, Z. L.; Qiu, H.; Gu, J. W. Structural design strategies of polymer matrix composites for electromagnetic interference shielding: A review. *Nano-Micro Lett.* **2021**, *13*, 181.

[202] Sang, G. L.; Xu, P.; Yan, T.; Murugadoss, V.; Naik, N.; Ding, Y. S.; Guo, Z. H. Interface engineered microcellular magnetic conductive polyurethane nanocomposite foams for electromagnetic interference shielding. *Nano-Micro Lett.* **2021**, *13*, 153.

[203] Shi, T.; Gao, X.; Liu, H.; Wang, X. D. Multi-energy conversion and electromagnetic shielding enabled by carbonized polyimide/kevlar/graphene oxide@ZIF-67 bidirectional complex aerogel-encapsulated phase-change materials. *Nano-Micro Lett.* **2025**, *17*, 236.

[204] Tang, X. W.; Lu, Y. Z.; Li, S. S.; Zhu, M. Y.; Wang, Z. X.; Li, Y.; Hu, Z. Y.; Zheng, P. L.; Wang, Z. C.; Liu, T. X. Hierarchical polyimide nonwoven fabric with ultralow-reflectivity electromagnetic interference shielding and high-temperature resistant infrared stealth performance. *Nano-Micro Lett.* **2025**, *17*, 82.

[205] Liu, Y. L.; Zhu, T. Y.; Wang, Q.; Huang, Z. J.; Sun, D. X.; Yang, J. H.; Qi, X. D.; Wang, Y. Hierarchically porous polypyrrole foams contained ordered polypyrrole nanowire arrays for multifunctional electromagnetic interference shielding and dynamic infrared stealth. *Nano-Micro Lett.* **2025**, *17*, 97.

[206] Ma, L.; Hamidinejad, M.; Zhao, B.; Liang, C. Y.; Park, C. B. Layered foam/film polymer nanocomposites with highly efficient EMI shielding properties and ultralow reflection. *Nano-Micro Lett.* **2022**, *14*, 19.

[207] Oraby, H.; Naeem, I.; Darwish, M.; Senna, M. H.; Tantawy, H. R. Effective electromagnetic interference shielding using foamy polyurethane composites. *Polym. Compos.* **2021**, *42*, 3077–3088.

[208] Qian, K. P.; Zhou, J. Y.; Miao, M.; Wu, H. M.; Thaiboonrod, S.; Fang, J. H.; Feng, X. Highly ordered thermoplastic polyurethane/aramid nanofiber conductive foams modulated by kevlar polyanion for piezoresistive sensing and electromagnetic interference shielding. *Nano-Micro Lett.* **2023**, *15*, 88.

[209] Saboor, A.; Khalid, S. M.; Jan, R.; Khan, A. N.; Zia, T.; Farooq, M. U.; Afridi, S.; Sadiq, M.; Arif, M. PS/PANI/MoS_2 hybrid polymer composites with high dielectric behavior and electrical conductivity for EMI shielding effectiveness. *Materials* **2019**, *12*, 2690.

[210] Menon, A. V.; Madras, G.; Bose, S. Mussel-inspired self-healing polyurethane with "flower-like" magnetic MoS_2 as efficient microwave absorbers. *ACS Appl. Polym. Mater.* **2019**, *1*, 2417–2429.

[211] Sharma, S.; Singh, B. P.; Hur, S. H.; Choi, W. M.; Chung, J. S. Facile fabrication of stacked rGO/MoS_2 reinforced polyurethane composite foam for effective electromagnetic interference shielding. *Compos. Part A: Appl. Sci. Manuf.* **2023**, *166*, 107366.

[212] Dhanasekaran, A.; Malakar, A.; Lakshmanan, A.; Stranak, V.; Bose, S.; Dhanaraj, K.; Venugopal, V. Electromagnetic interference shielding properties of conductive polyaniline/TiO_2/MoS_2 hybrid composites. *ACS Omega* **2025**, *10*, 28143–28152.

[213] Zhou, J. Q.; Song, Z. M.; Wan, J. C.; Zhou, M. Z.; Zhu, B.; Qiao, K.; Cai, X. Polyaniline-functionalized MoS_2 nanosheets/carbon fiber network for structural and functional integration of composites.

Compos. Part B: Eng. **2025**, *306*, 112847.
[214] Zeng, Z. H.; Wu, N.; Wei, J. J.; Yang, Y. F.; Wu, T. T.; Li, B.; Hauser, S. B.; Yang, W. D.; Liu, J. R.; Zhao, S. Y. Porous and ultra-flexible crosslinked MXene/polyimide composites for multifunctional electromagnetic interference shielding. *Nano-Micro Lett.* **2022**, *14*, 59.
[215] Zhang, Y. L.; Gu, J. W. A perspective for developing polymer-based electromagnetic interference shielding composites. *Nano-Micro Lett.* **2022**, *14*, 89.
[216] Khosravi, A.; Zarepour, A.; Zarrabi, A.; Iravani, S. MXene-based wearable contact lenses: Integrating smart technology into vision care. *Nano-Micro Lett.* **2026**, *18*, 20.
[217] Ma, G. L.; Luo, Z. B.; Shao, H.; Shen, Y. B.; Lin, Z. F.; Simon, P. Tellurium-terminated MXene synthesis via one-step tellurium etching. *Nano-Micro Lett.* **2026**, *18*, 28.
[218] Yang, S. D.; Lin, Z. Q.; Wang, X. M.; Huang, J. H.; Yang, R. L.; Chen, Z. B.; Jia, Y.; Zeng, Z. P.; Cao, Z. L.; Zhu, H. J. et al. Stretchable, transparent, and ultra-broadband terahertz shielding thin films based on wrinkled MXene architectures. *Nano-Micro Lett.* **2024**, *16*, 165.
[219] Zarepour, A.; Ahmadi, S.; Rabiee, N.; Zarrabi, A.; Iravani, S. Self-healing MXene- and graphene-based composites: Properties and applications. *Nano-Micro Lett.* **2023**, *15*, 100.
[220] Yang, S. D.; Huang, W. Q.; Lin, Z. Q.; Chen, Z. B.; Yang, R. L.; Jia, Y.; Liu, X. B.; Wang, R.; Zeng, Z. P.; Hu, Y. G. et al. Janus MXene film with gradient structure for highly efficient terahertz and infrared electromagnetic absorption. *Nano Res* **2025**, *18*, 94907041.
[221] Wang, H.; Ding, J. H.; Zhao, H. R.; Chu, Q. C.; Zhu, J.; Wang, J. G. Robust and reprocessable biorenewable polyester nanocomposites *in situ* catalyzed and reinforced by dendritic MXene@CNT heterostructure. *Nano-Micro Lett.* **2025**, *17*, 161.
[222] Wu, X. Y.; Tu, T. X.; Dai, Y.; Tang, P. P.; Zhang, Y.; Deng, Z. M.; Li, L. L.; Zhang, H. B.; Yu, Z. Z. Direct ink writing of highly conductive MXene frames for tunable electromagnetic interference shielding and electromagnetic wave-induced thermochromism. *Nano-Micro Lett.* **2021**, *13*, 148.
[223] Xiong, J. H.; Zhao, X.; Liu, Z. L.; Chen, H.; Yan, Q.; Lian, H. X.; Chen, Y. X.; Peng, Q. Y.; He, X. D. Multifunctional nacre-like nanocomposite papers for electromagnetic interference shielding via heterocyclic aramid/MXene template-assisted *in-situ* polypyrrole assembly. *Nano-Micro Lett.* **2025**, *17*, 53.
[224] Xue, T. T.; Yang, Y.; Yu, D. Y.; Wali, Q.; Wang, Z. Y.; Cao, X. S.; Fan, W.; Liu, T. X. 3D printed integrated gradient-conductive MXene/CNT/polyimide aerogel frames for electromagnetic interference shielding with ultra-low reflection. *Nano-Micro Lett.* **2023**, *15*, 45.
[225] Yang, R. L.; Gui, X. C.; Yao, L.; Hu, Q. M.; Yang, L. L.; Zhang, H.; Yao, Y. T.; Mei, H.; Tang, Z. K. Ultrathin, lightweight, and flexible CNT buckypaper enhanced using MXenes for electromagnetic interference shielding. *Nano-Micro Lett.* **2021**, *13*, 66.
[226] Yin, G.; Wu, J.; Qi, C. Z.; Zhou, X. F.; Yu, Z. Z.; Zhang, H. B. Pickering emulsion-driven MXene/silk fibroin hydrogels with programmable functional networks for EMI shielding and solar evaporation. *Nano-Micro Lett.* **2025**, *17*, 312.
[227] Yu, Y. H.; Yi, P.; Xu, W. B.; Sun, X.; Deng, G.; Liu, X. F.; Shui, J. L.; Yu, R. H. Environmentally tough and stretchable MXene organohydrogel with exceptionally enhanced electromagnetic interference shielding performances. *Nano-Micro Lett.* **2022**, *14*, 77.
[228] Anand, S.; Mani, D.; Islam, M. A.; Choi, W. K.; Park, P. J.; Kim, H.; Kim, S. R. Self-alignment of MXene films induced by electrostatic repulsion from TaS_2 nanosheets for multifunctional applications. *ACS Appl. Mater. Interfaces* **2025**, *17*, 57486–57499.
[229] Xing, Y. Q.; Wan, Y. Z.; Wu, Z.; Wang, J. Q.; Jiao, S. L.; Liu, L. Multilayer ultrathin MXene@AgNW@MoS_2 composite film for high-efficiency electromagnetic shielding. *ACS Appl. Mater. Interfaces* **2023**, *15*, 5787–5797.
[230] Ahmed, S.; Li, B. S.; Luo, S. H.; Liao, K. Heterogeneous $Ti_3C_2T_x$ MXene-MWCNT@MoS_2 film for enhanced long-term electromagnetic interference shielding in the moisture environment. *ACS Appl. Mater. Interfaces* **2023**, *15*, 49458–49467.
[231] Liu, K. Y.; Zhang, H. W.; Qin, Y. T.; Lan, C. T.; Jia, H. Gradient structured MoS_2@MXene/MXene/aramid nanofiber composite film with excellent electromagnetic interference shielding performance. *Diam. Relat. Mater.* **2024**, *148*, 111449.
[232] Li, Y. H.; Wang, Y.; Li, Z.; Ma, S. P.; Zhang, Y. W.; Fan, F.; Huang, Y. Meter-scale wearable multifunctional core-shell nanofiber textiles for ultra-broadband electromagnetic interference shielding and infrared stealth. *Adv. Mater.* **2025**, *37*, 2501485.
[233] Zhou, Y.; Zhang, W.; Pan, D.; Li, Z. Y.; Zhou, B.; Huang, M.; Mi, L. W.; Liu, C. T.; Feng, Y. Z.; Shen, C. Y. Absorption-reflection-transmission power coefficient guiding gradient distribution of magnetic MXene in layered composites for electromagnetic wave absorption. *Nano-Micro Lett.* **2025**, *17*, 147.
[234] Zhu, C. B.; Hao, Y. R.; Wu, H.; Chen, M. N.; Quan, B. Q.; Liu, S.; Hu, X. P.; Liu, S. L.; Ji, Q. H.; Lu, X. et al. Self-assembly of binderless MXene aerogel for multiple-scenario and responsive phase change composites with ultrahigh thermal energy storage density and exceptional electromagnetic interference shielding. *Nano-Micro Lett.* **2024**, *16*, 57.
[235] Hu, Y.; Sha, Y.; Chen, L.; Ma, Y. F.; Huang, Q.; Zhang, M.; Jia, P. Y.; Zhou, Y. H. Bio-based adaptable dynamically cross-linked networks and their composites: Multiple stimulus responses and potential electromagnetic shielding applications. *J. Mater. Chem. A* **2025**, *13*, 4317–4328.
[236] Cheng, S. Y.; Chen, Z. L.; Sheng, D. H.; Dong, W.; Cao, R.; Su, Z. B.; Wu, M. D.; Zhu, X. F.; Xie, A. M.; Mukherjee, S. et al. Sustainable electromagnetic interference shielding materials from cellulose-grafted *n*-type polymers. *Nat. Commun.,* **2025**, *16*, 8608.
[237] Guo, Z. Z.; Zhao, Y. D.; Luo, P. E.; Wang, J. J.; Pei, L.; Yu, H.; Song, P.; Ren, F.; Ren, P. G. Asymmetric and mechanically enhanced MOF derived magnetic carbon-MXene/cellulose nanofiber films for electromagnetic interference shielding and electrothermal/photothermal conversion. *Chem. Eng. J.* **2024**, *497*, 155707.
[238] Lang, L.; Ren, W. N.; Men, J. Y.; Mao, X. Y.; Yang, Z. L.; Zhang, S. R.; Wang, L. Advances in electromagnetic interference shielding materials with low reflection. *Eng. Sci.* **2025**, *36*, 1640.
[239] Rani, P.; Murthy, V. R. K.; Pasha, S. K. K. Development of MXene based organic polymer nanocomposites as highly efficient electromagnetic interference shielding materials: A review. *Coordin. Chem. Rev.* **2026**, *548*, 217104.
[240] Jiao, S.; Wang, Y. D.; Che, W. R.; Pan, F.; Sui, Z. Y.; Pang, X. Y.; Zhang, Q. D.; Cai, W. Q.; Wu, N.; Zeng, Z. H. Perspective of aramid-nanofiber-based electromagnetic interference shielding materials. *J. Mater. Sci. Technol.* **2025**, *253*, 179–193.
[241] Hassan, M. W.; Elshazly, T. M.; Ponnamma, D. Cellulose-inspired approaches to sustainable EMI shielding materials: A comprehensive review. *Int. J. Biol. Macromol.* **2024**, *273*, 132920.
[242] Xiong, C. Y.; Xiong, Q.; Zhao, M. J.; Wang, B.; Dai, L.; Ni, Y. H. Recent advances in non-biomass and biomass-based electromagnetic shielding materials. *Adv. Compos. Hybrid Mater.* **2023**, *6*, 205.
[243] Zeng, Z. H.; Zhang, Y. F.; Ma, X. Y. D.; Shahabadi, S. I. S.; Che, B. Y.; Wang, P. Y.; Lu, X. H. Biomass-based honeycomb-like architectures for preparation of robust carbon foams with high electromagnetic interference shielding performance. *Carbon* **2018**, *140*, 227–236.
[244] Govindasamy, T.; Mathew, N. K.; Asapu, V. K.; Subramanian, V.; Subramanian, B. Synergistic advancements in electromagnetic interference shielding: Harnessing Fe_3O_4 nanoparticles and biomass-

derived n-doped carbon-layered structure for next-generation nanocomposites. *ACS Sustain. Res. Manage.* **2024**, *1*, 289–302.
[245] Bharath, V.; Reddy, S. B. Sustainable electromagnetic interference shielding with biomass waste. In *Electromagnetic Field - from Atomic Level to Engineering Applications*. Wang, C.; Kang, Y. F., Eds; IntechOpen, 2025.
[246] Zhang, Q.; Wang, K.; Chen, X. C.; Tang, X. H.; Zhao, Q.; Fu, Q. Biomass composite based on metallized bamboo fiber for electromagnetic interference shielding, joule heating, and solar heating. *Compos. Sci. Technol.* **2023**, *243*, 110228.
[247] Zhai, M. Z.; Zhao, S. J.; Guo, H.; Li, X. C.; Shi, X. T.; He, M. K.; Zhang, Y. L.; Gu, J. W. Bionic-structured electromagnetic interference shielding composites. *Sci. Bull.* **2025**, *70*, 2347–2364.
[248] Wu, H. R.; Liu, C. C.; Chu, S. Y.; Feng, X. F.; Liu, X. B. Integrated super-engineering polymeric electromagnetic interference shielding films withstanding the extreme environments. *Chem. Eng. J.* **2023**, *472*, 144853.
[249] Ouda, M.; Sanad, A. A. A.; Krishna, A.; Kandah, M. I.; Kurdi, J. Advancing environmental sustainability: A comprehensive review of waste-based composite materials for efficient electromagnetic shielding and absorption. *IEEE Access* **2025**, *13*, 15028–15061.